Coupled Nonlinear Dynamics of Bubble and Bubble Cluster Oscillations

March 2017

A thesis submitted in partial fulfilment of the requirements for the degree of
Doctor of Philosophy in Engineering

Keio University

Graduate School of Science and Technology
School of Integrated Design Engineering

SUGITA, Naohiro

Acknowledgements

Firstly, I would like to express my sincere gratitude to my advisor Professor Toshihiko Sugiura for the continuous support of my Ph.D. study and related research throughout these past six years. His guidance helped me in all the time of research and writing of this thesis. Besides my advisor, I would like to thank the rest of my thesis committee: Professors Tatsuo Sawada, Tatsuo Iguchi, Kenjiro Takemura and Keita Ando for their insightful comments and encouragement.

Especially, I would like to express my sincere gratitude to Keita Ando, for his lecture of fluid dynamics and discussion on bubble dynamics. I would also like to express my thanks to members in Ando's laboratory: Tatsuya Yamashita, Takehiro Nakajima for their support on image processing employed in my experiment, Sosuke Hukui for his advice on preparation of experimental equipments, and Izumi Watanabe and Daijiro Murakami for designing my experimental apparatus using High-speed camera supported by Terasaka laboratory.

I had great time with my laboratory member. I always enjoyed discussion with Masahiko Sasaki and Kosuke Kanda on dynamical analysis. Their comments and insightful advice also helped me understanding complex phenomena of structural dynamics, which allow me to greatly improve this thesis. I am also very thankful to the members of bubble group, especially to Koney Dupol Kanwar, Takeshi Nagasawa, Takeshi Okada and Hikari Hebiguchi. I would also like to express my thanks to Dr. Katsuhiko Kimura for his thoughtful advices on preparation of this thesis.

Finally, I would express a deep sense of gratitude to my parents and grandmother for their effort and consideration to my life in Keio University.

Abstract

The dynamics of an oscillating bubble in an acoustic field has been employed in a wide range of engineering and medical applications. The key mechanism is an activity of bubble oscillations interacting with an external driving sound pressure. The behavior of oscillating bubbles is interpreted as a coupled dynamical system of nonlinear oscillatiors, indicating that individual bubbles are mutually coupled with neighboring bubbles and surrounding wall boundaries via an acoustic radiation. Therefore, there is a need to understand the coupled bubble dynamics for effective and advanced operation of oscillating bubbles in practical applications. The main aim of this thesis is to investigate the coupled bubble-bubble and bubble-wall dynamics in an acoustic field. The present thesis contains nonlinear modal analysis of bifurcation structures of coupled two-bubble oscillation, experiment and modeling of translational dynamics of oscillating bubble cluster and coupled fluid-structure simulation of bubble oscillations near an elastic boundary.

Nonlinear modal analysis of coupled oscillation of two spherical bubbles is presented on the basis of the method of multiple scales. Analytical expressions of nonlinear normal modes (NNMs) and steady-state oscillations are derived and underlying bifurcation structures are discussed. For the case of equally-sized bubbles, symmetry-breaking bifurcations arise in the neighborhood of NNMs, leading to energy localization in the steady-state oscillations.

Translational motion of an oscillating bubble cluster is experimentally observed by a high-speed imaging technique. The trajectory of the cluster motion is computationally calculated from the recorded images, and the classical theory of the translational dynamics of a single bubble is extended to the bubble cluster and compared with the experimental result. For a millimeter sized bubble cluster observed in the present experiment, the translational dynamics of the bubble cluster is described by the force balance between the classical expression of the secondary Bjerknes force and the cluster inertia from the mass of liquid in the cluster and the added mass of the cluster.

Coupled dynamics between an oscillating bubble and an elastic wall with a finite thickness is numerically explored, and effect of the wall thickness are discussed. Assuming that the ambient fluid undergoes a potential flow in an axisymmetric two dimensional domain, a set of boundary integral equations for use of boundary element formulation is derived. Eigenvalue analysis of the linear elastodynamics of a circular elastic plate is performed to obtain eigenfunctions and eigenfrequencies of normal modes. The equation of motion of the normal modes (i.e., the equation of motion of the wall surface) is derived. A numerical method to solve the previously presented coupled fluid-structure model is summarized in the following section. The boundary element method with boundary tracking of the bubble wall is employed to solve the moving boundary problem of the bubble dynamics. The elastodynamics of the elastic wall is formulated by the finite element method with Newmark's time stepping. The results are compared with the case of a rigid boundary. The results shows the translation velocity of the oscillating bubble substantially decreases as the wall surface oscillates in phase with the bubble oscillations. This indicates that the surface wave needs to be incorporated in the model of an elastic boundary for accurately describing the translational bubble dynamics.

Contents

Acknowledgements **iii**

Abstract **iii**

1 Introduction **1**

1.1 Motivation 1

1.2 Studies of bubble oscillations 2

1.2.1 Coupled bubble-bubble dynamics 2

1.2.2 Bubble cluster oscillation and translation 6

1.2.3 Interaction with boundaries 8

1.3 Contribution and outline 10

2 Nonlinear modal analysis of coupled two-bubble oscillation **13**

2.1 Model equation 14

2.1.1 Rayleigh–Plesset equation 14

2.1.2 Equations of radial motion 15

2.1.3 Dimensionless form 16

2.1.4 Linear normal modes 18

2.2 Perturbation analysis 20

2.2.1 Small-amplitude approximation 20

2.2.2 Perturbation solution 21

2.2.3 Nonlinear normal modes 25

2.2.4 Steady state solution 28

2.3 Numerical results 33

2.4 Summary 36

3 Translational dynamics of an oscillating bubble cluster 39

3.1 Experimental method 39

3.1.1 Experimental setup 39

3.1.2 Preparation of a bubble cluster 40

3.1.3 Image processing 42

3.2 Experimental observation 43

3.2.1 Overview of bubble cluster dynamics 43

3.2.2 Bubble collapse, fission and cluster oscillation 44

3.2.3 Interaction with wall boundaries 47

3.3 Modeling of the translational motion 49

3.3.1 Secondary Bjerknes force 49

3.3.2 Translational motion of the bubble cluster 52

3.4 Comparison to the experimental result 54

3.5 Summary 55

4 Coupled bubble dynamics with an elastic boundary 57

4.1 Boundary integral modeling of bubble dynamics 57

4.1.1 Basic equation 57

4.1.2 Boundary integral formulation 59

4.1.3 Boundary condition 61

4.2 Linear elastodynamics of a circular plate 61

4.2.1 Basic equation 61

4.2.2 Dynamic Love's stress function 62

4.2.3 Dimensionless form 63

4.2.4 Boundary condition 64

4.2.5 Eigenvalue analysis 64

4.2.6 Orthogonality of the eigenfunction 67

4.2.7 Wave equation of the wall surface 70

4.3 Numerical method 72

4.3.1 Spatial discretization 73
4.3.2 Smoothing scheme 75
4.3.3 Galerkin approximation 76
4.3.4 Adaptive time step 77
4.3.5 Newmark method 77
4.4 Numerical results 78
4.4.1 Sample calculation 78
4.4.2 Summary 82

5 Concluding remarks **83**
5.1 Summary and conclusions 83
5.2 Suggestions for future work 85

A Nonlinear modal analysis **87**
A.1 The scale analysis of the translational velocity 87
A.2 List of the dimensionless parameters 88
A.3 Hopf bifurcation 89

B Dynamical analysis of the translational motion of an oscillating bubble **91**
B.1 Eigenvalue analysis 91

Bibliography **93**

List of Figures

1.1 A schematic of bubble-wall interaction. 10

2.1 Schematic of two oscillating bubbles. 15

2.2 The NNMs Ni ($i = 1, 2, 3, 4$) as a function of normal oscillation frequency ω (Case A: $R_{10} = R_{20} = 10\ \mu\mathrm{m}$). The LNMs, L1 and L2, are also shown for comparison. 27

2.3 The steady-state amplitude (top) and the phase shift (bottom) of the fundamental component for case B as a function of the dimensionless driving frequency denoted by ai (i =1,2,3 and 4) in different colors. Solid and dashed lines stand for stable and unstable solutions, respectively. For convenience, the NNMs in Fig. 2.2 are also depicted. The numerical results (circles) are the steady-state fundamental component extracted from the FFT spectrum of time-radius curve. 29

2.4 The steady-state solution of the branches a1 to a4 plotted in a Δx-Δy configuration space for (a) the branch a1 at $\omega_f = 0.92$, (b) the branch a2 at $\omega_f = 1.02$, (c) the branch a3 at $\omega_f = 0.97$ and (d) the branch a4 at $\omega_f = 0.97$. The physical parameters are the same as those of Fig. 2.3. Analytical solutions are the first approximation given by Eqs. (2.49) to (2.54). Numerical curves were obtain by time-integration of Eqs. (2.5) and (2.6). 29

2.5 The steady-state amplitude (top) and the phase shift (bottom) of the fundamental component for case C as a function of the dimensionless separation distance denoted by bi (i =1,2,3 and 4) in different colors. Solid and dashed lines stand for stable and unstable solutions, respectively. The numerical results (circles) are the steady-state fundamental component extracted from the FFT spectrum of time-radius curve. 30

2.6 The steady-state amplitude (top) and the phase shift (bottom) of the fundamental component denoted by ci (i =1,2,3,4,5 and 6) in different colors. The parameters are same as case B in Table 1. For comparison to Fig. 2.3, the effect of finite speed of sound is incorporated only in the retardation effect, while neglecting the radiation damping. The numerical results are obtained form Eqs. (2.15) and (2.16). The parameter of the retardation time is $\tau^* = 0.86$. Note that the peak amplitudes of c3 and c4 are substantially damped compared to Fig. 2.3, and out-of-phase motions (c5 and c6) manifest in the neighborhood of N2. 31

2.7 Time-radius curves for (a) $\omega_f = 0.40$ (second superharmonic resonance), (b) $\omega_f = 0.70$ (primary resonance). The physical parameters are case D ($d^* = 7.5$, and $A = 1.00$) in Table 2.1. 33

2.8 Frequency response curves of the maximum bubble radii obtained from the steady-state oscillation after 32 cycles of the driving period. The physical parameters are case D ($d^* = 7.5$, and $A = 1.00$) in Table 2.1. The sound pressure corresponds to 100 kPa. 34

2.9 Contour plot of $\Delta R_{\text{max}} = (R_{2\text{max}} - R_{1\text{max}})/R_{10}$ as a function of the driving frequency and the separation distance. Note that $\Delta R_{\text{max}} = 0$ indicates non-localized oscillation which is not plotted, and only localized oscillation $\Delta R_{\text{max}} \neq 0$ is plotted. The physical parameters used are those for case E ($d^* = 3 - 45$, and $A^* = 1.00$) in Table 2.1. 35

3.1 Schematic of (a) experimental setup, (b) an enlarged view of the silicone plug and needle and (c) comparison of a typical photographed image (left) and the image processing with a bounding box and its centroid (right). 41

3.2 Sideview of an injected bubble nucleus corresponding to the schematic in Fig. 3.1(b). 42

3.3 Trajectory of a cluster motion denoted by a red solid line. Representative pictures of the cluster are superimposed: (a) initial state, (b) collapse and fission, (c) jet formation and (d) oscillation in contact with the side wall. The injected bubble nucleus departs from the silicone plug and moves toward the right side wall. 43

3.4 Snapshots of (a) the initial state, (b) maximum expansion, and (c-f) the consecutive collapse phases. The scale bar represents 2 mm. 44

3.5 A typical image sequence of an oscillating bubble cluster driven at 625 Hz. The image sequence corresponds to one oscillation cycle of the imposed driving frequency. The scale bar represents 2 mm. 44

3.6 The results of image processing. (a) R_b–t curve, (b) R_b–t curve (enlarged) and (c) its Fourier spectrum. The fitting curve in (b) was reproduced using the frequency component up to the third harmonics of (c). 45

3.7 The temporal evolution of the cluster position. 45

3.8 A typical image sequence of an oscillating bubble cluster driven at 312 Hz. The image sequence corresponds to one oscillation cycle of the imposed driving frequency. The scale bar represents 2 mm. 46

3.9 An image sequence of (a) the jet-like motion and (b) hemispherical oscillation in contact with the right side wall driven at 625 Hz. The scale bar represents 2 mm. 48

3.10 Schematic of the water vessel (top view). X and $2L$ denote the center of a hemispherical bubble cluster and the separation distance between the left and right side walls, respectively. The bubble cluster is mirrored with respect to the left and right side walls; the mirrored clusters are set at $2\,(L+X)$ and $2\,(L-X)$ away from the original cluster. 50

3.11 Comparison between the experiment and simulations: the results of the temporal evolution of the cluster position. The parameter for the acoustic energy loss is set at $\Re[Q] = 0.22$. 54

4.1 A schematic of bubble-wall interaction. 58

4.2 Eigenfrequency of the $(1, n)$ eigenmodes (n = 1, 2, 3, 4 and 5) as a function of the wall thickness for the case of (a) G = 1.5 kPa, and (b) G = 15 kPa. The eigenfrequency and the wall thickness are normalized, respectively, by the adiabatic natural frequency and the initial radius of an isolated bubble. 68

4.3 The parameters of the $(1, n)$th eigenmode (n = 1, 2, 3, 4 and 5) as a function of the wall thickness: (a) mass, (b) tension and (c) stiffness. . . 72

4.4 Temporal evolution of (a) the bubble mean radius, R_b, and (b) the bubble center, X_b, for case (a) in Table 4.1. For comparison, the displacement of the elastic wall at $r = 0$, w_c, is plotted in dashed line. 79

4.5 Temporal evolution of bubble and wall profiles. The corresponding time history of the bubble mean radius and bubble center are shown in Fig. 4.4. The displacement of the wall is illustrated with 100-fold magnification. 79

4.6 The temporal evolution of the bubble center, X_b, for different oscillation modes: (a) (m, n) = (1,1), (b) (m, n) = (1,2), (c) (m, n) = (1,3). The wall thickness is fixed to h = 1.0, and the other parameters are listed in Table 4.1. 80

4.7 The temporal evolution of the bubble center, X_b, for different wall thicknesses: (a) h = 1.0, (d) h = 0.8, and (e) h = 2.0. The oscillation mode is fixed at $(1, 1)$, and the other parameters are listed in Table 4.1. 81

A.1 The steady-state amplitude of the fundamental component for case F $(R_{10} = R_{20} = 100\ \mu\mathrm{m})$ in Table 2.1 as a function of the driving frequency denoted by di (i =1,2,3,4,5 and 6) in different colors. The numerical results of periodic solutions are shown by circles. The vertical lines indicate modulation amplitudes of quasi-periodic oscillations obtained during 1000 oscillation periods of the driving frequency. 89

List of Tables

2.1 Dimensionless parameters for air bubbles in water and the atmospheric ambient pressure. The equilibrium radii of the two bubbles are 10 μm for all the cases. Case A corresponds to an undamped free oscillation (damping and driving pressure are removed), and the other cases are for forced oscillation with damping effects. Note that in case D and E Reynolds number is calculated with the effective kinematic viscosity $\nu_{\text{eff}} = 6.73 \times 10^{-3}\ \text{m}^2/\text{s}$, and the effective polytropic exponent $\kappa_{\text{eff}} = 1.10$. The corresponding driving pressure are 2.5 and 100 kPa for $A^* = 2.50 \times 10^{-2}$ and 1.00, respectively. 33

3.1 The cluster radius R_c and oscillation amplitudes δ_k determined by the experimentally obtained Fourier spectrum. The radius of the (initially injected) bubble nucleus is $R_0 = 1.01$ mm. The imposed sound frequency is 625 Hz. 54

4.1 Dimensionless parameters with different wall thicknesses and the oscillation mode of (m, n) mode. The radius of the elastic layer is fixed at $a = 5R_0$, and the modulus of rigidity is G = 1.5 kPa. In cases (a) to (c), the wall thickness is fixed at 1.0, and different oscillation modes are considered. The wall thickness is varied in cases (d) and (e) for the fundamental mode $(1, 1)$. These cases are compared with the case of rigid boundary. 78

List of Abbreviations

BEM	**B**oundary **E**lement **M**ethod
FEM	**F**oundary **E**lement **M**ethod
NNM	**N**onlinear **N**ormal **M**ode
PV	Cauchy's **P**rincipal **V**alue

List of Symbols

A^*	Driving pressure normalized by static pressure	[-]
A_i	Complex amplitude	[-]
A	Displacement amplitude of the vibration generator	$[\mathrm{m}]$
A_{box}	Area of a bounding-box	$[\mathrm{m}^2]$
a_i	Steady-state amplitude of ith bubble	[-]
a_{bp}	Amplitude at a bifurcation point	[-]
a_0	Equilibrium radius of bubble fragments in the cluster	$[\mathrm{m}]$
a	Radius of the elastic body	$[\mathrm{m}]$
B	Intensity of the acoustic radiation from bubble cluster	[-]
c	Speed of sound in liquid	$[\mathrm{m/s}]$
C	Dimensionless speed of sound	[-]
C_D	rag coefficient	[-]
c_i	Damping coefficient due to the viscous and radiation effects	[-]
cc	Complex conjugate of the preceding terms	
c_s	Speed of transversal sound wave	[m/s]
c_p	Speed of longitudinal sound wave	[m/s]
d	Separation distance between the bubble centers	$[\mathrm{m}]$
d^*	Dimensionless separation distance	[-]
D_k	Time differentiation with respect to t_k	[-]
d_w	Distance between the bubble center and the elastic wall	$[\mathrm{m}]$
Eu	Euler number	[-]
e_i	Driving amplitude of the acoustic pressure	[-]
e_{ij}	Deformation rate tensor	$[\mathrm{s}^{-1}]$

F_{B}	Bjerknes force	[N]
F_{A}	Inertial force due to additional mass	[N]
F_{D}	Drag force	[N]
g	Gravitational acceleration	$[\mathrm{m/s^2}]$
G	Modulus of rigidity	$[\mathrm{N/m}]$
G^{AX}	Fundamental solution of Laplace's equation in an axisymmetric domain	$[\mathrm{m}^{-1}]$
H	Water depth measured from the free surface	[m]
h	Thickness of the elastic body	[m]
J_i	Bessel function of the first lind of the ith order	[-]
K_i	Coefficient of nonlinear term	[-]
k_p	Wave number of transversal sound wave	$[\mathrm{m}^{-1}]$
k_s	Wave number of longitudinal sound wave	$[\mathrm{m}^{-1}]$
l	Distance to measurement point from the cluster center	[m]
L	Inside size of the water vessel	[m]
m	Mass within the cluster	[kg]
m^*	Dimensionless mass	[-]
M_s	Mach number of the transversal wave	[-]
M_p	Mach number of the longitudinal wave	[-]
p_r	Radiation pressure	[Pa]
p_∞	Pressure in the far field	[Pa]
p_0	Hydrostatic pressure in the far field	[Pa]
p_a	Driving pressure	[Pa]
$p_{\mathrm{ex}}(t)$	External driving pressure	[Pa]
p_2	Liquid pressure at the bubble wall	[Pa]
${p_i}^*$	Dimensionless liquid pressure at bubble walls	[-]
Pe	Péclet number	[-]
p	Eigenfrequency of a circular elastic plate	[Pa]
p_{rad}	Secondary pressure field	[Pa]

p_b	Liquid pressure at bubble wall	[Pa]
P_{G0}	Initial gas pressure of the bubble contents	[Pa]
p_n	nth eigenfrequency	[-]
p_w	Pressure at the elastic wall	[Pa]
p_v	Vapor pressure	[Pa]
Q	Complex reflection coefficient	[-]
R_0	Equilibrium bubble radius	[m]
$R_i(t)$	Time-varying radii	[m]
R_{i0}	Equilibrium radius of ith bubble	[m]
R^*	Ratio of the initial radii	[-]
Re	Reynolds number	[-]
$R_{i\max}$	Maximum bubble radii	[m]
R_b	Area-equivalent mean radius(cluster radius)	[m]
r	Coordinate in the spherical coordinate	[m]
R	Time-varying cluster radius	[m]
R_c	Mean radius of the cluster	[m]
Re_U	Maximum particle Reynolds number, $2R_cU\nu_L^{-1}$	[-]
$\mathcal{R}$	Eigenfunction in the r direction	[-]
S	Surface tension	[N/m]
t	Time	[s]
t^*	Nondimensional time	[-]
t_b	Traction at surface of the elastic wall	[-]
t_k	Time in the ϵ^k order	[-]
u_i	Translational velocity of ith bubble	[m/s]
U	Transient velocity	[m/s]
U^*	Nondimensional translational velocity	[-]
U_0^*	Initial velocity	[m/s]
U_max	Maximum velocity	[m/s]

U_{st^*}	Velocity at a fixed point	$[\mathrm{m/s}]$
u	Fluid velocity	$[\mathrm{m/s}]$
u_r	Displacement in the r direction	$[\mathrm{m}]$
u_z	Displacement in the z direction	$[\mathrm{m}]$
u_r^*	Dimensionless displacement in the r direction	[-]
u_z^*	Dimensionless displacement in the z direction	[-]
$V_i(w)$	Time-varying volume of ith bubble	$[\mathrm{m}^3]$
$V(t)$	Volume of bubbler	$[\mathrm{m}^3]$
V_0	Equilibrium bubble volume	$[\mathrm{m}^3]$
We	Weber number	[-]
w	Displacement of an elastic wall surface	$[\mathrm{m}]$
w_t	Retarded time frame	[s]
x_i	Solution of Δx of the ϵ^i order	[-]
X	Position of an oscillating bubble cluster in the x direction	$[\mathrm{m}]$
X_{st}^*	Position at a fixed point	$[\mathrm{m}]$
y_i	Solution of Δy of the ϵ^i order	[-]
Y	Position of an oscillating bubble cluster in the y direction	$[\mathrm{m}]$
$\mathcal{Z}$	Eigenfunction in the z direction	[-]
α	Detuning parameter of the driving frequency	[-]
α_{th}	Thermal diffusivity of the gas	$[\mathrm{m}^2/\mathrm{s}]$
α_c	Void fraction	[-]
α_n	nth zero of the Bessel function of the first kind	[-]
β_{ii}	Parameter associated with quadratic nonlinear terms	[-]
β_{iii}	Parameter associated with cubic nonlinear terms	[-]
γ	Ratio of the specific heats of bubble contents	[-]
$\Delta R_{\max}$	Maximum amplitude	$[\mathrm{m}]$
δ_k	Oscillation amplitude	[-]
δx	Perturbation of x	[-]

δu	Perturbation of u	[-]
δ_{3D}	Dirac delta function in three dimensional space	[-]
ϵ	Finite dimensionless quantity	[-]
κ	Polytropic index	[-]
κ_{eff}	Effective polytropic index	[-]
Λ	Lamé’s first parameter	[-]
λ	Wave number of nth eigenfunction in the r direction	[-]
μ_L	Liquid viscosity	$[\mathrm{Pa\,s}]$
μ_i	Strength of the acceleration’s coupling term	[-]
ν_{eff}	Effective kinetic viscosity	$[\mathrm{Pa\,s}]$
ν_L	Kinetic Viscosity	$[\mathrm{m}^2/\mathrm{s}]$
ν	Poisson’s ratio	[-]
ρ_L	Liquid density	$[\mathrm{kg}/\mathrm{m}^3]$
ρ_w	Density of an elastic body	$[\mathrm{kg}/\mathrm{m}^3]$
σ	Detuning parameter of the driving frequency	[-]
τ^*	Dimensionless retarded time	[-]
τ	Stress tensor of isotropic liner elasticity	$[\mathrm{Pa}]$
Φ	Adjoint function	[-]
ϕ_i	Phase angle of ith bubble	$[\mathrm{rad}]$
ϕ_k	Phase angle of frequency components	$[\mathrm{rad}]$
ϕ	Velocity potential	$[\mathrm{m}^2/\mathrm{s}]$
χ	Love’s stress function	$[\mathrm{J}]$
ω	Angular frequency	$[\mathrm{rad}/\mathrm{s}]$
ω_N	Adiabatic natural frequency of an unbounded bubble	$[\mathrm{rad}/\mathrm{s}]$
ω_f	Angular driving frequency	$[\mathrm{rad}/\mathrm{s}]$
ω_i	Partial natural frequency of ith bubble	$[\mathrm{rad}/\mathrm{s}]$
ω_{Li}	Modal natural frequency of the LNMs	rad/s
Ω_i	Oscillation phase of free oscillation	[-]

ω_{bp}	Frequency at the bifurcation point	[-]
ω_c	Cluster's resonance frequency	$[\mathrm{rad/s}]$
ω_M	Minnaert frequency	$[\mathrm{rad/s}]$

Chapter 1

Introduction

1.1 Motivation

The role of bubble oscillation has extended to a wide range of engineering and medical applications such as ultrasonic cleaning, food processing, ultrasound imaging and therapy. Since the bubble activities are essentially a pressure fluctuation propagating in the surrounding liquid medium, cavitation techniques offer great advantages such as chemical-free reaction (Sochard, Wilhelm, and Delmas, 1998), medical non-invasive operation (Hill and Ter Haar, 1995) and acceleration of ultrasonic cleaning ability (Sato, Hubbard, English, Sievers, Ilic, Czaplewski, and Craighead, 2003).

In the application of mega-sonic cleaning, high-speed observation of the micro-pattern damaging process by Kim et al. (Kim and Kim, 2014) indicated that chaotic oscillation and splitting of microbubble clusters (rather than the liquid jet formation due to an asymmetric bubble collapse) are the main part of cleaning ability. Tanimura et al. (2010) also pointed out that the translation of bubbles contributed to cleaning action as well as bubble oscillation in the cleaning process at 28 kHz ultrasound sonication. It is clear from the above observation that the geometrical structure of solid boundaries affects the dynamical stability of nonlinear bubble oscillations.

In an acoustic field, an oscillating bubble acts as a sound source (not just a scatterer), radiating secondary pressure wave to the surroundings, and the bubble volume responds to an oscillating sound pressure that is due to a primary sound source. There therefore arise two types of secondary interactions; the radiated sound pressure exerted on neighboring bubbles leads to coupled dynamics among the oscillating bubbles (bubble-bubble interaction), while the bubble reacts against the reflected pressure wave from boundaries (bubble-boundary interaction). The main purposes of this thesis is to explore coupled nonlinear bubble oscillations in a stationary sound field. In what follows, relevant studies of coupled bubble dynamics are summarized.

1.2 Studies of bubble oscillations

1.2.1 Coupled bubble-bubble dynamics

Small cavitation bubbles repeatedly change their volume in an oscillating pressure field, accompanied frequently with jetting and splitting into fission fragments (Brennen, 2002) and subsequent coalescence. Such continuous response of the oscillating bubbles is referred to as stable acoustic cavitation (Brennen, 2013), which is employed in many engineering applications such as ultrasonic cleaning (Kim, Kim, Choi, and Kim, 2009), ultrasound imaging (Emmer, Van Wamel, Goertz, and De Jong, 2007; Helfield and Goertz, 2013) and therapy (Coussios and Roy, 2008). The interactions between sound and cavitation bubbles have been extensively investigated since the resonant phenomenon of the bubble oscillation is an important mechanism of the above applications.

The external acoustical energy is continuously localized to oscillating bubbles and subsequently released to surroundings as the secondary radiation pressure which, in turn, drives the neighboring bubbles, leading to the mutual interaction of the oscillating bubbles. We can consider the bubbles as nonlinear oscillators coupled by the radiation pressure, and readily analyze the motion of the bubble walls on the basis of fairly mathematical treatments: that is to say the spherical bubble dynamics with time-varying radii $R_i(t)$. As the dynamical behavior of the bubble population is practically of importance to improve the validity of ultrasonic techniques, the coupled oscillation of resonant bubbles has been studied intensively for many years.

At the outset of the theoretical studies on the coupled bubble oscillation (Zabolotskaya, 1984; Takahira, Akamatsu, and Fujikawa, 1994), solid mathematical consequences have been offered by linear modal analyses. Zabolotskaya (1984) analyzed linear normal modes (LNMs) of two gas bubbles pulsating in a liquid based on the Lagrangian formalism, and showed that the linear normal frequencies depend on the separation distance between the two bubbles. Takahira et al. (Takahira, Akamatsu, and Fujikawa, 1994) provided a general derivation of coupled N bubble dynamics accounting for the translational motion and deformation of the bubbles on a basis of a potential solution. The resulting eigenvalue problem concluded that the eigenfrequency of the fundamental normal mode is much smaller than that of an unbounded single bubble. However, in contrast to linear systems, extremely complex behaviors are encountered in nonlinear systems (Kerschen, Peeters, Golinval, and Vakakis, 2009). Although nonlinear spherical dynamics of a single bubble and its bifurcation structures such as subharmonic generation, period-doubling bifurcation and chaotic oscillation have been explored (Parlitz, Englisch, Scheffczyk, and Lauterborn, 1990), little is known about the bifurcation structures of the coupled bubble dynamics; most of the studies (Takahira, Yamane, and Akamatsu, 1995; Macdonald and Gomatam, 2006; Chong, Quek, Dzaharudin, Ooi, and Manasseh, 2010; Dzaharudin, Suslov, Manasseh, and Ooi, 2013; Carroll, Calvisi, and Lauderbaugh, 2013) have employed numerical techniques.

The numerical study of Takahira et al. (Takahira, Yamane, and Akamatsu, 1995) demonstrated the period-doubling bifurcation and accompanying chaotic oscillation of interacting multi-bubble systems. The fundamental feature identified in the analysis is that equal-sized bubbles with the same initial radii arranged in a symmetrical configuration all take on the same behavior similar to that of an unbounded bubble, whereas bubbles in a cluster with different initial equilibrium radii cannot oscillate independently from one another but experience a collective behavior. Macdonald and Gomatam(2006) also reported numerical results of the same collective behavior in the multi-bubble interaction of ultrasound contrast agent microbubbles.

Herein, this thesis explore nonlinear localization (Kerschen, Peeters, Golinval, and

Vakakis, 2009; Vakakis, Manevitch, Mikhlin, Pilipchuk, and Zevin, 2008; Ikeda, Harata, and Nishimura, 2013) or symmetry-breaking bifurcation (Kozłowski, Parlitz, and Lauterborn, 1995) of the mutual bubble interaction in which the total vibrational energy of the system is confined to some bubbles due to the nonlinearity of the bubble oscillation even though they are equally-sized and arranged in a symmetric configuration. Similar nonlinear phenomenon has been theoretically investigated as spatial resonance in a damped and periodically driven chain and oscillator arrays with a periodic boundary condition (Geist and Lauterborn, 1988; Geist and Lauterborn, 1991), and experimentally observed in micromechanical systems (Sato, Hubbard, English, Sievers, Ilic, Czaplewski, and Craighead, 2003; King, Aubrecht, and Vakakis, 1995). This symmetry-breaking property is one of the distinctive feature of the localized oscillation considered in this study. The assumption of the symmetrical arrangements and equal-sized assumption have been used in numerical investigation of the effects of bubble sizes and spatial arrangement on the coupled bubble dynamics (Chong, Quek, Dzaharudin, Ooi, and Manasseh, 2010; Dzaharudin, Suslov, Manasseh, and Ooi, 2013; Carroll, Calvisi, and Lauderbaugh, 2013; Ooi and Manasseh, 2005). However, the fundamental bifurcation structure of the coupled bubble dynamics has not been addressed because most of the above studies are based on numerical investigation.

The linear modal analyses have been definitely powerful tools for interpreting the underlying linear system. However, they are still inadequate to describe properly the complicated nonlinear phenomena. For a general survey of the bifurcation structure of the coupled bubble dynamics, analytical investigation of nonlinear normal modes (NNMs) (Kerschen, Peeters, Golinval, and Vakakis, 2009; Vakakis, Manevitch, Mikhlin, Pilipchuk, and Zevin, 2008; Li, Ji, and Hansen, 2006) is an essential approach to a greater insight on the structural nature of the multi-bubble dynamics. At the first attempt of NNMs, Rosenberg (Rosenberg, 1960; Rosenberg, 1962; Rosenberg, 1966) extended straightforwardly the concept of LNMs to nonlinear vibration systems and defined a NNM as a vibration *in unison* where all mass points in the system display periodic motions with the same period. In the definition, all displacements pass through their equilibrium points and reach their extreme values simultaneously. It should be also noted that NNMs inherit the invariance property of LNMs (i.e., motions that depart from the NNM confined in it for all time), which is exploited to derive the NNMs in the perturbation analysis of this study.

There have been a few studies which used a perturbative method to obtain the steady-state solution of bubble oscillation. Prosperetti (1974) presented a second order steady-state solution of Rayleigh's equation of motion for the bubble wall by means of an asymptotic expansion method. The analytical result enabled it evident to predict the multivalued solution of the nonlinear oscillation and the unstable region of subharmonic resonance as well as their hysteresis behavior. Francescutto (Francescutto and Nabergoj, 1983) used an asymptotic method of multiple scales to obtain explicit and simpler formulas for the second order approximate solution. Nevertheless, nonlinear resonance of the vibration modes among multiple bubbles are still unclear since these results are for a single bubble. We employ the method of multiple scales (Li, Ji, and Hansen, 2006; Nayfeh and Mook, 2008) to derive NNMs of the coupled bubble oscillation and investigate the internal resonance (Li, Ji, and Hansen, 2006) of the steady-state amplitude and the phase shift.

In the present study, we will restrict the analysis to a resonant pair of two bubbles. In order not to limit the generality, the bubble sizes are allowed to be different in the perturbation analysis (Section 3), but assumed to be similar so that the two uncoupled natural frequencies of isolated bubbles have a slight difference by the order of $O(\epsilon^2)$ where ϵ is a dimensionless oscillation amplitude. Since the aim of this paper is to investigate the bifurcation structure of the radial dynamics of a resonant pair of bubbles, the separation distance of the bubbles is assumed to be unchanged by the translational instability (Koch, Kurz, Parlitz, and Lauterborn, 2011) due to Bjerknes forces, while it is important to account for the transient response and hysteresis property for a full understanding of the bubble structure dynamics (Barbat, Ashgriz, and Liu, 1999). The circumstances of a fixed bubble distance is not improbable but achieved in the case of surface cavitation bubbles attached on a solid surface (Bremond, Arora, Ohl, and Lohse, 2006; Bremond, Arora, Dammer, and Lohse, 2006). Because of the adhesion between the bubble and wall surface the bubble mobility is decreased, and the bubble distances tends to remain almost fixed. Additionally, the effect of the wall boundary is replaced with a mirror image of the real bubble. This allows the dynamics of the hemispherical bubble to be well described by the Rayleigh–Plesset equation for a spherical bubble in an unbounded space.

1.2.2 Bubble cluster oscillation and translation

Growth of gas bubble nuclei under pressure fluctuations of the surrounding liquid and the subsequent oscillations are termed acoustic cavitation (Apfel, 1984; Neppiras, 1984; Brennen, 2013) and the subsequent dynamics of nucleated cavitation bubbles plays an important role in many applications such as ultrasonic cleaning. This is due to the fact that inputted acoustic energy is effectively converted, through bubble oscillations in volume and translational instability of fissioned bubbles (Brennen, 2002; Delale and Tunç, 2004), into mechanical energy within localized spots (Krefting, Mettin, and Lauterborn, 2004; Kim and Kim, 2014). Since oscillating and translating bubble clusters are accompanied frequently with violent collapses (Lauterborn and Bolle, 1975; Kreider, Crum, Bailey, and Sapozhnikov, 2011), cavitation can give rise to undesired disruptive damage to surrounding solid materials (i.e., the so-called cavitation erosion).

Hydrodynamic interactive forces acting on oscillating bubbles were first studied by Bjerknes (Bjerknes, 1906). In the classical theory, two synchronously oscillating bubbles are subject to mutual attractive force, while two bubbles oscillating out-of-phase experience mutual repulsion. These kinds of mutual forces are known as secondary Bjerknes force and distinguished from the primary Bjerknes force that results from interaction with an external sound source. The magnitude of the secondary Bjerknes forces is proportional to the intensities of radial oscillation of each bubble and decays inversely with the square of the separation distance between the bubbles. It follows from the classical description that the secondary Bjerknes effect is mathematically equivalent to translational motion of one oscillating dipole subject to monopole radiation of the other.

More complicated behaviors of oscillating bubbles have been demonstrated theoretically by extending the classical theory of Bjerknes. One of earliest studies of Crum (Crum, 1975) assumed linear bubble oscillation and derived a simple expression of the secondary Bjerknes force after time-averaging over one oscillation period of the imposed sound frequency. Barbat et al. (Barbat, Ashgriz, and Liu, 1999) modified Crum's formula by accounting for damped oscillation of spherical bubbles. The resulting phase shift between two resonant bubbles allowed a stable equilibrium point at which the sign of the secondary Bjerknes force changes. Oguz and Prosperetti (1990) developed a set of ordinary differential equations for the coupled nonlinear dynamics between translational motion and bubble pulsation in a potential flow. Subsequently, Harkin et al. (Harkin, Kaper, and Nadim, 2001) classified patterns of translational motion of a couple of oscillating bubbles for the case of linear or weakly nonlinear forcing by means of the dynamical analysis of Oguz and Prosperetti (1990), drawing a conclusion that the classical theory was valid only for a large separation distance and weakly forced bubbles. Near-field interaction between bubbles is often results in nonspherical bubble deformation and there is thus a need to handle it using the boundary element method (Pelekasis and Tsamopoulos, 1993a; Pelekasis and Tsamopoulos, 1993b). Further extensions to the discussion on the secondary Bjerknes force between single bubbles have been proposed by several authors, which consider viscous liquid (Pelekasis, Gaki, Doinikov, and Tsamopoulos, 2004), high-intensity sound pressure (Doinikov, 2002), multipole interaction or higher spherical harmonics (Doinikov and Zavtrak, 1995), drag and history forces on an oscillating bubble (Kang and Leal, 1988; Magnaudet and Legendre, 1998; Reddy and Szeri, 2002) and decoupling of the radial dynamics from the translational motion (Krefting, Toilliez, Szeri, Mettin, and Lauterborn, 2006).

Validity of the time-averaged secondary Bjerknes force has been experimentally investigated for single bubbles in early works of Crum (1975) and Barbat et al. (1999), and more recently in the ultrasonic frequency range by Yoshida et al. (2011) and Jiao et al. (2015). The coupled radial and translational model developed by Doinikov (2002) was extended to microbubble-wall interaction by Xi et al. (2012). However, studies on the translational motion of an oscillating bubble ”cluster” are rather limited, despite its practical importance. While the translational dynamics of cavitation clouds was recently investigated by Nowak and Mettin (2014) and Johnston et al. (2014), in an ultrasonic frequency range, the cluster dynamics could not be resolved in detail because of limitation in temporal and spatial resolution of the optical imaging. In this work, we aim to propose an experimental technique to resolve the dynamics of a translating bubble cluster under sonication and analyze the experimental observation with extended theory.

The goal of this study is to show the validity of the classical Bjerknes theory to a spherical cluster oscillation interacting with solid boundaries. In doing so, we develop a lower frequency vibration system (Jameson and Davidson, 1966; Baird, 1968; Sudo and Hashimoto, 1988) in order to resolve the entire picture of bubble cluster activities subject to a stationary sound field after the example of Nyborg and Rodgers (1976) and Crum (1975). In what follows, we explain the experimental method and high-speed imaging of cluster events (bubble fission, clustering, cluster oscillation and translation, interaction with solid boundaries), present the temporal evolution of cluster size and translation, and finally analyze the translational dynamics with extended Bjerknes theory.

1.2.3 Interaction with boundaries

For translational dynamics of an oscillating bubble near a boundary, a temporal evolution of the pressure boundary data and its distribution are of necessity because the hydrodynamics force due to the secondary sound wave (i.e., secondary Bjerknes force) is given by a product of the pressure gradient at the bubble position and the volume of the oscillating bubble; the translational motion of bubble is driven by the radiation pressure wave reflected from neighboring wall boundaries interacting with the bubble volume oscillation. A schematic of an oscillating bubble near a wall boundary is shown in Fig. 1.1. The phase difference between the reflected wave and the bubble oscillation should therefore be well quantified for accurately describing the bubble translational dynamics. Thus, it is a need to consider the structural dynamics of the deformable boundary coupled with the fluid dynamics of the bubble oscillation.

In the early stage of studies of the bubble-wall interactions, one of primary concerns of these studies has been growth and collapse dynamics of a transient cavitation bubble. Formation of a re-entrant jet and following topological change of a collapsing bubble have been numerically explored for the case of a rigid boundary (Wiedemair, Tukovic, Jasak, Poulikakos, and Kurtcuoglu, 2014; Plesset and Chapman, 1971; Blake, Robinson, Shima, and Tomita, 1993; Blake, Taib, and Doherty, 1986; Zhang, Duncan, and Chahine, 1993; Wang, 2014) and the case of a free surface (Wang, Yeo, Khoo, and Lam, 1996; Blake, Taib, and Doherty, 1987; Dommermuth and Yue, 1987; Pelekasis, Tsamopoulos, and Manolis, 1992; Robinson, Blake, Kodama, Shima, and Tomita, 2001; Li, Sun, Zong, and Dong, 2012). The basic feature identified in these studies is the direction reversal of the bubble motion at collapse phase; the re-entrant jet directed toward (rigid boundary) or away (free surface) from the boundary due to the difference of the dynamical boundary condition at the wall. However, further complex phenomena have been numerically demonstrated for the case of an elastic wall boundary, and some experimental evidences were also provided (Shima, Tomita, Gibson, and Blake, 1989 and Gisbon and Blake, 1980). Rigid and free boundaries are particular examples of a general compliant boundary.

There have been two common numerical methods for the modeling of a compliant wall dynamics. In the first case, a spring-backed membrane (Duncan and Zhang, 1991; Farhangmehr, Aghdam, Shervani-Tabar, Parvizi, Ohl, and Khoo, 2014; Gisbon and Blake, 1980; Gibson and Blake, 1982) is used for the reduced model of a compliant wall boundary. In the second case, the compliant boundary is modeled as an elastic fluid (Ohl, Klaseboer, and Khoo, 2009; Klaseboer, Turangan, and Khoo, 2006; Wang, Zhang, Liu, and Zeng, 2013; Yu, Lin, Xu, Liu, and Shen, 2015; Yang and Church, 2005; Klaseboer and Khoo, 2004). A direct numerical simulation of the elastic body by the

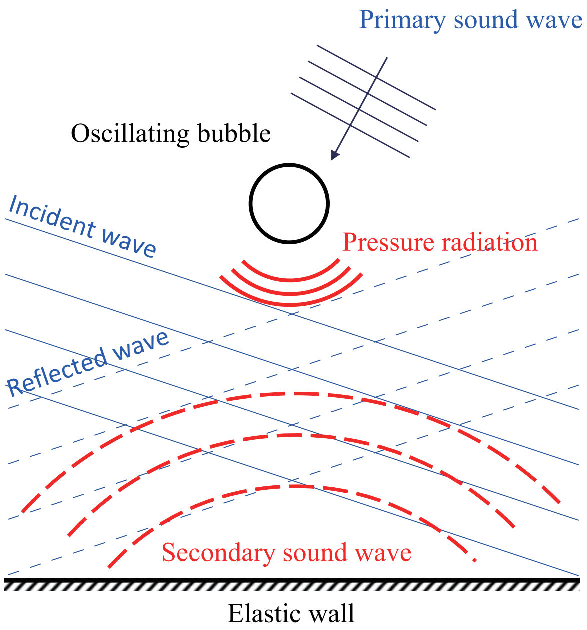
Primary sound wave
Oscillating bubble
Incident wave
Pressure radiation
Reflected wave
Secondary sound wave
Elastic wall

FIGURE 1.1: A schematic of bubble-wall interaction.

finite element method (FEM) is a comprehensive and straightforward approach (Duncan, Milligan, and Zhang, 1996; Miao and Gracewski, 2008; Kalumuck, Duraiswami, and Chahine, 1995), and also offers verification of other reduced wall models. An image method (Hsiao et al., 2013; Soh, 1992) is also used to develop a potential solution which satisfies the dynamics boundary conditions on the wall surface.

One of the reason for the success of the two common models are simplicity and explicitness of the numerical implementation and efficiency of computation. However, in view of the structural dynamics of elastic boundaries, both of the models are limited in determining physically proper parameters. In this thesis, an eigenvalue analysis of a circular elastic plate is performed to obtain eigenfunctions and their eigenvalues of a spring-backed membrane model, which describes the unknown parameters used in the model.

1.3 Contribution and outline

The main contributions of this thesis are:

- Development of nonlinear normal modes of coupled oscillation of two spherical bubbles
- Experimental observation of an oscillating bubble cluster and modeling of the translational dynamics with the classical Bjerknes theory.
- Formulation of linear normal modes of a circular elastic plate, and derivation of the equation of motion of the elastic body surface coupled with an oscillating bubble dynamics
- Numerical implementation of the coupled dynamics of an oscillating bubble and a compliant wall, and quantification of the effect of the thickness and the rigidity the elastic layer.

Nonlinear modal analysis of coupled oscillation of two spherical bubbles is presented in Chapter 2. Analytical expressions of nonlinear normal modes (NNMs) and steady-state oscillations are derived and underlying bifurcation structures are discussed. Chapter 3 is devoted to experiment and modeling of translational dynamics of an oscillating bubble cluster. The classical theory of the translational dynamics of a single bubble is extended to the bubble cluster and compared with the experimental result. Chapter 4 presents an analytical model and the basic equation for the coupled nonlinear dynamics of an oscillating bubble near an elastic wall. A numerical method to solve the fluid-structure coupled model presented in the previous section is summarized. Numerical results of the coupled bubble-wall dynamics are shown to discuss the effect of the thickness of the elastic wall on the translational dynamics of the oscillating bubble. Concluding remarks and suggestions for future work are summarized in Chapter 5.

Chapter 2

Nonlinear modal analysis of coupled two-bubble oscillation

In this chapter, nonlinear modal analysis of acoustically-coupled two-bubble oscillators is presented to explore the bifurcation structure of the steady-state dynamics and underlying nonlinear normal modes. Bifurcation structures of coupled nonlinear oscillation of two spherical gas bubbles subject to a stationary sound field is explored by means of nonlinear modal analysis. The goal of this paper is to describe an energy localization phenomenon of coupled two-bubble oscillators, resulting from symmetry-breaking bifurcation of the steady-state oscillation. Approximate asymptotic solutions of NNMs and steady state oscillation are obtained based on the method of multiple scales. It is found that localized oscillation arises in a neighborhood of the localized normal modes. The analytical solutions of the amplitude and the phase shift of the steady-state oscillation are compared to numerical results and found to be in good agreement within the limit of small-amplitude oscillation. For larger amplitude oscillation, a bifurcation diagram of the localized solution as a function of the driving frequency and the separation distance between the bubbles is provided in the presence of the thermal damping. The numerical results show that the localized oscillation can occur for a fairly typical parameter range used in practical experiments and simulations in the early literatures.

2.1 Model equation

2.1.1 Rayleigh–Plesset equation

Suppose that two gas bubbles are separated by a fixed distance in a liquid driven by a stationary sound field sketched in Fig. 2.1. The wave length is assumed larger enough for the two bubbles to experience the equal driving pressure. Bubble oscillations are inertially controlled by periodic pressure change in the far field, and develop a secondary sound field without distorting each others' sphericity. The radiation pressure induced by one of the bubbles, bubble 1, measured at the center of the other bubble, bubble 2, is

$$p_r\left(d,t\right) = \frac{\rho_L}{4\pi d}\frac{d^2 V_1(w_t)}{dw_t^2}\bigg|_{w_t = t-\frac{d}{c}} \tag{2.1}$$

where ρ_L is the undisturbed liquid density, V_1 is the time-varying volume of bubble 1, d is the separation distance between the bubble centers which is enough larger than the wave length for the bubbles to remain spherical with the time-varying radii $R_1(t)$ and $R_2(t)$, respectively, and c is the (constant) speed of sound. The radiation pressure is evaluated in the retarded time-frame, $w_t = t - d/c$, due to the finite speed of sound. Eq. (2.1) is exerted on the neighboring bubbles as an additional driving pressure, and their resulting spherical dynamics are coupled with each other.

Herein, the liquid is assumed to be cold, and the vapor pressure is omitted from the bubble contents, while the linear thermal damping (Devin Jr, 1959; Chapman and Plesset, 1971) was used in the numerical simulation (Section 4). The contribution of the translational motion is higher-order correction and can be neglected in the following perturbation analysis in Section 3. The model limitation of neglecting the translational dynamics is given in Appendix A based on a scale analysis. Shape and dissolution instabilities (Koch, Kurz, Parlitz, and Lauterborn, 2011; Hilgenfeldt, Lohse, and Brenner, 1996) are neglected while they are generally needed to account for lifetimes of oscillating cavitation bubbles. The bubble fission (Brennen, 2002) and rectified diffusion (Eller and Flynn, 1965) are also not taken into account because the scope of this study is to

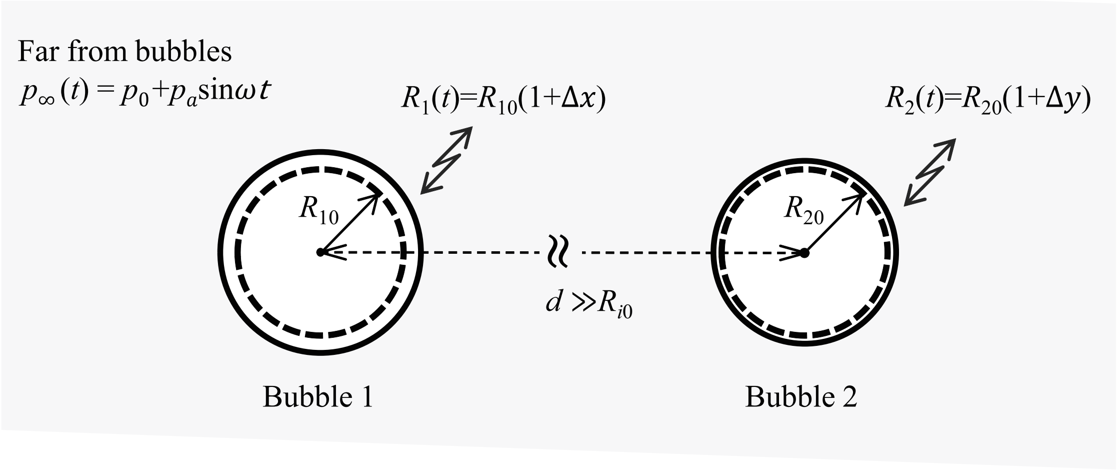
Far from bubbles
$p_\infty(t) = p_0 + p_a \sin\omega t$
$R_1(t) = R_{10}(1+\Delta x)$
$R_2(t) = R_{20}(1+\Delta y)$
R_{10}
R_{20}
$d \gg R_{i0}$
Bubble 1
Bubble 2

FIGURE 2.1: Schematic of two oscillating bubbles.

identify the bifurcation structure of the spherical bubble oscillators.

2.1.2 Equations of radial motion

For spherical dynamics of an oscillating bubble of radius $R_i(t)$, we use a modified form of the coupled Keller–Miksis equation (Keller and Miksis, 1980) which accounts for the liquid compressibility to the first order. Adding the radiation pressure, $p_r(d,t)$, as a secondary driving term into the external driving pressure and neglecting coupling terms of higher order (Parlitz, Englisch, Scheffczyk, and Lauterborn, 1990; Prosperetti and Lezzi, 1986) lead to the equation of radial motion of bubble 2 (Mettin, Akhatov, Parlitz, Ohl, and Lauterborn, 1997):

$$\begin{aligned}\left(1-\frac{\dot{R}_2}{c}\right)R_2\ddot{R}_2+\left(\frac{3}{2}-\frac{\dot{R}_2}{2c}\right)\dot{R}_2^2 =& \frac{1}{\rho_L}\left(1+\frac{\dot{R}_2}{c}\right)\left[p_2(R_2,\dot{R}_2)-p_0-p_{\mathrm{ex}}(t)\right]\\ &+\frac{\dot{R}_2}{\rho_L c}\frac{d}{dt}\left[p_2(R_2,\dot{R}_2)-p_{\mathrm{ex}}(t)\right]\\ &-\left.\frac{R_1^2\ddot{R}_1+2R_1\dot{R}_1^2}{d}\right|_{w_t=t-\frac{d}{c}}\end{aligned} \tag{2.2}$$

where dots denote time differentiation, ρ_L is the equilibrium density of the liquid, p_0

is the hydrostatic pressure in the far field, $p_{\mathrm{ex}}(t) = p_a \sin \omega t$ is the external driving pressure, and $p_2(R_2, \dot{R}_2)$ is the liquid pressure at the bubble wall. Note that the coupling terms are evaluated with respect to the retarded time (Doinikov, Manasseh, and Ooi, 2005), $t^* - \tau^*$, where $\tau^* = d^*/C$ is the dimensionless retardation time.

It is assumed that the behavior of the gas in the bubble is approximately polytropic and set

$$p_2 = \left(p_0 + \frac{2S}{R_{20}}\right)\left(\frac{R_{20}}{R_2}\right)^{3\kappa} - \frac{2S}{R_2} - \frac{4\mu_L \dot{R}_2}{R_2} \tag{2.3}$$

where R_{20} is the equilibrium radius of bubble 2, S is the surface tension, κ is the polytropic index, and μ_L is the liquid viscosity. The equations for bubble 1 is obtained by exchanging the indices 1 and 2 in Eqs. (2.2) and (2.3). The adiabatic natural frequency of an uncoupled bubble of R_0 in radius at rest in an unbounded space is given by

$$\omega_N = \frac{1}{R_0}\left[\frac{3\gamma p_0}{\rho_L} + \frac{2(3\gamma - 1)S}{\rho_L R_0}\right]^{\frac{1}{2}} \tag{2.4}$$

where γ is the ratio of specific heats.

2.1.3 Dimensionless form

In the following perturbation method, it is convenient to nondimensionalize the equations of motion. Substituting $R_1 = R_{10}(1 + \Delta x)$, $R_2 = R_{20}(1 + \Delta y)$ and $t = \omega_N^{-1} t^*$, the equations motion of the two bubbles are reduced to

$$\begin{aligned}\left(1 - \frac{\dot{\Delta x}}{C}\right)(1 + \Delta x)\,\ddot{\Delta x} + \frac{3}{2}\left(1 - \frac{\dot{\Delta x}}{3C}\right)\dot{\Delta x}^2 \\ = \left(1 + \frac{\dot{\Delta x}}{C}\right)\left[p_1^*(\Delta x, \dot{\Delta x}) - \mathrm{\mathbf{Eu}}(1 + A^* \sin \omega_f t^*)\right] \\ + \frac{\Delta x}{C}\frac{d}{dt^*}\left[p_1^*(\Delta x, \dot{\Delta x}) - \mathrm{\mathbf{Eu}} A^* \sin \omega_f t^*\right] \\ - \frac{R^{*3}}{d^*}\left[(1 + \Delta y)^2 \ddot{\Delta y} + 2\dot{\Delta y}^2 (1 + \Delta y)\right]\Bigg|_{w_t = t^* - \frac{d}{c}},\end{aligned} \tag{2.5}$$

$$\begin{aligned}\left(1-\frac{R^*\Delta\dot{y}}{C}\right)(1+\Delta y)\,\Delta\ddot{y}+\frac{3}{2}\left(1-\frac{R^*\Delta\dot{y}}{3C}\right)\Delta\dot{y}^2 \\ =\left(1+\frac{R^*\Delta\dot{y}}{C}\right)\left[p_2^*(\Delta y,\Delta\dot{y})-\frac{\text{Eu}}{R^{*2}}(1+A^*\sin\omega_f t^*)\right] \\ +\frac{R^*\Delta y}{C}\frac{d}{dt^*}\left[p_2^*(\Delta y,\Delta\dot{y})-\frac{\text{Eu}}{R^{*2}}A^*\sin\omega_f t^*\right] \\ -\frac{1}{d^*R^{*2}}\left[(1+\Delta x)^2\Delta\ddot{x}+2\Delta\dot{x}^2(1+\Delta x)\right]\Bigg|_{w_t=t^*-\frac{d}{c}}\end{aligned} \tag{2.6}$$

where Δ symbolizes small perturbation of the corresponding variables and $p_1^*(\Delta x,\Delta\dot{x})$ and $p_2^*(\Delta y,\Delta\dot{y})$ are the dimensionless liquid pressures at the bubble walls given by

$$p_1^*=\left(\text{Eu}+\frac{2}{\text{We}}\right)\left(\frac{1}{1+\Delta x}\right)^{3\kappa}-\frac{2}{\text{We}}\frac{1}{1+\Delta x}-\frac{4}{\text{Re}}\frac{\Delta\dot{x}}{1+\Delta x}, \tag{2.7}$$

$$p_2^*=\left(\frac{\text{Eu}}{R^{*2}}+\frac{2}{\text{We}R^{*3}}\right)\left(\frac{1}{1+\Delta y}\right)^{3\kappa}-\frac{2}{\text{We}R^{*3}}\frac{1}{1+\Delta y}-\frac{4}{\text{Re}R^{*2}}\frac{\Delta\dot{y}}{1+\Delta y}. \tag{2.8}$$

Here, all the dimensionless parameters are defined with respect to R_{10} and ω_N as

$$\begin{aligned}&R^*=\frac{R_{20}}{R_{10}},\ d^*=\frac{d}{R_{10}},\\ &A^*=\frac{p_a}{p_0},\ \omega_f=\frac{\omega}{\omega_N},\ C=\frac{c}{\omega_N R_{10}},\\ &\text{Eu}=\frac{p_0}{\rho_L\omega_N^2R_{10}^2},\ \text{We}=\frac{\rho_L\omega_N^2R_{10}^3}{S},\ \text{Re}=\frac{\rho_L\omega_N R_{10}^2}{\mu_L}\end{aligned} \tag{2.9}$$

where R^* is the ratio of the initial radii, d^* is the dimensionless separation distance, A^* is the driving pressure normalized by the static pressure in the far field, ω_f is the ratio between the sound frequency and the adiabatic natural frequency of an isolated bubble, C is the speed of sound in the liquid normalized by the characteristic bubble wall speed, and Eu, We and Re are Euler, Weber and Reynolds number, respectively. Since the temporal time is nondimesionalized using the natural frequency of an isolated bubble, the order of the velocity and that of the acceleration of the bubble wall do not change after time differentiation, given that the excitation frequency is near the natural frequency of the bubble ($\omega_f \approx 1$). Therefore, the order of $\Delta\dot{x}$ and that of $\Delta\ddot{x}$ are assumed the same as that of Δx in the primary resonance considered in this study. Throughout the perturbation analysis, we can assume small amplitude oscillation and set the order of Δx, Δy and their derivatives to be a small but finite dimensionless quantity ϵ.

2.1.4 Linear normal modes

Linear truncation of Eqs. (2.5) to (2.8) with respect to Δ leads to

$$\ddot{\Delta x} + c_x \dot{\Delta x} + \omega_x^2 \Delta x = -e_x \left(1 + \Delta x\right) \sin \omega_f t^* - \mu_x \ddot{\Delta y} + \mu_x \tau^* \dddot{\Delta y}, \tag{2.10}$$

$$\ddot{\Delta y} + c_y \dot{\Delta y} + \omega_y^2 \Delta y = -e_y \left(1 + \Delta y\right) \sin \omega_f t^* - \mu_y \ddot{\Delta x} + \mu_y \tau^* \dddot{\Delta x} \tag{2.11}$$

where ω_i $(i = x, y)$ is the partial natural frequency of the individual bubbles, c_i is the damping coefficient due to the viscous and radiation effects, μ_i is the strength of the acceleration's coupling term which is inversely proportional to the separation distance, and e_i is the driving amplitude of the acoustic pressure. Here, the third order derivatives in Eqs. (2.10) and (2.11) are approximated by linear solution:

$$\dddot{\Delta x} \approx -c_x \ddot{\Delta x} - \omega_x^2 \dot{\Delta x} - e_x \omega_f \cos \omega_f t^*, \tag{2.12}$$

$$\dddot{\Delta y} \approx -c_y \ddot{\Delta y} - \omega_y^2 \dot{\Delta y} - e_y \omega_f \cos \omega_f t^*. \tag{2.13}$$

Substituting Eqs. (2.12) and (2.13) into Eqs. (2.10) and (2.11) yields

$$\begin{aligned} \ddot{\Delta x} + c_x \dot{\Delta x} + \omega_x^2 \Delta x = &- e_x \left(1 + \Delta x\right) \sin \omega_f t^* - \mu_x \left(1 + \tau^* c_x\right) \ddot{\Delta y} - \mu_x \tau^* \omega_x^2 \dot{\Delta y} \\ &- \mu_x \tau^* e_x \omega_f \cos \omega_f t^*, \end{aligned} \tag{2.14}$$

$$\begin{aligned} \ddot{\Delta y} + c_y \dot{\Delta y} + \omega_y^2 \Delta y = &- e_y \left(1 + \Delta y\right) \sin \omega_f t^* - \mu_y \left(1 + \tau^* c_y\right) \ddot{\Delta x} - \mu_y \tau^* \omega_y^2 \dot{\Delta x} \\ &- \mu_y \tau^* e_y \omega_f \cos \omega_f t^* \end{aligned} \tag{2.15}$$

Eq. (2.14) and (2.15) are given in a vector form:

$$\mathrm{M}\ddot{\mathrm{x}} + \mathrm{C}\dot{\mathrm{x}} + \left(\mathrm{K} - \mathrm{F}\sin\omega_f t^*\right)\mathrm{x} = \mathbf{0} \tag{2.16}$$

where inhomogeneous terms with respect to x= $(\Delta x, \Delta y)^T$ are dropped out. Expressions for these parameters and matrices M, C, K and F are listed in Appendix A.2. Eq. (2.16) is a damped Mathieu-type equation driven by a harmonic excitation, and the fourth term on the left hand side gives rise to parametric instability when the driving amplitude and frequency satisfy specific conditions. However, we can neglect this parametric resonance term in the small amplitude approximation.

In general, a N degrees-of-freedom linear oscillation system can have N natural frequencies and corresponding LNMs which are derived from the eigenvalue problem of $\mathrm{M}^{-1}\mathrm{K}$. We denote by ω_{L1} and ω_{L2} the modal natural frequencies of the LNMs of the system as

$$\omega_{\mathrm{L1}}^2 = \frac{\omega_x^2 + \omega_y^2 - \sqrt{(\omega_x^2 + \omega_y^2)^2 - 4\xi\omega_x^2\omega_y^2}}{2\xi}, \tag{2.17}$$

$$\omega_{\mathrm{L2}}^2 = \frac{\omega_x^2 + \omega_y^2 + \sqrt{(\omega_x^2 + \omega_y^2)^2 - 4\xi\omega_x^2\omega_y^2}}{2\xi} \tag{2.18}$$

where

$$\xi = 1 - \mu_x\mu_y\left(1 + c_x\tau^*\right)\left(1 + c_y\tau^*\right). \tag{2.19}$$

In the absence of the retarded effect ($\tau^* = 0$), Eqs. (2.17) and (2.18) are identical with that of Zabolotskaya (1984) termed as the partial natural frequency in the paper. Particularly for equally-sized two bubbles, the above equations become

$$\omega_{\mathrm{L1}} = \frac{\omega_N}{\sqrt{1 + d^{*-1}}}, \tag{2.20}$$

$$\omega_{\mathrm{L2}} = \frac{\omega_N}{\sqrt{1 - d^{*-1}}}. \tag{2.21}$$

The corresponding oscillations are in-phase and out-of-phase, respectively. The corresponding LNMs are described in Fig. 2.2 where the dimensionless parameters used are for case given in Table 2.1. The LNMs are uniquely specified by the ratio between the inertia and stiffness of the system and invariant with respect to the state of motion; L1 and L2 are depicted as a straight vertical line in Fig. 2.2 which indicates that the LNMs are not functions of the oscillation amplitude. Note that the forced oscillation of a two degree of freedom system has two resonance points in the neighborhood of the LNMs. Therefore, it is worth exploring normal modes and their normal natural frequencies for understanding the global dynamics of the coupled oscillating system. In the next section, we readily extend the concept of LNMs to the nonlinear modal analysis of the two-bubble oscillators.

2.2 Perturbation analysis

2.2.1 Small-amplitude approximation

In order to construct perturbative solutions based on a Taylor series expansion, we approximate Eqs. (2.5) to (2.8) by truncated equations considering terms to $O(\epsilon^3)$

$$\begin{aligned}\ddot{\Delta x} + c_x\dot{\Delta x} + \omega_x^2\Delta x =& - b\,(1-\Delta x)\,\dot{\Delta x}^2 - \beta_{xx}\Delta x^2 - \beta_{xxx}\Delta x^3 - e_x\sin\omega_f t^* - \mu_x\ddot{\Delta y}\\ &- \mu_x\tau^*\omega_x^2\dot{\Delta y}, \qquad (2.22)\\ \ddot{\Delta y} + c_y\dot{\Delta y} + \omega_y^2\Delta y =& - b\,(1-\Delta y)\,\dot{\Delta y}^2 - \beta_{yy}\Delta y^2 - \beta_{yyy}\Delta y^3 - e_y\sin\omega_f t^* - \mu_y\ddot{\Delta x}\\ &- \mu_y\tau^*\omega_x^2\dot{\Delta x} \qquad (2.23)\end{aligned}$$

where β_{xx}, β_{yy}, β_{xxx} and β_{yyy} are parameters associated with the nonlinear terms (see Appendix A.2). The other parameters associated with the linear terms are the same as Eq. (2.16) except that $b = 3/2$ is a constant.

For the sake of the perturbation analysis, we assume that the damping coefficients, c_i, and the coupling strength, μ_i, are of the order of $O(\epsilon^2)$, and the sound amplitude, e_i, is of the order of $O(\epsilon^3)$ so that all the terms in Eqs. (2.22) and (2.23) are of the order of $O(\epsilon^3)$ and set

$$c_i = \epsilon^2 \hat{c}_x, \;\; \mu_i = \epsilon^2 \hat{\mu}_i, \;\; e_i = \epsilon^3 \hat{e}_i. \tag{2.24}$$

Since the retardation time is assumed to be small compared to the driving period ($\tau^* \ll 2\pi$) in the derivation (Doinikov, Manasseh, and Ooi, 2005), the order of τ^* is set at $O(1)$. This indicates that the following analysis is restricted to relatively small separation distance ($d^* \ll 2\pi C$) with the presence of the retarded effect.

2.2.2 Perturbation solution

To obtain the approximate solution of Eqs. (2.22) and (2.23), we use the method of multiple scales (Nayfeh and Mook, 2008; Nayfeh, 2008). Instead of using the driving frequency, ω_f, as a control parameter, we use a detuning parameter, $\sigma = \epsilon^2 \hat{\sigma}$, which indicates the deviation of ω_f from ω_x such that

$$\omega_f = \omega_x + \epsilon^2 \hat{\sigma}. \tag{2.25}$$

Here, we consider nearly equal-sized bubbles and denote the difference of the natural frequencies of the bubbles by $\alpha = \epsilon^2 \hat{\alpha}$ in the form

$$\omega_y = \omega_x + \epsilon^2 \hat{\alpha}. \tag{2.26}$$

On the basis of the method of multiple scales, we introduce three time scales $t_0 = t^*$, $t_1 = \epsilon t^*$ and $t_2 = \epsilon^2 t^*$. Accordingly, the total derivative is $d/dt^* = D_0 + \epsilon D_1 + \epsilon^2 D_2$ where $D_k = \partial / \partial t_k$ denotes partial differentiation with respect to t_k. The approximate solution of Δx and Δy as functions of these multiple time scales are assumed in the form

$$\Delta x\left(t_0,t_1,t_2\right)=\epsilon x_1+\epsilon^2 x_2+\epsilon^3 x_3+\cdots\,, \tag{2.27}$$

$$\Delta y\left(t_0,t_1,t_2\right)=\epsilon y_1+\epsilon^2 y_2+\epsilon^3 y_3+\cdots \tag{2.28}$$

where successively determined x_i and y_i are the solution of the ϵ^i order. After substituting Eqs. (2.24) to (2.28) into Eqs. (2.22) and (2.23) and collect terms of same powers of ϵ, we find a set of partial differential equations.

$O(\epsilon)$:

$$D_0^2 x_1+\omega_x^2 x_1=0, \tag{2.29}$$

$$D_0^2 y_1+\omega_x^2 y_1=0. \tag{2.30}$$

$O(\epsilon^2)$:

$$D_0^2 x_2+\omega_x^2 x_2=-2D_0D_1x_1-b\left(D_0x_1\right)^2-\beta_{xx}x_1^2, \tag{2.31}$$

$$D_0^2 y_2+\omega_x^2 y_2=-2D_0D_1y_1-b\left(D_0y_1\right)^2-\beta_{yy}y_1^2. \tag{2.32}$$

$O(\epsilon^3)$:

$$\begin{aligned}D_0^2 x_3+\omega_x^2 x_3=&-D_1^2x_1-2D_0D_2x_1-2D_0D_1x_2\\&-2b(D_0x_1)(D_1x_1)+2b(D_0x_1)(D_0x_2)+bx_1(D_0x_1)^2\\&-\hat{c}_xD_0x_1-\hat{\mu}_x\tau^*\omega_x^2D_0y_1-2\beta_{xx}x_1x_2-\beta_{xxx}x_1^3\\&-\hat{\mu}_xD_0^2y_1-\hat{e}_x\sin\omega_f t^*,\end{aligned} \tag{2.33}$$

$$\begin{aligned} D_0^2 y_3 + \omega_x^2 y_3 = &-D_1^2 y_1 - 2D_0 D_2 y_1 - 2D_0 D_1 y_2 \\ &- 2b(D_0 y_1)(D_1 y_1) + 2b(D_0 y_1)(D_0 y_2) + b y_1 (D_0 y_1)^2 \\ &- \hat{c}_y D_0 y_1 - \hat{\mu}_y \tau^* \omega_x^2 D_0 x_1 - 2\beta_{yy} y_1 y_2 - \beta_{yyy} y_1^3 - \hat{\mu}_y D_0^2 x_1 - \hat{e}_y \sin \omega_f t^* \\ &- 2\omega_x \hat{\alpha} y_1. \end{aligned} \tag{2.34}$$

The general solutions of Eqs. (2.29) and (2.30) are

$$x_1 = A_x(t_1, t_2) \mathrm{e}^{i\omega_x t_0} + cc, \tag{2.35}$$

$$y_1 = A_y(t_1, t_2) \mathrm{e}^{i\omega_x t_0} + cc \tag{2.36}$$

where A_x and A_y are the complex amplitude, and cc stands for the complex conjugate of the preceding terms on the right hand side. Substituting Eqs. (2.35) and (2.36) into Eqs. (2.31) and (2.32) yields

$$D_0^2 x_2 + \omega_x^2 x_2 = -2iD_1 A_x \mathrm{e}^{i\omega_x t_0} + bA_x^2 \mathrm{e}^{2i\omega_x t_0} - \beta_{xx} x_1^2, \tag{2.37}$$

$$D_0^2 y_2 + \omega_x^2 y_2 = -2iD_1 A_y \mathrm{e}^{i\omega_x t_0} + bA_x^2 \mathrm{e}^{2i\omega_x t_0} - \beta_{yy} y_1^2. \tag{2.38}$$

The first terms on the right hand side of Eqs. (2.37) and (2.38) produce secular terms in x_2 and y_2, respectively, which make the solution grow unboundedly in time. To eliminate the secular terms, we exert solvability conditions:

$$D_1 A_x(t_1, t_2) = 0, \tag{2.39}$$

$$D_1 A_y(t_1, t_2) = 0. \tag{2.40}$$

Solving Eqs. (2.39) and (2.40), A_x and A_y turn out to be a function of only t_2. The solutions of Eqs. (2.37) and (2.38) are given by

$$x_2 = -\frac{\beta_{xx} - b\omega_x}{3\omega_x^2} A_x^2 \mathrm{e}^{2i\omega_x t_0} - \frac{\beta_{xx} + b\omega_x^2}{\omega_x^2} |A_x|^2 + cc, \tag{2.41}$$

$$y_2 = -\frac{\beta_{yy} - b\omega_x}{3\omega_x^2} A_y^2 \mathrm{e}^{2i\omega_x t_0} - \frac{\beta_{yy} + b\omega_x^2}{\omega_x^2} |A_y|^2 + cc. \tag{2.42}$$

Similarly, substituting Eqs. (2.35), (2.36), (2.41) and (2.42) into Eqs. (2.33) and (2.34) leads to solvability conditions so as to eliminate the secular terms in x_3 and y_3:

$$2i\omega_x D_2 A_x + i\omega_x \hat{c}_x A_x + i\omega_x \hat{\mu}_x \tau^* \omega_x^2 A_y - \omega_x K_x A_x |A_x|^2 - \omega_x^2 \hat{\mu}_x A_y - \frac{i\hat{e}_x}{2} \mathrm{e}^{i\hat{\sigma} t_2} = 0, \tag{2.43}$$

$$\begin{aligned} 2i\omega_x D_2 A_y + i\omega_x \hat{c}_y A_y + i\omega_x \hat{\mu}_y \tau^* \omega_x^2 A_x - \omega_x K_y A_y |A_y|^2 - \omega_x^2 \hat{\mu}_y A_x - \frac{i\hat{e}_y}{2} \mathrm{e}^{i\hat{\sigma} t_2} \\ + 2\omega_x \hat{\alpha} A_y = 0 \end{aligned} \tag{2.44}$$

where

$$K_x = -3\beta_{xxx} + \frac{10}{3}\omega_x^2 \left(\beta_{xx}^2 + b\omega_x^2 \beta_{xx}\right) + \omega_x^2 \left(\frac{4}{3}b^2 + b\right), \tag{2.45}$$

$$K_y = -3\beta_{yyy} + \frac{10}{3}\omega_x^2 \left(\beta_{yy}^2 + b\omega_x^2 \beta_{yy}\right) + \omega_x^2 \left(\frac{4}{3}b^2 + b\right). \tag{2.46}$$

To solve Eqs. (2.43) and (2.44) for A_x and A_y, we transform complex functions A_x and A_y into the polar form

$$\epsilon A_x(t_2) = \frac{1}{2} a_x(t_2) \mathrm{e}^{i[\phi_x(t_2) + \hat{\sigma} t_2]}, \tag{2.47}$$

$$\epsilon A_y(t_2) = \frac{1}{2} a_y(t_2) \mathrm{e}^{i[\phi_y(t_2) + \hat{\sigma} t_2]} \tag{2.48}$$

where a_x, a_y, ϕ_x and ϕ_y are real functions of t_2. Substituting Eqs. (2.47) and (2.48) into Eqs. (2.43) and (2.44), and separating the results into real and imaginary parts, a set of amplitude equations for the oscillation amplitude and the phase shift are obtained.

$$\frac{da_x}{dt^*} = -\frac{c_x}{2}a_x - \frac{\mu_x \tau^* \omega_x^2}{2}a_y + \frac{\omega_x \mu_x}{2}a_y \sin\left(\phi_y - \phi_x\right) + \frac{e_x}{2\omega_x}\cos\phi_x, \tag{2.49}$$

$$\frac{d\phi_x}{dt^*} = -\sigma - \frac{K_x}{8}a_x^2 - \frac{\omega_x \mu_x}{2}\frac{a_y}{a_x}\cos\left(\phi_y - \phi_x\right) - \frac{e_x}{2\omega_x a_x}\sin\phi_x, \tag{2.50}$$

$$\frac{da_y}{dt^*} = -\frac{c_y}{2}a_y - \frac{\mu_y \tau^* \omega_x^2}{2}a_x + \frac{\omega_x \mu_y}{2}a_x \sin\left(\phi_x - \phi_y\right) + \frac{e_y}{2\omega_x}\cos\phi_y, \tag{2.51}$$

$$\frac{d\phi_y}{dt^*} = -\sigma - \frac{K_y}{8}a_y^2 - \frac{\omega_x \mu_y}{2}\frac{a_x}{a_y}\cos\left(\phi_x - \phi_y\right) - \frac{e_y}{2\omega_x a_y}\sin\phi_y + \alpha a_y \tag{2.52}$$

where the scaled parameters by using ϵ are reset to the original form without $(\hat{\ })$. Substituting Eqs. (2.47) and (2.48) into Eqs. (2.35) and (2.36) yields the first approximate solution

$$\Delta x = a_x \cos\left(\omega_f t^* + \phi_x\right) + O(\epsilon^2), \tag{2.53}$$

$$\Delta y = a_y \cos\left(\omega_f t^* + \phi_y\right) + O(\epsilon^2). \tag{2.54}$$

2.2.3 Nonlinear normal modes

In analogy with the LNMs, we consider undamped free oscillation of Eqs. (2.49) to (2.52). Dropping the damping and driving terms, the amplitude equations for NNMs are given by

$$\frac{da_x}{dt^*} = \frac{1}{2}\omega_x \mu_x a_y \sin\left(\phi_y - \phi_x\right), \tag{2.55}$$

$$\frac{d\phi_x}{dt^*} = -\frac{K_x}{8}a_x^2 - \frac{1}{2}\omega_x \mu_x \frac{a_y}{a_x}\cos\left(\phi_y - \phi_x\right), \tag{2.56}$$

$$\frac{da_y}{dt^*} = \frac{1}{2}\omega_x \mu_y a_x \sin\left(\phi_x - \phi_y\right), \tag{2.57}$$

$$\frac{d\phi_y}{dt^*} = -\frac{K_y}{8}a_y^2 - \frac{1}{2}\omega_x \mu_y \frac{a_x}{a_y}\cos\left(\phi_x - \phi_y\right) + \alpha a_y. \tag{2.58}$$

In what follows, the steady-state solution of Eqs. (2.55) to (2.58) is considered by extending the definition of normal modes; motions which depart from a NNM confined in it for all time. To obtain explicit expression of the NNMs, letting $da_x/dt = da_y/dt =$

0 in Eqs. (2.55) and (2.57) yields

$$\phi_x - \phi_y = 0,\ \pi \tag{2.59}$$

which correspond to in-phase and out-of-phase NNMs, respectively. Since $d\left(\phi_x - \phi_y\right)/dt = 0$ from Eq. (2.59), Eqs. (2.56) and (2.58) lead to a following nonlinear algebraic relation for a_x and a_y.

$$-\frac{K_x}{8}a_x^2 + \frac{K_y}{8}a_y^2 \mp \frac{\omega_x}{2}\left(\frac{\mu_x a_y}{a_x} - \frac{\mu_y a_x}{a_y}\right) - \alpha a_y = 0. \tag{2.60}$$

The first approximate solution of the free oscillation is

$$\Delta x = a_x \cos\Omega_x(t^*) + O(\epsilon^2), \tag{2.61}$$

$$\Delta y = a_y \cos\Omega_y(t^*) + O(\epsilon^2) \tag{2.62}$$

where $\Omega_i(t^*) = \omega_x t^* + \phi_i$ is the oscillation phase of the normal modes. The normal frequency of Δx and Δy, denoted by ω_1 and ω_2 are given by

$$\omega_1 = \frac{d\Omega_x(t^*)}{dt} = \omega_x - \frac{K_x}{8}a_x^2 - \frac{\omega_x \mu_x a_y}{2a_x}\cos\left(\phi_y - \phi_x\right), \tag{2.63}$$

$$\omega_2 = \frac{d\Omega_y(t^*)}{dt} = \omega_x - \frac{K_y}{8}a_y^2 - \frac{\omega_x \mu_y a_x}{2a_y}\cos\left(\phi_x - \phi_y\right) + \alpha. \tag{2.64}$$

On the NNMs, the bubbles oscillate at the same frequency, ω, which are determined by Eqs. (2.63) and (2.64). In order to complete understanding a bifurcation structure of the normal modes, the case of equally-sized bubbles is considered in the following. In this case ($\alpha = 0$), one can analytically obtain the oscillation frequency and amplitude at the bifurcation point. Straightforward calculations using the symmetric property of the system and Eq. (2.60) lead to

$$\left(a_x^2 - a_y^2\right)\left[-\frac{K_x}{8} \pm \frac{\omega_x \mu_x}{2a_x a_y}\right] = 0 \tag{2.65}$$

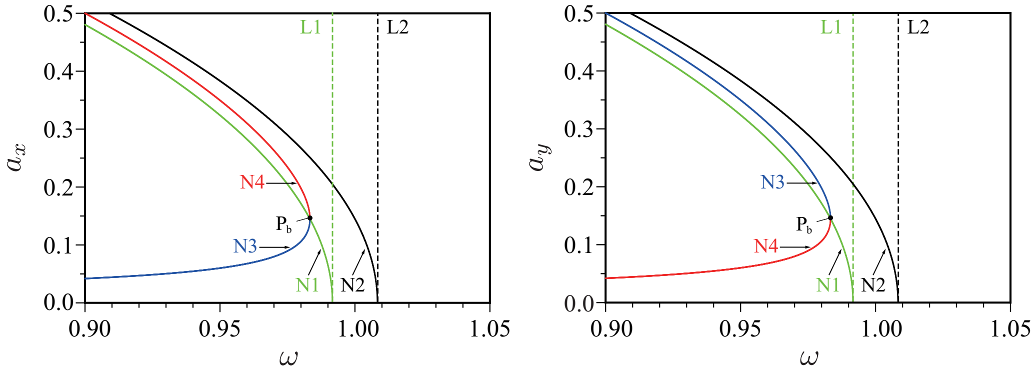

FIGURE 2.2: The NNMs Ni ($i = 1, 2, 3, 4$) as a function of normal oscillation frequency ω (Case A: $R_{10} = R_{20} = 10\ \mu$m). The LNMs, L1 and L2, are also shown for comparison.

where K_y and μ_y are replaced by K_x and μ_x owing to the equality of the bubble sizes. Assuming a_x and a_y to be positive quantities without loss of generality, Eq. (2.65) produces

$$a_y = \begin{cases} a_x, \dfrac{4\omega_x \mu_x}{K_x a_x} & (\phi_x - \phi_y = 0), \\ a_x & (\phi_x - \phi_y = \pi). \end{cases} \tag{2.66}$$

Therefore, we obtain four types of NNMs:

N1: $a_x = a_y,\ \phi_x - \phi_y = 0$

N2: $a_x = a_y,\ \phi_x - \phi_y = \pi$

N3: $a_x \geq a_y,\ \phi_x - \phi_y = 0$ (Localized mode)

N4: $a_x \leq a_y,\ \phi_x - \phi_y = 0$ (Localized mode)

where Ni (i =1,2,3 and 4) denotes a branch of the four types of NNMs. The non-localized normal modes N1 and N2 correspond to in-phase and out-of-phase motions. Localized modes N3 and N4 indicate a localized oscillation where the total vibration energy of the system is not evenly shared between the oscillators, but confined to either one. Fig. 2.2 illustrates the NNMs as a function of oscillation frequency where the LNMs, Li ($i = 1, 2$), are also depicted for comparison. The frequency of N1 and N2 decreases with increasing oscillation amplitude, and they converge asymptotically to their linear counterparts L1 and L2 in the limit of zero-amplitude. The in-phase mode, N1, splits up at the bifurcation point, $\mathrm{P_b}$, and the localized normal modes, N3 and N4, emerge on either sides of N1 as a result of a pitchfork bifurcation (i.e., symmetry-breaking). It follows that nonlinear localized resonance is expected in the neighborhood of the localized NNMs if the vibration amplitude exceeds a certain critical value. What is notable is that nonlinear localization can occur even in an equal-sized pair of bubbles which has no structural detuning but is completely symmetric. The amplitude and the frequency at the bifurcation point, $\mathrm{P_b}$, are given by

$$a_{\mathrm{bp}} = 2\left[\frac{\omega_x \mu_x}{K_x}\right]^{\frac{1}{2}}, \tag{2.67}$$

$$\omega_{\mathrm{bp}} = \omega_x(1-\mu_x). \tag{2.68}$$

The amplitude at $\mathrm{P_b}$ is proportional to the square root of the ratio between the magnitude of the nonlinearity and radiation coupling. In contrast, the frequency at $\mathrm{P_b}$ is just a linear function of the coupling coefficient. We note that these results are valid only for a limited parameter space under the small-amplitude approximation. Furthermore, the bifurcation structure and their stability highly depend on energy dissipation because the damping effect tends to smooth out the energy localization.

2.2.4 Steady state solution

The steady-state amplitude, the phase shift of Δx and Δy and their linear stabilities are shown in Fig. 2.3 as a function of the driving frequency. It is clear that the forced oscillation occurs in the neighborhood of the NNMs as is the case with linear resonance; The branches a1 and a2 (in-phase oscillation) result from the in-phase normal mode N1, and the branches a3 and a4 (localized oscillation) arise from the localized normal mode N3 and N4, respectively. Out-of-phase motion associated with N2 is not in resonance for this case. We found that the branch a1 is connected to a saddle-node

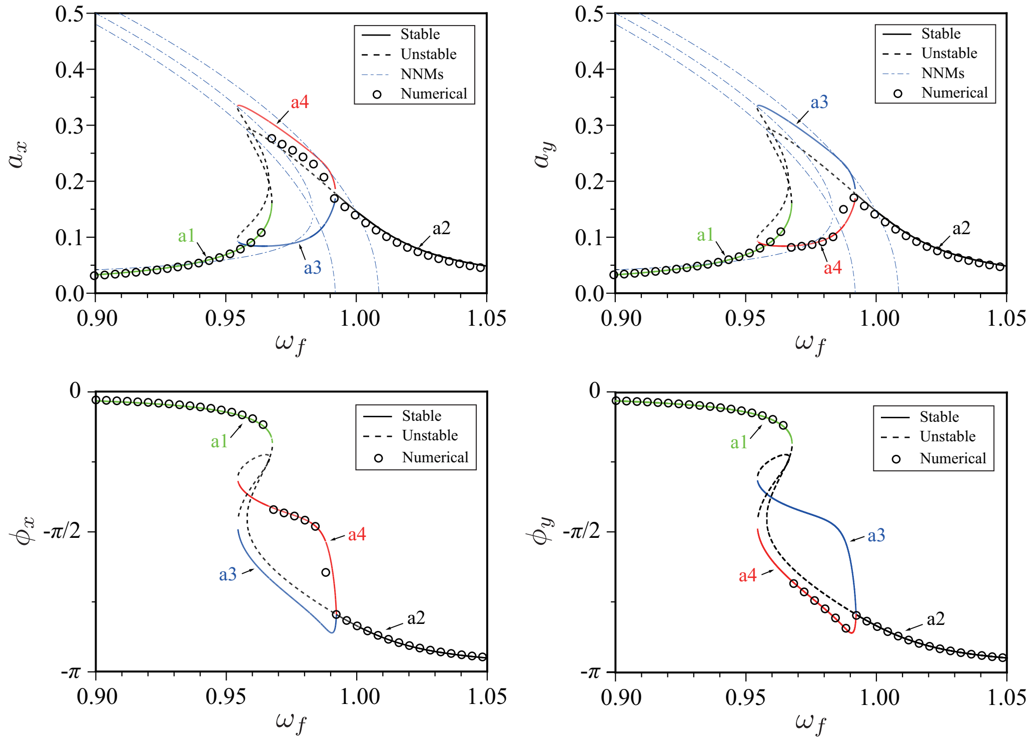

FIGURE 2.3: The steady-state amplitude (top) and the phase shift (bottom) of the fundamental component for case B as a function of the dimensionless driving frequency denoted by ai (i =1,2,3 and 4) in different colors. Solid and dashed lines stand for stable and unstable solutions, respectively. For convenience, the NNMs in Fig. 2.2 are also depicted. The numerical results (circles) are the steady-state fundamental component extracted from the FFT spectrum of time-radius curve.

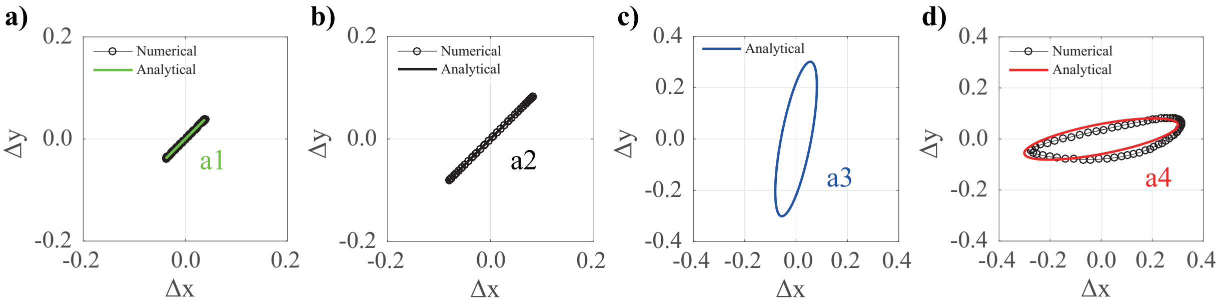

FIGURE 2.4: The steady-state solution of the branches a1 to a4 plotted in a Δx-Δy configuration space for (a) the branch a1 at $\omega_f = 0.92$, (b) the branch a2 at $\omega_f = 1.02$, (c) the branch a3 at $\omega_f = 0.97$ and (d) the branch a4 at $\omega_f = 0.97$. The physical parameters are the same as those of Fig. 2.3. Analytical solutions are the first approximation given by Eqs. (2.49) to (2.54). Numerical curves were obtain by time-integration of Eqs. (2.5) and (2.6).

bifurcation point at its right end, and a supercritical pitchfork bifurcation appears at the left end of a2. Consequently, there arises no stable synchronized motion between the

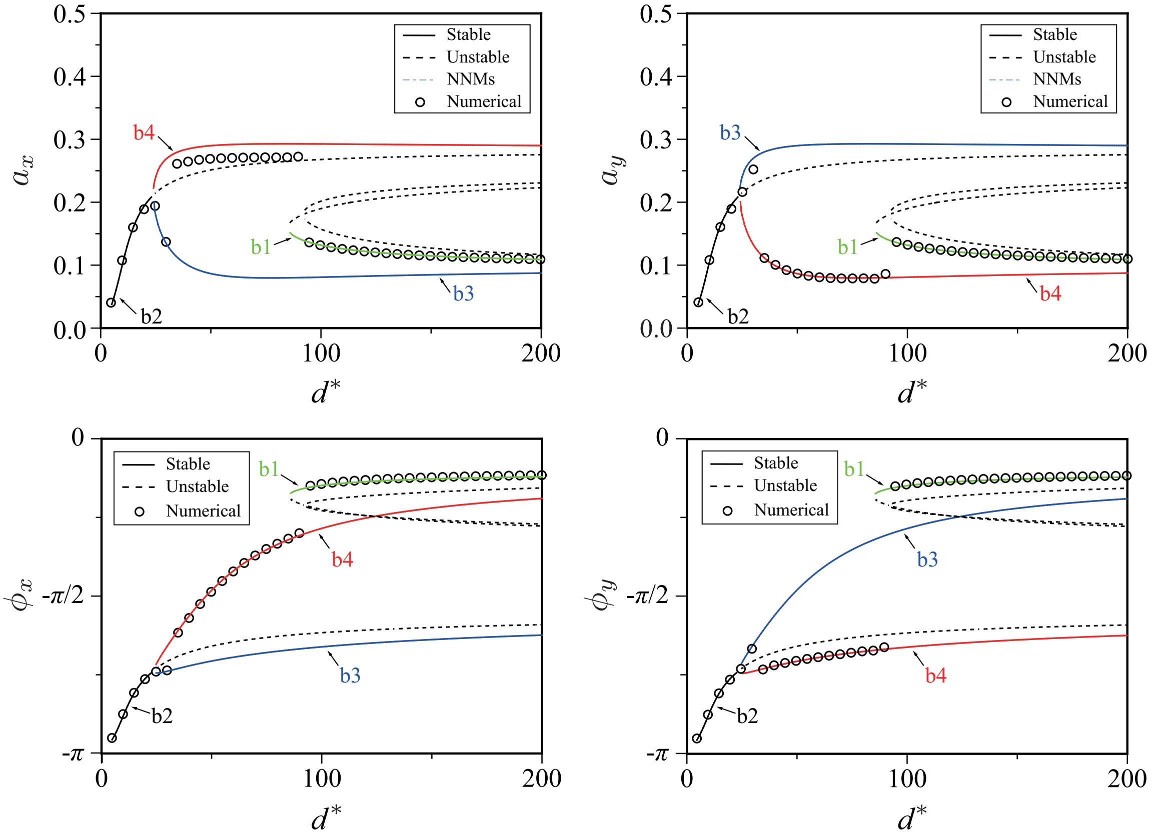

FIGURE 2.5: The steady-state amplitude (top) and the phase shift (bottom) of the fundamental component for case C as a function of the dimensionless separation distance denoted by bi (i =1,2,3 and 4) in different colors. Solid and dashed lines stand for stable and unstable solutions, respectively. The numerical results (circles) are the steady-state fundamental component extracted from the FFT spectrum of time-radius curve.

two bifurcation points. Instead, the localized solutions, a3 and a4, branch out from the pitchfork bifurcation point. We also notice that the localized branch a4 intersects with the non-localized branch a1, and three stable solutions coexist within a narrow range of the driving frequency. Comparison with the numerical results shows a good agreement over the range of the parameter limit. In general, more complicated bifurcation patterns are to be expected in other two-oscillator with different nonlinearities and topologically equivalent nonlinear systems. For reference, a bifurcation diagram for the case of larger bubbles of $100\ \mu\mathrm{m}$ in radius are presented in Appendix A.3. Since the larger bubbles have lower damping constants due to higher bubble wall Reynolds number, Hopf bifurcation and accompanying quasi-steady oscillation are found in Fig. A.1 in addition to

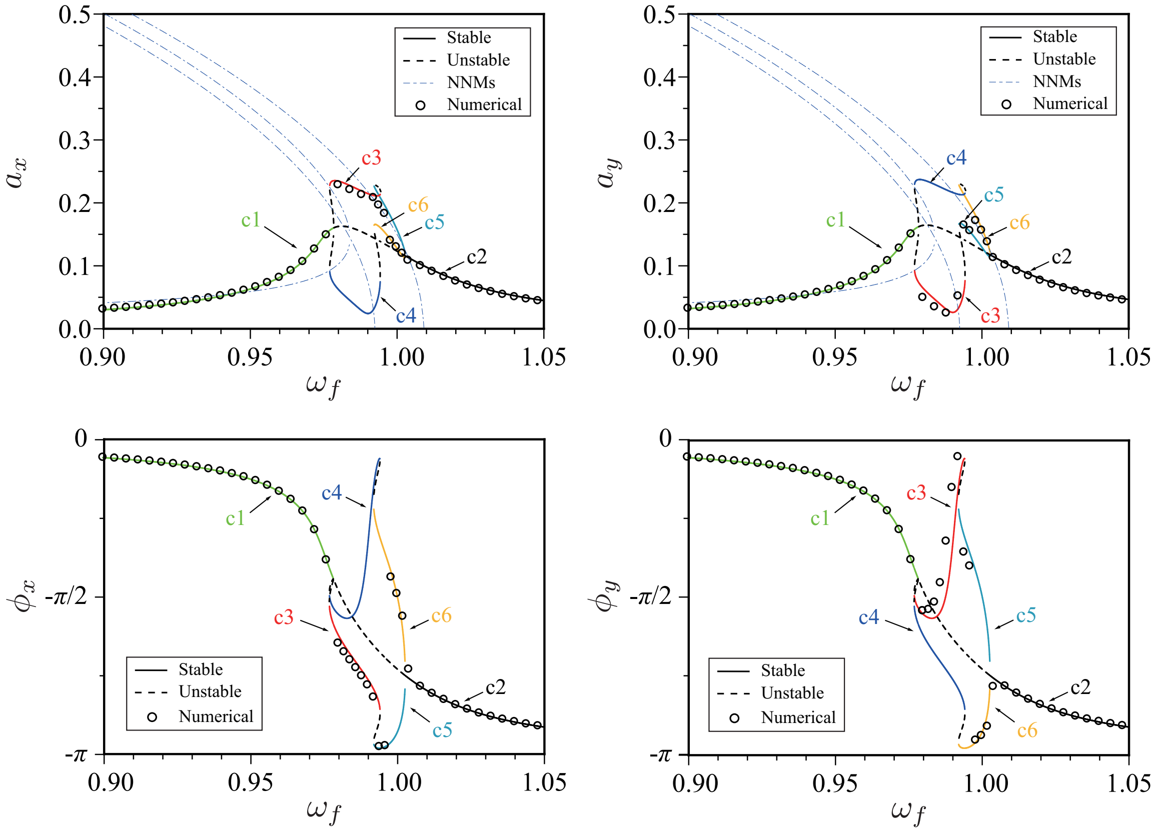

FIGURE 2.6: The steady-state amplitude (top) and the phase shift (bottom) of the fundamental component denoted by ci (i =1,2,3,4,5 and 6) in different colors. The parameters are same as case B in Table 1. For comparison to Fig. 2.3, the effect of finite speed of sound is incorporated only in the retardation effect, while neglecting the radiation damping. The numerical results are obtained form Eqs. (2.15) and (2.16). The parameter of the retardation time is $\tau^* = 0.86$. Note that the peak amplitudes of c3 and c4 are substantially damped compared to Fig. 2.3, and out-of-phase motions (c5 and c6) manifest in the neighborhood of N2.

the symmetry-breaking bifurcation.

In Fig. 2.4, these four types of steady-state solutions are described in $\Delta x - \Delta y$ configuration space. The non-localized solutions, a1 and a2, look like a straight line with a positive slope of unity in Fig. 2.4(a) and (b) because of the completely synchronized in-phase motion, while the plot of localized solutions, a3 and a4, are an elongated closed orbit with an oblique axis. The orientation of the axes are due to the localization of the phase difference shown in Fig. 2.3.

The steady-state amplitude and the phase shift as a function of the separation distance $d^*(= d/R_{10})$ are shown in Fig. 2.5 where the driving frequency is fixed to $\omega_f =$

0.97. The branch bi, respectively, corresponds to the branches ai in Fig. 2.3 for the same i =1,2,3 and 4. The similar bifurcation structures (i.e., pitchfork and saddle-node bifurcations) are also the case as with Fig. 2.3. That is, multi-valued stable solutions arise by increasing the separation distance, leading to a drastic jump of the steady-state at $d^* = 90$ where the phase difference $\phi_y - \phi_x$ changes from $\pi/2$ to zero. This indicates that even a small coupling effect exerted from neighboring bubbles are essentially negligible in such nonlinear regime. The immediate question is to which solution does the system converge for a typical initial condition. It requires observation of the sensitive dependence of the long-time behavior on the initial conditions and is beyond the scope of this paper.

Fig. 2.6 presents the effect of non-zero retardation time on the steady-state solution. The parameters are the same as Fig. 2.3 (case B) except for the presence of the retardation effect. The primary difference from Fig. 2.3 (no time delay) is that one pair of additional localized steady-state solutions, c5 and c6, arise in the neighborhood of N2 (out-of-phase mode) as a result of symmetry-breaking bifurcation of c2. Indeed, out-of-phase oscillations of c5 and c6 are evident from the bifurcation diagram of the phase shift in Fig. 2.6. We also note that the peak amplitude of c3 and c4 are damped compared to Fig. 2.3. These differences are due to the additional damping term, i.e., non-diagonal elements of the damping matrix C in Eq. (2.16). In fact, the NNMs are unchanged with the presence of the retarded time as seen in Eq. (2.66). The result is consistent with the discussion of (Doinikov, Manasseh, and Ooi, 2005) for two-bubble oscillation; the damping constant of the higher-frequency mode, corresponding to L2 of this study, decreases because of the presence of the retarded effect, while that of the lower-frequency mode is substantially increased.

TABLE 2.1: Dimensionless parameters for air bubbles in water and the atmospheric ambient pressure. The equilibrium radii of the two bubbles are 10 μm for all the cases. Case A corresponds to an undamped free oscillation (damping and driving pressure are removed), and the other cases are for forced oscillation with damping effects. Note that in case D and E Reynolds number is calculated with the effective kinematic viscosity $\nu_{\text{eff}} = 6.73 \times 10^{-3}$ m^2/s, and the effective polytropic exponent $\kappa_{\text{eff}} = 1.10$. The corresponding driving pressure are 2.5 and 100 kPa for $A^* = 2.50 \times 10^{-2}$ and 1.00, respectively.

Case	R^*	Eu	Re	We	C	Pe	A^*	ω_f	d^*
A	1	0.214	215	64.3	∞	∞	$\cdots$	$\cdots$	60
B	1	0.214	215	64.3	∞	∞	0.0250	0.9-1.05	60
C	1	0.214	215	64.3	∞	∞	0.0250	0.97	5-200
D	1	0.214	215	64.3	69.5	11.4	1.00	0.3-1.1	7.5
E	1	0.214	215	64.3	69.5	11.4	1.00	0.3-1.1	3-45
F	1	0.235	2.06×10^3	585	∞	∞	0.0150	0.9-1.05	60

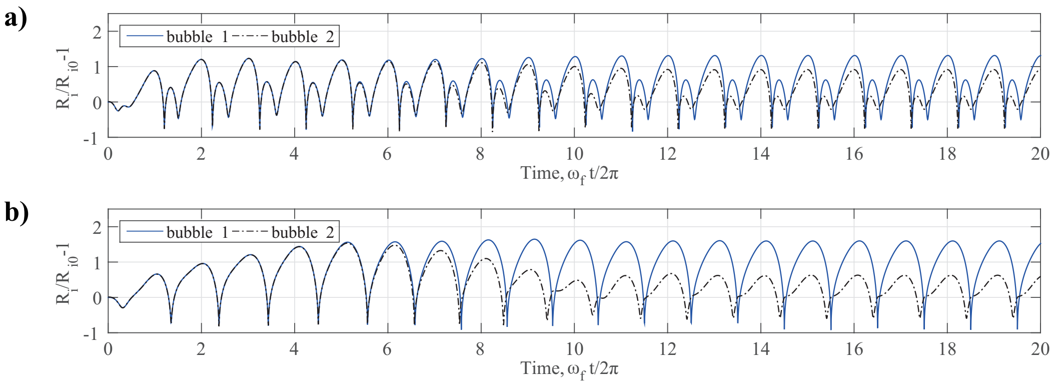

FIGURE 2.7: Time-radius curves for (a) $\omega_f = 0.40$ (second superharmonic resonance), (b) $\omega_f = 0.70$ (primary resonance). The physical parameters are case D ($d^* = 7.5$, and $A = 1.00$) in Table 2.1.

2.3 Numerical results

The preceding weakly nonlinear analysis assumed small-amplitude perturbation and is valid only for the limited parameter space. In this section, large amplitude oscillations for a wide range of the driving frequency and the separation distance are presented. An pair of equally-sized bubbles of 10 μm in radius with a fixed separation distance are driven by a sound pressure amplitude of 100 kPa. We put a small disturbance to the initial radius of bubble 2 in order to avoid a completely symmetric motion, and $(R_1(0), R_2(0), \dot{R}_1(0), \dot{R}_2(0)) = (1, 1.01, 0, 0)$ is used for each ω_f. To be simple, the

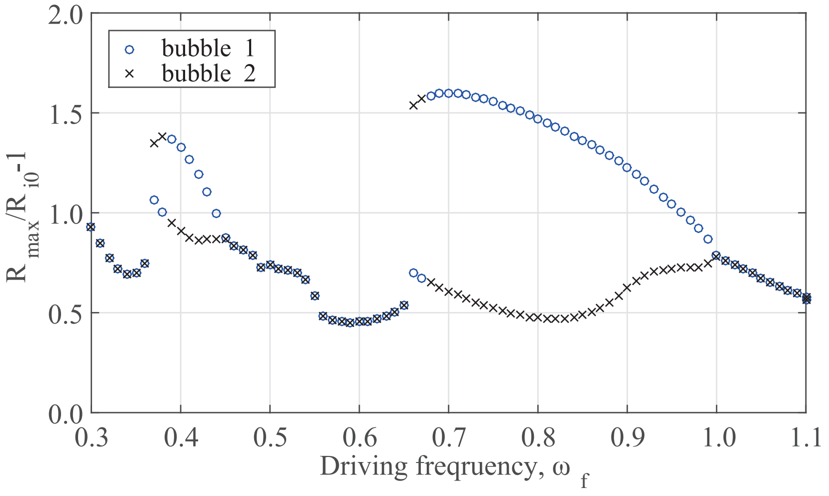

FIGURE 2.8: Frequency response curves of the maximum bubble radii obtained from the steady-state oscillation after 32 cycles of the driving period. The physical parameters are case D ($d^* = 7.5$, and $A = 1.00$) in Table 2.1. The sound pressure corresponds to 100 kPa.

retarded effect is neglected in the following numerical calculation. In addition, we account for the well-known additional damping (Devin Jr, 1959; Chapman and Plesset, 1971) because the thermal damping dominates over the viscous damping for a resonant bubble in a wide range of equilibrium bubble sizes. The effective viscosity, ν_{eff}, and polytropic index, κ_{eff}, for thermal behavior of the internal gas are given by a function of Péclet number, $\text{Pe} = \omega_f R_{10}^2/\alpha_{\text{th}}$, where α_{th} is the thermal diffusivity of the gas (Prosperetti, Crum, and Commander, 1988). In the calculation, the governing equation is transformed into a C^∞ equivalent dynamical system (Parlitz, Englisch, Scheffczyk, and Lauterborn, 1990) to achieve smoother oscillation in the transformed system since a singular behavior due to a violent collapse of a bubble oscillation leads to serious numerical errors. The classical fourth order Runge–Kutta method is used for time integration.

In Fig. 2.7, time-radius curves of typical localized oscillation are plotted for case D with a fixed driving frequency. The oscillation amplitudes are attracted to a localized steady-state after the transient response decays although both motions of the bubbles look identical during the first eight oscillation periods. It is also interesting to note that the phase shifts of the oscillators converge to different values, and the bubbles collapse

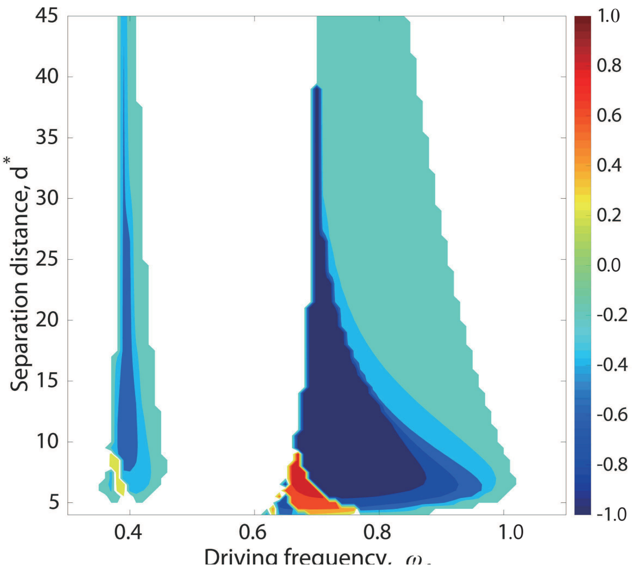

FIGURE 2.9: Contour plot of $\Delta R_{\max} = (R_{2\max} - R_{1\max})/R_{10}$ as a function of the driving frequency and the separation distance. Note that $\Delta R_{\max} = 0$ indicates non-localized oscillation which is not plotted, and only localized oscillation $\Delta R_{\max} \neq 0$ is plotted. The physical parameters used are those for case E ($d^* = 3 - 45$, and $A^* = 1.00$) in Table 2.1.

with a slight time lag. Fig. 2.8 shows the frequency response curve of the maximum bubble radii, $R_{i\max}$, obtained from the steady-state oscillation after 32 cycles of the driving period (Case D). The localized oscillations of the primary resonance demonstrated in the previous section are clearly observed. The in-phase localized oscillation as shown in Fig. 2.7(b) arises for a wide range of the driving frequency as can be expected from the discussion of N3 and N4, while out-of phase motions associated with mode N2 are suppressed by the presence of the additional thermal damping. As a result, the bifurcation structure is similar to Fig. 2.3. In addition, symmetry-breaking bifurcation of superharmonic resonance is evident at $\omega_f \approx 0.40$, while the perturbation analysis of this frequency range is not presented in this article. The symmetry-breaking bifurcation at the superharmonic resonance was numerically observed in coupled two Duffing oscillators (Kozłowski, Parlitz, and Lauterborn, 1995). Furthermore, the magnitudes of $R_{1\max}$ and $R_{2\max}$ are switched at the resonance peaks. It follows that the magnitude of localized oscillation is sensitive, at the vicinity of resonance peaks, to microscopic fluctuation of initial conditions or an external disturbance with the magnitude of no more than 1 % of the initial bubble radii.

In order to explore bifurcation structures in $\omega_f - d^*$ space, contour plot of the difference of the maximum amplitude, $\Delta R_{\max} = (R_{2\max} - R_{1\max})/R_{10}$, as a function of the driving frequency and the separation distance is illustrated in Fig. 2.9 where the physical parameters of case E are used. In contrast to the weakly nonlinear case, localization occurs at short separation distances. This is because both the nonlinearity and coupling strength should be large enough to counterbalance the thermal damping. Therefore, the region of localization shifts toward a low-frequency and short-distance part of the $\omega_f - d^*$ space which is a fairly typical parameter range used in practical experiments and simulations in the early literatures (Takahira, Akamatsu, and Fujikawa, 1994; Parlitz, Englisch, Scheffczyk, and Lauterborn, 1990; Takahira, Yamane, and Akamatsu, 1995; Ooi and Manasseh, 2005; Mettin, Akhatov, Parlitz, Ohl, and Lauterborn, 1997; Wiedemair, Tukovic, Jasak, Poulikakos, and Kurtcuoglu, 2014). It follows that even a single-sized bubble cloud can have complex bifurcation structures depending on the concentration of bubbles and the driving pressure amplitude at the nonlinear resonant frequencies.

2.4 Summary

This chapter provides an asymptotic derivation of the steady-state solution and underlying NNMs for the primary resonance of two spherical bubbles oscillating with a fixed separation distance. In the case of equal-sized bubbles, an approximate solution of the oscillation amplitude and the phase shift shows symmetry-breaking bifurcations, leading to multi-valued stable solutions in the neighborhood of the localized NNMs. The distinctive feature of these solutions is that localized oscillation can occur depending on the driving frequency and the separation distance between the bubbles; the synchronized steady-state motion becomes unstable in a certain range of the parameter space. In addition to the symmetry-breaking bifurcation, Hopf bifurcations turn out to occur for the case of lower damping constants (i.e., for larger bubbles). Additionally, numerical calculation shows that the localized oscillation occur for a fairly typical parameter range used in practical experiments and simulations in the literature.

Chapter 3

Translational dynamics of an oscillating bubble cluster

Translational motion of an oscillating bubble cluster under sound irradiation is studied experimentally and is modeled in the framework of the classical approach of Bjerknes. An experimental technique is proposed to observe bubble cluster formation and its translational dynamics interacting with wall boundaries due to the secondary Bjerknes force. The translational motion observed in the experiment is modeled by extending the classical theory of Bjerknes on single bubble; a bubble cluster is treated as a single bubble. The extended Bjerknes theory is shown to allow us to predict the overall trajectory of the cluster translating toward a wall of finite acoustic impedance by tuning acoustic energy loss at the wall. The drag force turns out to be unimportant for the translation of a millimeter-sized cluster that we observed.

3.1 Experimental method

3.1.1 Experimental setup

The experimental setup is sketched in Fig. 3.1(a). A rectangular acrylic vessel (inside sizes: 50 mm × 50 mm × 100 mm, thickness: 5 mm) filled with tap water of 90 mm in height at the room temperature was fixed on a vibration generator (513-BS/Z08, EMIC

Corp.). A vacuum pump (DAP-6D, ULVAC KIKO Inc.) was connected to the well-closed vessel through a valve in order to reduce the hydrostatic pressure in the vessel toward the vapor pressure. With the reduced ambient pressure, one can easily obtain cavitation evens at low driving amplitude of the vibration generator (Crum, 1975). Continuous sinusoidal excitation was input from a function generator (WF1973, NF Corp.) via a power amplifier (371-A, EMIC Corp.). The acceleration of the vessel in the vertical direction was measured by an accelerometer (710-D, EMIC Corp.) with a charge amplifier (6001-AHD/1NBD-1, EMIC Corp.), which was used to calculate the absolute liquid pressure. The gas pressure in the container was monitored by a pressure sensor (HAV-100KP-V, SENSEZ) attached on the top of the vessel. The absolute gas pressure remains approximately at 5.0 kPa under steady state operation of the vacuum pump. It turned out that the gas pressure is almost undisturbed, even with the presence of cavitation. It can therefore be assumed that the liquid pressure at the free surface is fixed at the gas pressure.

The recording system consists of a high-speed video camera (FASTCAM SA-5, Photron), a distortion-less macro lens (VS-LD50, VS Technology) combined with a 2.0× magnification converter lens (VS-2.0XV, VS Technology), and LED backlight (TS-LAX-RGB3, MeCan imaging). The spatial resolution of images was 41 μm per pixel. The recording frame rate of the high-speed camera was set at 10000 frame/s, which is sufficiently fast for image processing with the Fourier analysis. The exposure time of the camera was fixed to 0.1 ms.

3.1.2 Preparation of a bubble cluster

A millimeter-sized gas bubble as a cavitation nucleus was manually injected by a needle through a silicone plug of 4.5 mm in diameter, which was located at 30 mm above the vessel bottom and 25 mm away from the side walls. The bubble injection was sketched in Fig. 3.1(b). The diameter of the gas nucleus we obtained is approximately 1 mm. The side view of the bubble nucleus is shown in Fig. 3.2. The bubble remained attached to

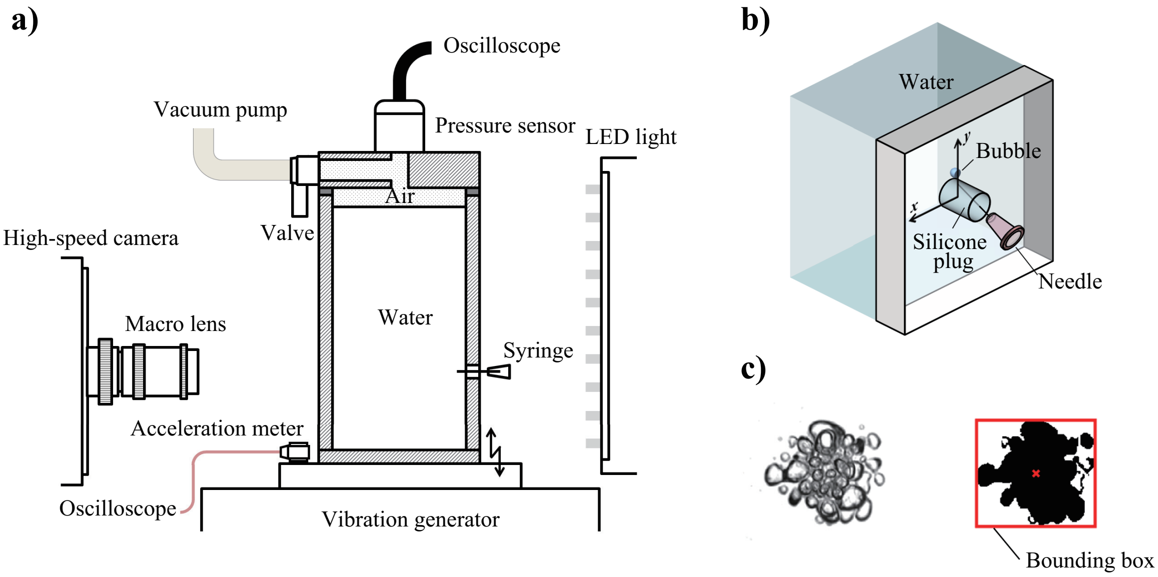
a)
Oscilloscope
Vacuum pump
Pressure sensor
LED light
Air
Valve
High-speed camera
Water
Macro lens
Syringe
Acceleration meter
Oscilloscope
Vibration generator
b)
Water
Bubble
y
x
Silicone plug
Needle
c)
Bounding box

FIGURE 3.1: Schematic of (a) experimental setup, (b) an enlarged view of the silicone plug and needle and (c) comparison of a typical photographed image (left) and the image processing with a bounding box and its centroid (right).

the wall surface unless the external driving force was imposed.

The periodic pressure field induced by the driving acceleration will follow a potential solution owing to the sufficiently long wave length and given in the form of (Crum, 1975; Nyborg and Rodgers, 1967; Sorokin, Blekhman, and Vasilkov, 2012)

$$p(h,t) = p_0 + \rho_L g H + \rho_L A\omega^2 H \sin \omega t \tag{3.1}$$

where H is the water depth measured from the free surface, p_0 is the static pressure at the free surface, ρ_L is the liquid density, g is the gravitational acceleration, A is the displacement amplitude of the vibration generator, and ω is the angular frequency of the vibration generator. Since p_0 reached 5.0 kPa after vacuuming, the hydrostatic pressure at the initial bubble position, at $H = 60$ mm ($\equiv H_0$), was reduced to 5.6 kPa. As a result of this pressure reduction, the injected bubble nucleus was subject to large amplitude oscillation and accompanying surface instability in the sub-kHz sound field even with a weak sound amplitude $\rho_L A\omega^2 H$; this eventually leads to the formation of a collapsing

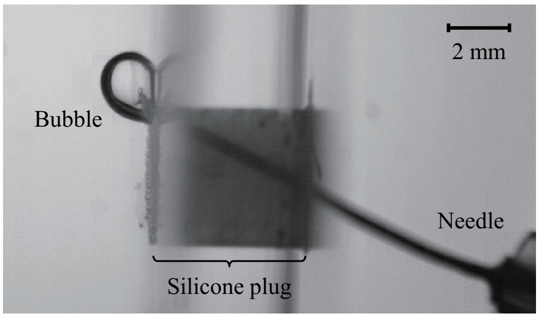

FIGURE 3.2: Sideview of an injected bubble nucleus corresponding to the schematic in Fig. 3.1(b).

bubble cluster. In fact, the displacement acceleration measured by the accelerometer was 29 $\mathrm{m/s^2}$ for 625 Hz and yields sound amplitude of 1.9 kPa at $H = H_0$. However, further large driving amplitude gave rise to a large number of cavitation arising probably from pre-existing bubble nuclei at the container surface (Atchley and Prosperetti, 1989). In order to observe only the motion of the injected bubble nucleus, the driving amplitude was set at sufficiently low levels to avoid such undesired cavitation events.

3.1.3 Image processing

The recorded images were analyzed using the image processing software (MATLAB, The Mathworks Inc.) function *graythresh* based on the binarization and thresholding technique of a recorded image sequence to 8-bit grayscale images. Fig. 3.1(c) shows comparison between a captured image and a processed binary image with a bounding-box which encloses the contour of the cluster with the minimum area. The area of the bounding-box A_{box} and the coordinate of its centroid (X, Y) were computed for each recorded image. Here, we defined an area-equivalent mean radius R_{b} as

$$R_{\mathrm{b}} = \sqrt{\frac{\text{Area of the inscribed ellipse}}{\pi}} = \frac{\sqrt{A_{\mathrm{box}}}}{2}. \tag{3.2}$$

Temporal evolution of R_{b} was produced from the recorded image sequence, and Fourier spectrum of the time-radius curve was then calculated for the use of theoretical analysis. The transient velocity U in the x direction was calculated by a simple central difference

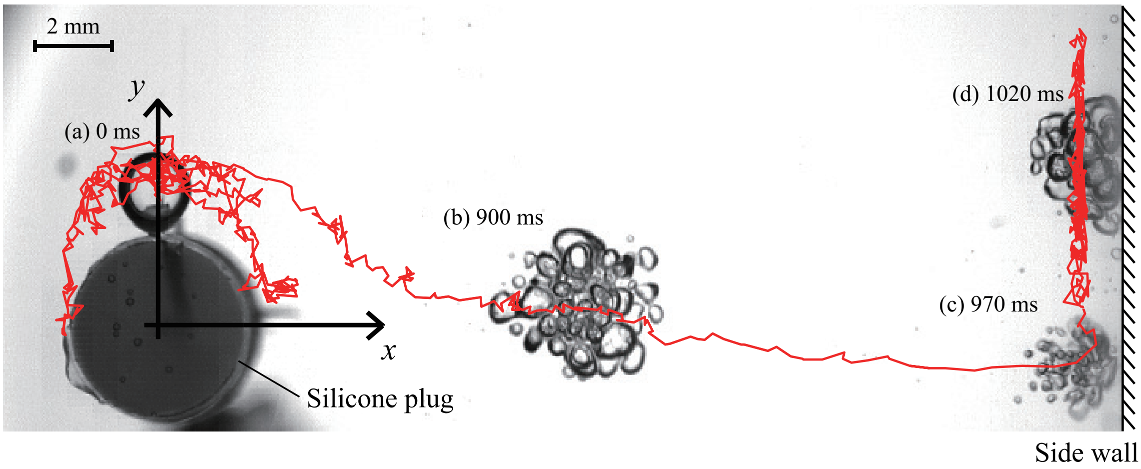

FIGURE 3.3: Trajectory of a cluster motion denoted by a red solid line. Representative pictures of the cluster are superimposed: (a) initial state, (b) collapse and fission, (c) jet formation and (d) oscillation in contact with the side wall. The injected bubble nucleus departs from the silicone plug and moves toward the right side wall.

of the X–t curve where X stands for the geometric center of a bubble cluster. Before applying differentiation to compute the velocity, the X–t curve was smoothed using a moving average low-pass filtering based on the MATLAB function *filter*.

3.2 Experimental observation

3.2.1 Overview of bubble cluster dynamics

Fig. 3.3 presents a representative example of cluster motion and its trajectory with the driving frequency 625 Hz. An initially injected bubble of R_b=1 mm departs from the silicone plug, oscillating in volume subject to the primary sound field. The bubble continuously collapses with the Rayleigh–Taylor-like surface instability and subsequent bubble fission (Brennen, 2002), so that the bubble oscillates as a cluster of bubble fragments. It should be noted that the cluster motion occurs almost in the horizontal direction because the primary Bjerknes force counterbalances to the buoyant force in the vertical direction.

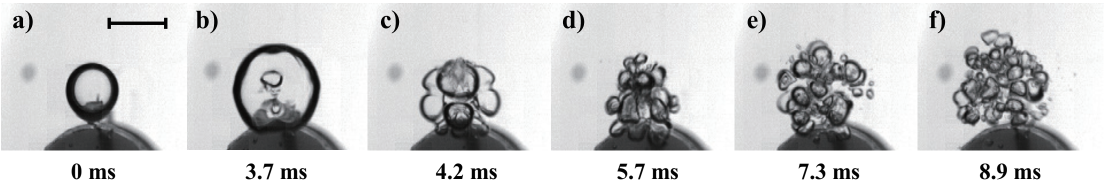

FIGURE 3.4: Snapshots of (a) the initial state, (b) maximum expansion, and (c-f) the consecutive collapse phases. The scale bar represents 2 mm.

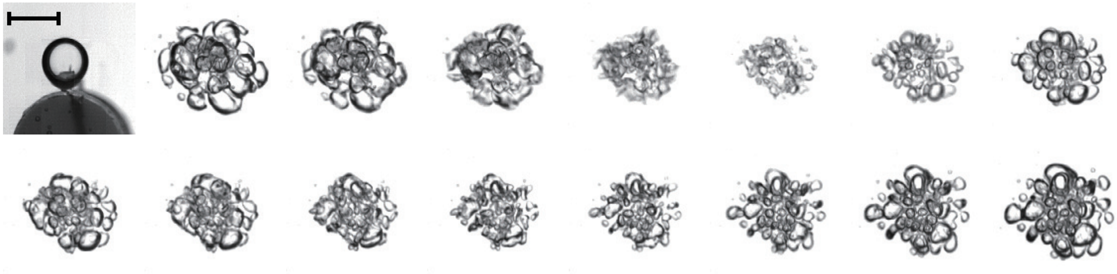

FIGURE 3.5: A typical image sequence of an oscillating bubble cluster driven at 625 Hz. The image sequence corresponds to one oscillation cycle of the imposed driving frequency. The scale bar represents 2 mm.

After some back-and-forth motion around the silicone plug, the bubble cluster goes straight to the right direction with increasing its translational velocity due to the secondary Bjerknes force that arises from the interaction with the side walls, as will be explained in Chapter 4. During the travel to the right side wall, the bubble cluster experienced kinds of phenomena shown in the following section, i.e., surface instability, bubble collapse and fission, coalescence, nonlinear oscillation, interaction with the wall boundaries.

3.2.2 Bubble collapse, fission and cluster oscillation

An image sequence of consecutive collapse phases is shown in Fig. 3.4. The dark circular structure seen beneath the bubble in the images is the upper part of the silicone plug. The initially spherical bubble reached a maximum radius $R_\mathrm{b} = 2.15$ mm, as seen in Fig. 3.4(b), after several driving periods. At the subsequent first collapse shown in Fig.

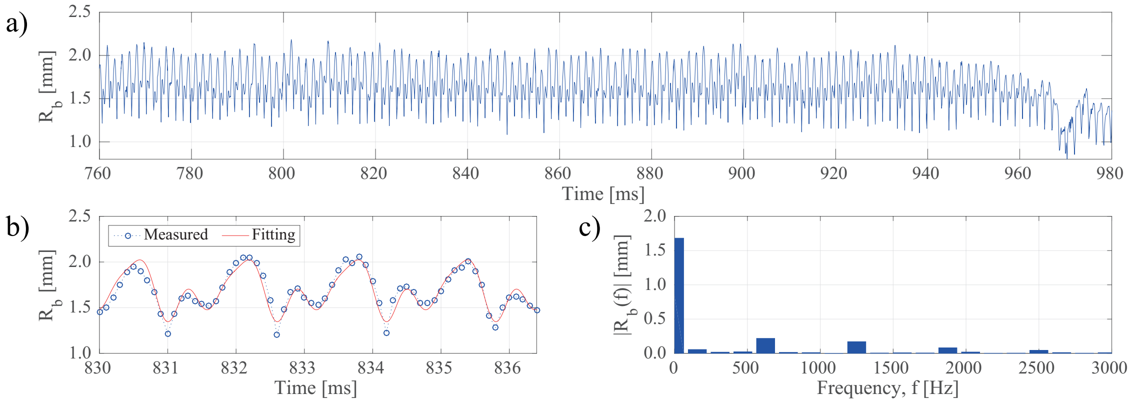

FIGURE 3.6: The results of image processing. (a) R_b–t curve, (b) R_b–t curve (enlarged) and (c) its Fourier spectrum. The fitting curve in (b) was reproduced using the frequency component up to the third harmonics of (c).

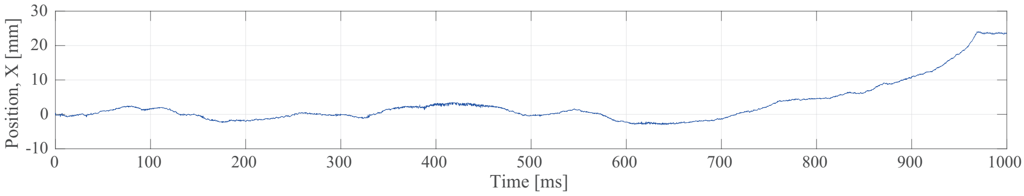

FIGURE 3.7: The temporal evolution of the cluster position.

3.4(c), surface instability was developed, so that the bubble was split into fission fragments. The deformed bubble has lost the spherical symmetry, but the configuration of the fragments has an almost exact line symmetry with respect to the vertical axis. This indicates that the primary sound field does not have a significant pressure gradient in the x direction as described by Eq. (3.1). After the second collapse shown in Fig. 3.4(d), each tuft-like structure in Fig. 3.4(c) seems to be split again into a couple of daughter bubbles. Although the number of fission fragments was augmented and the size of bubble fragments was ununiformly distributed, the line symmetry was barely retained at this moment. During the third collapse, the fragmentation continued further as shown in Fig. 3.4(e), and much smaller bubbles were produced. As seen in Fig. 3.4(f), the bubble fragments tended to be single-sized after the fourth collapse, and their oscillation phases were synchronized. At the subsequent collapses, the cluster looked very similar in a sense that the size and number of the bubble fragments remain at the same order, implying that fission and coalescence balance. The subsequent cluster oscillation for one driving period is shown in Fig. 3.5. The bubble cluster kept in contact with the back wall and slid across the contact surface with its shape remained nearly hemispherical.

Fig. 3.6(a) shows the last 130 oscillation periods of the evolution of the cluster radius R_b before the bubble cluster crashed to the right side wall. The beginning of the external driving is set to $t = 0$. The volumetric response of the bubble cluster is found to be almost in a steady state during the observation. It should be noted that the interaction between the cluster and the right side wall comes into play just before the cluster reaches the wall; otherwise, the interaction does not play an important role in the volumetric oscillation. The bubble fragments remain gathered in a cluster. This is because attractive secondary Bjerknes forces, which act on synchronously oscillating bubbles of the similar size, hold the bubble fragments closely together within the cluster.

The evolution of the cluster radius in shorter time is shown in Fig. 3.6(b) and its Fourier spectrum (from 64 data points) is computed in Fig. 3.6(c). The fitting curve is reproduced using Eq. (3.5), to be presented in the following section, where nonlinear components up to the third harmonic δ_3 are considered. It is clearly seen that there arises nonlinear resonance in the oscillation; the second superharmonic at 1250 Hz (i.e., twice the driving frequency) is notably evident. It follows that the resonant frequency of the cluster oscillation would lie around 1250 Hz. If the damping effect is small, resonant

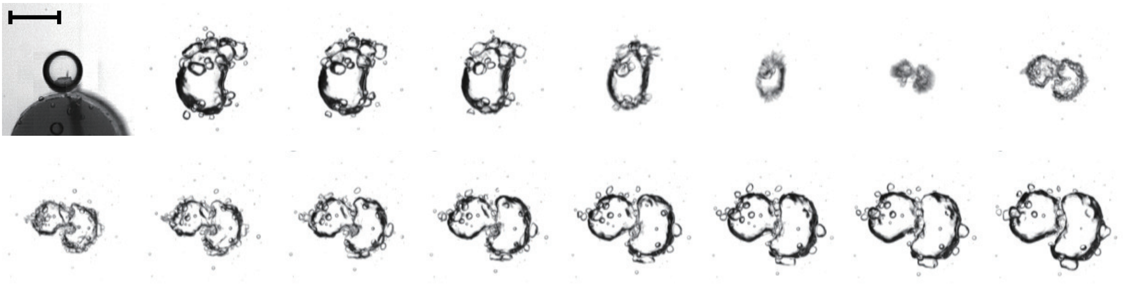

FIGURE 3.8: A typical image sequence of an oscillating bubble cluster driven at 312 Hz. The image sequence corresponds to one oscillation cycle of the imposed driving frequency. The scale bar represents 2 mm.

frequency of a spherical gas bubble is given by the Minnaert frequency, ω_M (Leighton, 2012). The formula of the natural frequency can be extended to the case of a spherical bubble cluster that consists of single-sized bubbles (Nigmatulin, Akhatov, Vakhitova, and Nasibullayeva, 2000; Nasibullaeva and Akhatov, 2013) and is given by

$$\omega_c = \frac{1}{a_0}\sqrt{\frac{3\gamma\left(p_0 - p_v\right) + \dfrac{2S}{a_0}(3\gamma - 1)}{\rho_L\left(1 + \dfrac{N^{1/3}a_0}{R_0}\left(N^{2/3} - 1\right)\right)}} < \omega_M \tag{3.3}$$

where N is the number of bubble fragments in the cluster, R_0 is the equilibrium cluster radius, a_0 is the equilibrium radius of bubbles in the cluster, γ is the ratio of the specific heats of the bubble contents, p_v is the vapor pressure and S is the surface tension. Eq. (3.3) is reduced to the Minnaert frequency when $N = 1$ and the surface tension is neglected. Calculating with $\gamma = 1.4$ (for air), $S = 0.073\,\mathrm{N/m}$, $R_0 = 1.6\,\mathrm{mm}$ and $p_0 - p_v \sim 3\,\mathrm{kPa}$ offers a reasonable estimation of a_0, given the cluster's resonance frequency $\omega_c = 2\pi \times 1250\,\mathrm{rad/s}$; $a_0 = 0.58\,\mathrm{mm},\ 0.35\,\mathrm{mm},\ 0.17\,\mathrm{mm}$ and $0.081\,\mathrm{mm}$, respectively, for $N = 1,\ 10,\ 100$ and 1000. In the particular example of our experiment in Fig. 3.3, the cluster dynamics are tuned to be under resonance at twice the driving frequency. Indeed, we also observed cluster oscillation under primary resonance (i.e., resonance at an imposed frequency) by lowering the driving sound frequency to 312.5 Hz (See Fig. 3.8), which consists of a small number of N but arising from similar R_0, leading to larger bubble fragments than that of Fig. 3.4. The result is consistent with the above discussion where one obtains a smaller resonant frequency from Eq. (3.3) for the case of larger a_0.

3.2.3 Interaction with wall boundaries

The trajectory of the cluster center is shown in Fig. 3.7. The cluster stayed around the plug until $t = 760\,\mathrm{ms}$. After that, the cluster began traveling toward the right side wall subjected to the secondary Bjerknes force exerted from the wall. The direction of movement depends not only on the initial position, but also the detuning of the vibrating

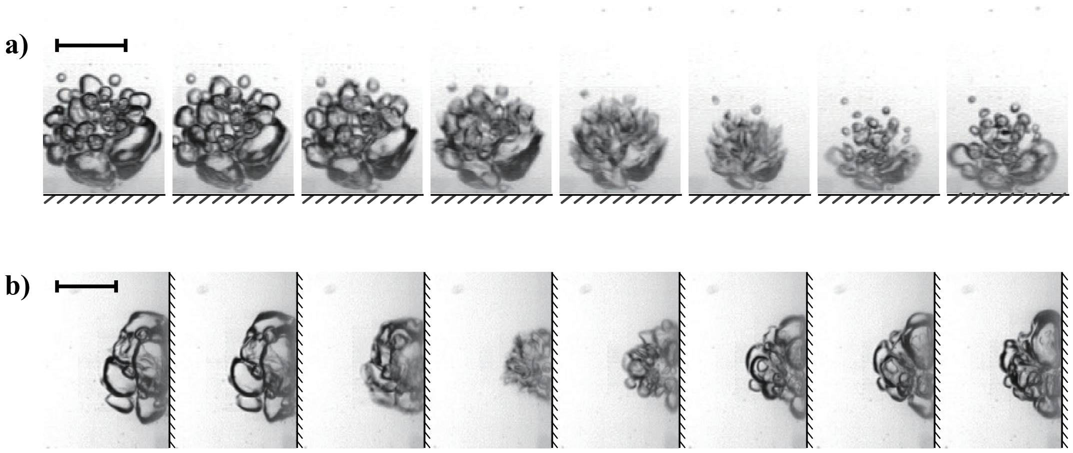

FIGURE 3.9: An image sequence of (a) the jet-like motion and (b) hemispherical oscillation in contact with the right side wall driven at 625 Hz. The scale bar represents 2 mm.

system and randomness of the fission process. The impact on the right wall (located at $x = 25\ \mathrm{mm}$) occurred approximately at $t = 970\ \mathrm{ms}$.

The oscillating bubble cluster radiates secondary pressure field, p_{rad}, which reflects on the side walls and forms a pressure gradient at the cluster normal to the wall, $\partial p_{\mathrm{rad}}/\partial x$. The cluster with volume $V(t)$ in the pressure gradient experienced an instantaneous force, $-V(t)\partial p_{\mathrm{rad}}/\partial x$. Since this force is composed of a product of oscillating components, time-averaging of this force leads to mean motion of the cluster. The direction of the force is determined by phase angle between the cluster oscillation and the reflected wave. It is instructive to note that in the y direction, buoyant force counterbalanced to the Bjerknes force due to the primary sound field induced by the driving acceleration (strictly, interaction with the bottom wall and top surface contribute to the force balance). This allowed the cluster to move almost in the horizontal direction. The translational dynamics in the x direction will be modeled and examined in Section 4.

At the final stage of the wall impact, we observed a jet-like motion of the bubble cluster shown in Fig. 3.9(a), which is similar to the phenomenon of a single bubble near a wall boundary; asymmetric bubble collapse leads to formation of a liquid jet directed toward the wall (Lauterborn and Bolle, 1975; Kim and Kim, 2014). The interaction between larger bubbles in the cluster and the wall boundary became much stronger than that of bubble-bubble interaction; smaller bubbles were no longer able to follow up the fast motion and left behind the cluster. After the impact on the wall, side view of cluster oscillation were captured at the corner of the container shown in Fig. 3.9(b). Once the cluster was attached to wall surface, the shape of the cluster remained almost hemispherical during oscillation, meaning that the boundary layer at the side wall does not have an impact on the cluster dynamics.Therefore, the hemispherical bubble cluster may be treated as a spherical cluster under the presence of a hemispherical mirror image that is oscillating in phase at the opposite side of the wall.

3.3 Modeling of the translational motion

3.3.1 Secondary Bjerknes force

Fig. 3.10 illustrates the top view of the vibrating water vessel. The separation between the left and right side walls is $2L$, and the center of a (hemispherical) bubble cluster in the x direction is denoted by X and is initially set at the middle of the side walls (i.e., $-L < X < L$). Here, we consider fictitious bubble clusters that are mirrored with respect to the left and right side walls; the mirrored clusters are set at $2\left(L+X\right)$ and $2\left(L-X\right)$ away from the original cluster. With these mirrored clusters, we aim to model the interaction of the oscillating bubble cluster of our target with the side walls.

We treat the acrylic side wall as an elastic boundary and assume that the secondary sound field induced by oscillation of a bubble cluster is spherically symmetric. Since the interaction between the bubble cluster and the plane boundaries is equivalent to monopole interaction with its images, the gradient of the radiation pressure at distance l away from the center of an oscillating cluster is described by (Brennen, 2013)

$$\left.\frac{\partial p_a}{\partial r}\right|_{r=l} = -\frac{\rho_L\left(R^2\ddot{R}+2R\dot{R}^2\right)}{l^2} \tag{3.4}$$

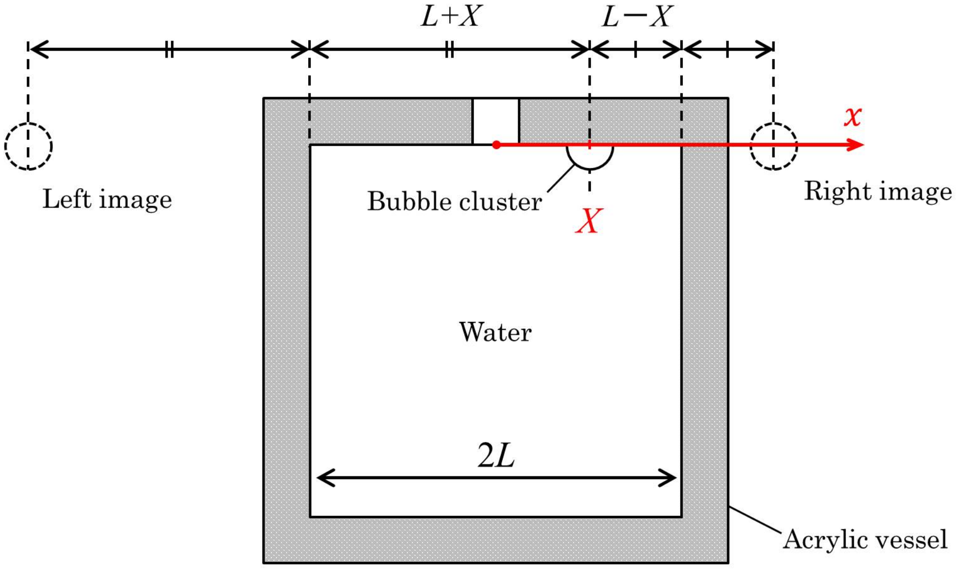

FIGURE 3.10: Schematic of the water vessel (top view). X and $2L$ denote the center of a hemispherical bubble cluster and the separation distance between the left and right side walls, respectively. The bubble cluster is mirrored with respect to the left and right side walls; the mirrored clusters are set at $2\,(L+X)$ and $2\,(L-X)$ away from the original cluster.

where dots denote time derivative, r is the radial component in the spherical coordinates, ρ_L is the (constant) density of the liquid, R is the time-varying cluster radius, and l is the distance to measurement point from the cluster center. For clarity, we account only for the adjacent two images in the x direction while neglecting any higher-order corrections. Since we will below introduce simplifications in fluid dynamics modeling of cluster translation, higher-order corrections are expected to be minor.

The radial oscillation of a spherical cluster is now expanded as Fourier series:

$$R(t) = R_0 \left[1 + \delta_0 + \sum_{k=1}^{n} \delta_k \sin(k\omega t + \phi_k) \right] \tag{3.5}$$

where R_0 is the radius of the (initially injected) bubble nucleus, ω is the angular frequency of the primary sound field induced by the external driving, and δ_k and ϕ_k ($k = 0, 1, \ldots, n$) are, respectively, the small amplitude and the phase angle of frequency component k. Here, the mean radius of the cluster, R_c, is defined as a time average of

$R(t)$ by

$$R_c = R_0\left(1+\delta_0\right). \tag{3.6}$$

Since the primary sound field governed by Eq. (3.1) is a function of y $(= H_0 - H)$ and has no significant pressure gradient in the x direction, the force acting on the cluster is only due to the reflected pressure wave from the side walls (Crum, 1975). Therefore, the pressure gradient of the reflected wave at the center of the bubble cluster is approximated by

$$\left.\frac{\partial p_a}{\partial x}\right|_{x=X} = -\left[\frac{\rho_L R_c^2 \ddot{R}}{4(L-X)^2} - \frac{\rho_L R_c^2 \ddot{R}}{4(L+X)^2}\right] Q \tag{3.7}$$

where the complex quantity Q represents acoustic energy loss through transmission to the side walls of finite acoustic impedance. To be simple, the loss Q is assumed to be constant regardless of the frequency. The time-averaged Bjerknes force (of the second kind) in the x direction is obtained as a function of position X,

$$F_B(X) = -\left\langle V(t)\frac{\partial p_a(X,t)}{\partial x}\right\rangle \tag{3.8}$$

where $\langle\cdot\rangle$ denotes a time average over the driving period $2\pi\omega^{-1}$ and $V(t) = (4\pi/3)R^3(t)$ is the volume of the spherical bubble cluster. Substituting Eq. (3.7) into Eq. (3.8) leads to

$$F_B(X) = 2\pi\rho_L\omega^2 R_c^6 \Delta^2 \left[\frac{1}{4(L-X)^2} - \frac{1}{4(L+X)^2}\right]\Re[Q] \tag{3.9}$$

where $\Re$ denotes the real part and

$$\Delta = \frac{1}{1+\delta_0}\left[\sum_{k=1}^{3} k^2\delta_k^2\right]^{\frac{1}{2}}. \tag{3.10}$$

Here, higher nonlinear corrections of the order $O(\delta_1^i\delta_2^j\delta_3^k)$ $(i+j+k \geq 3;\, i, j$ and k are integers) are neglected in Eq. (3.9). We note that a long-time behavior of the translation of an oscillating bubble cluster arises from quadratic nonlinear terms $O(k^2)$ in the expression of the Bjerknes force F_B.

3.3.2 Translational motion of the bubble cluster

The translation of the bubble cluster may be described by

$$m\frac{dU}{dt} = F_B + F_D + F_A \tag{3.11}$$

where U is the translational velocity and m is the mass within the cluster. Since the gas phase is essentially massless, the cluster mass is approximated by

$$m = \frac{4}{3}\pi\rho_L R_c^3 \left(1 - \alpha_c\right), \tag{3.12}$$

where α_c is the so-called void fraction (i.e., the volume fraction of the gas phase). The case of no bubbles is represented by $\alpha_c = 0$. The added force, F_A, arising from unsteadiness is calculated by (Barbat, Ashgriz, and Liu, 1999)

$$F_A = \frac{2}{3}\pi\rho_L R_c^3 \frac{dU}{dt}, \tag{3.13}$$

where $(2/3)\pi\rho_L R_c^3$ means the added mass. It will turn out, in the following discussion, that the added force is comparable with the cluster's inertia and needs to incorporated in the case of unsteady translation.The drag force acting on the bubble cluster is given by Levich's formula (Doinikov, 2002),

$$F_D(U) = -12\pi\mu_L R_c U \tag{3.14}$$

where μ_L is the liquid viscosity. We will show that the contribution of the drag force has negligible impact on the translation. Because of the assumption of small-amplitude oscillations, the cluster radius is evaluated as the undisturbed constant R_c in Eqs. (3.12) to (3.14) (Krefting, Toilliez, Szeri, Mettin, and Lauterborn, 2006).

The dimensionless variables (superscripted by asterisks) are defined as

$$U^* = \frac{U}{\omega L}, \quad X^* = \frac{X}{L}, \quad t^* = \omega t. \tag{3.15}$$

Substituting Eqs. (3.15) into Eq. (3.13) leads to the dimensionless form

$$\frac{dU^*}{dt^*} = B\left[\frac{1}{(1-X^*)^2} - \frac{1}{(1+X^*)^2}\right] - C_D U^*. \tag{3.16}$$

There arise the two dimensionless parameters

$$B = \frac{3}{4m^*}\left(\frac{R_c}{L}\right)^3 \Delta^2 \Re[Q], \quad C_D = \frac{3}{4m^*}\frac{R_c}{L}\frac{48}{\mathrm{Re}}. \tag{3.17}$$

where m^* is the dimensionless mass that consists of the cluster mass and the added mass is given by

$$m^* = 3 - 2\alpha_c. \tag{3.18}$$

For the case of a single bubble (not a cluster) with $\alpha_c = 1$, this reduces to $m^* = 1$. Note that B presents intensity of the acoustic radiation from the bubble cluster including the acoustic energy loss, and C_D is the drag force where $\mathrm{Re} = (2R_c)^2 \omega \nu_L^{-1}$ is Reynolds number from the cluster translation. For the inviscid case ($C_D = 0$), one can explicitly derive the exact solution of Eq. (3.16). Multiplying the both side of Eq. (3.16) by U^* and integrating with initial conditions (X_0, U_0) yield

$$U^{*2} = \left(U_0^{*2} - \frac{4B}{1-X_0^{*2}}\right) + \frac{4B}{1-X^{*2}}. \tag{3.19}$$

For reference, the eigenvalue analysis of the dynamical system described by Eq. (3.16) is presented in Appendix B.

TABLE 3.1: The cluster radius R_c and oscillation amplitudes δ_k determined by the experimentally obtained Fourier spectrum. The radius of the (initially injected) bubble nucleus is $R_0 = 1.01$ mm. The imposed sound frequency is 625 Hz.

R_c[mm]	δ_0	δ_1	δ_2	δ_3
1.68	0.665	0.216	0.169	0.0802

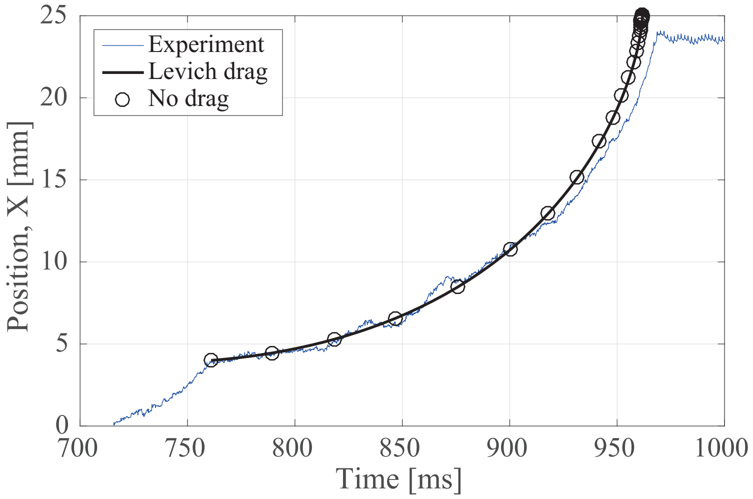

FIGURE 3.11: Comparison between the experiment and simulations: the results of the temporal evolution of the cluster position. The parameter for the acoustic energy loss is set at $\Re[Q] = 0.22$.

3.4 Comparison to the experimental result

With the model we proposed in the previous section, we now try to replicate the cluster translation observed in Fig. 3.3. The mean radius R_c and oscillation amplitudes δ_k are determined from the Fourier spectrum in Fig. 3.6(c):

$$R_c = |R_\mathrm{b}(f)|_{f=0}, \tag{3.20}$$

$$\delta_k = |R_\mathrm{b}(f)|_{f=\frac{\omega}{2\pi}\times k} \tag{3.21}$$

where k takes 1, 2, or 3. The computed values of Eqs. (3.20) and (3.21) are summarized in Table 3.1. For water, we have $\rho_L = 1000$ kg/m^3 and $\mu_L = 0.001$ Pa·s. The initial position and velocity of the bubble cluster are set, respectively, at $X_0 = 4$ mm and $U_0 = 0.01$ m/s; the simulation result is not altered significantly by slight changes in the values of X_0 and U_0. The void fraction is approximated by

$$\alpha_c \approx \left(\frac{R_0}{R_c}\right)^3 = 0.27. \tag{3.22}$$

Comparison of the temporal evolution of X between the experiment and the model is made in Fig. 3.11 where the parameter for the acoustic energy loss is set at $\Re[Q] = 0.22$. The maximum particle Reynolds number defined as $\mathrm{Re}_U = 2R_c U \nu_L^{-1}$ is approximately 1900 for $U_{\max} = 0.576\,\mathrm{m/s}$ at $X = 23\,\mathrm{mm}$. The computed curve fits well to the experiment except near the cluster-wall collision. It should be noted, however, that higher-order nonlinear corrections neglected in the present model may be needed for the short-distance interaction; the model overestimates the translational velocity as the separation distance decreases. We also note that the evaluation of the drag force acting on the cluster is unimportant, for a change in the computation is insignificant between the viscous and inviscid cases. Finally, we pointed out that the ratio of the cluster's inertia to the added inertia, $m(dU/dt)/F_A$, is 1.46, meaning that the added mass effect needs to be incorporated in the case of unsteady translation. It is therefore concluded that the translational motion is determined mainly by the secondary Bjerknes force and the inertia from the cluster's mass and the added mass in this particular example.

3.5 Summary

An experimental technique was developed to observe translation of a bubble cluster oscillating under a stationary sound field and the translational dynamics were modeled by simply extending the theory of Bjerknes. The bubble cluster shows translation toward the side wall. We explained the cluster translation as a result of the interaction with imaginary bubbles located at the opposite side of the side walls. The interaction was modeled by applying the Bjerknes theory of the second kind where the cluster is treated as a single bubble, while acoustic energy loss at the elastic wall was treated as a tuning parameter. We showed that the cluster translation observed in the experiment can be predicted properly by solving the equation of the cluster motion coupled with extended Bjerknes theory. It is concluded that the cluster translation in the present experiment is determined mainly by the secondary Bjerknes force and the cluster inertia from the cluster's mass and the added mass.

Chapter 4

Coupled bubble dynamics with an elastic boundary

This chapter provides a physical model designed for the coupled bubble and elastic wall dynamics. Bubble oscillation is modeled in an axisymmetric two dimensional domain. The ambient flow field is assumed potential, and linear elastodynamics of a circular plate with a finite thickness is coupled with the potential flow via linear boundary conditions. The basic equations of the flow field are converted in integral form for the sake of boundary element formulation. Eigenvalue analysis of the elastodynamics of the deformable wall is performed on the basis of Love's stress function in order to obtain linear normal modes of the elastic wall given a stress free boundary condition.

4.1 Boundary integral modeling of bubble dynamics

4.1.1 Basic equation

A schematic of an oscillating bubble near a circular elastic body embedded in a rigid foundation is given in Fig. 4.1. The equilibrium bubble radius is R_0. The distance between the bubble center and the elastic wall is d_w. The coordinate of system is an axisymmetric cylindrical coordinates. The bubble wall is denoted by S_b, and the wall surface is denoted by S_r and S_e for the rigid and elastic parts of the wall. The radius and thickness of the elastic body are a and h, respectively. The origin of the coordinate

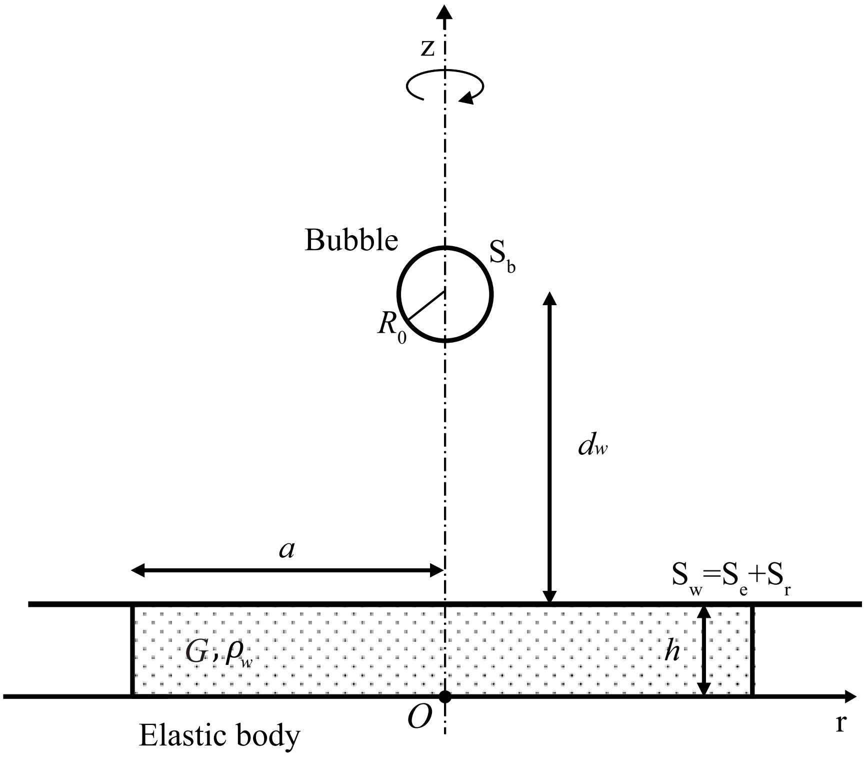

FIGURE 4.1: A schematic of bubble-wall interaction.

system is fixed on the bottom of the elastic body. The host liquid is incompressible, and the ambient fluid motion is assumed to be irrotational, indicating that boundary layer is sufficiently thin due to the slipped boundary condition at the bubble wall. It should be noted that the slipped boundary condition does not hold if the bubble wall is contaminated with chemical materials such as surfactants; Marangoni effects arising from ununiformity of the concentration of the surfactants alter the dynamical boundary condition at the bubble wall (Takagi and Matsumoto, 2011). The fluid velocity is given by a gradient of the velocity potential:

$$\boldsymbol{u} = \nabla\phi. \tag{4.1}$$

The conservation of mass leads to Laplace's equation for the velocity potential:

$$\nabla^2\phi = 0. \tag{4.2}$$

The dynamic boundary condition is satisfied on the bubble wall.

$$\frac{D\phi}{Dt} = \frac{1}{2}|\nabla\phi|^2 - \frac{p_b - p_\infty}{\rho_L} \tag{4.3}$$

where D/Dt is the material derivative, p_b is the liquid pressure at the bubble wall, p_∞ is the pressure in the far field and ρ_L is the liquid density. The position of a liquid particle on the bubble wall satisfies the kinetic boundary condition:

$$\frac{d\boldsymbol{x}}{dt} = \nabla\phi \tag{4.4}$$

where $\boldsymbol{x}$ is the position of a fluid particle on the bubble wall. On the free surface, no shear boundary condition is satisfied.

$$\frac{D\phi}{Dt} = \frac{1}{2}|\nabla\phi|^2 + \frac{p_\infty(t)}{\rho_L} - \frac{P_{G0}}{\rho_L}\left(\frac{V_0}{V}\right)^\kappa + \frac{S}{\rho_L}(\nabla\cdot\boldsymbol{n}) + \frac{2}{\mathrm{Re}}(\boldsymbol{n}\nabla\boldsymbol{n}). \tag{4.5}$$

where P_{G0} and V_0 are the equilibrium gas pressure and the volume of the bubble content, S is the surface tension and $\boldsymbol{n}$ is the unit normal directed away from liquid. The viscous collection (Lundgren and Mansour, 1988) is incorporated in the last term on the right hand side of Eq. (4.5).

4.1.2 Boundary integral formulation

Laplace's equation is solved for ϕ and $\partial\phi/\partial n$ in the form of an integral equation:

$$\begin{aligned}\alpha(\boldsymbol{x}_0) f(\boldsymbol{x}_0) = &-\int_S G^{AX}(\boldsymbol{x},\boldsymbol{x}_0)\left[\boldsymbol{n}\cdot\nabla f(\boldsymbol{x})\right] r(\boldsymbol{x})\, dl(\boldsymbol{x}) \\ &+PV\int_S f(\boldsymbol{x})\left[\boldsymbol{n}\cdot\nabla G^{AX}(\boldsymbol{x},\boldsymbol{x}_0)\right] r(\boldsymbol{x})\, dl(\boldsymbol{x})\end{aligned} \tag{4.6}$$

where $\boldsymbol{x}$ denotes the observation point in the cylindrical coordinates, $\boldsymbol{x}_0$ is the source point of $G(\boldsymbol{x},\boldsymbol{x}_0)$, and $G(\boldsymbol{x},\boldsymbol{x}_0)$ is the fundamental solution of Laplace's equation given by

$$G\left(\boldsymbol{x},\boldsymbol{x}_0\right)=\frac{1}{4\pi\left|\boldsymbol{x}-\boldsymbol{x}_0\right|}. \tag{4.7}$$

For axisymmetric flow in the cylindrical coordinates, the Green function is integrated in θ and the axisymmetric Green function is given by

$$G^{AX}\left(\boldsymbol{x},\boldsymbol{x}_0\right)=\frac{F(k)}{\pi\sqrt{(z-z_0)^2+(r+r_0)^2}}. \tag{4.8}$$

where $F(k)$ is the elliptic integral of the first kind given by

$$F(k)=\int_0^{\frac{\pi}{2}}\frac{d\eta}{\sqrt{1-k^2\cos^2\eta}}. \tag{4.9}$$

The parameter k is a function of the observation point and of the position of the source point as follows:

$$k^2=\frac{4rr_0}{(z-z_0)^2+(r+r_0)^2}. \tag{4.10}$$

The gradient of the axisymmetric Green function are

$$\frac{\partial G^{AX}}{\partial z}=-\frac{1}{4\pi}(z-z_0)I_{30}, \tag{4.11}$$

$$\frac{\partial G^{AX}}{\partial r}=-\frac{1}{4\pi}\left(rI_{30}-r_0I_{31}\right). \tag{4.12}$$

The integral quantities in Eq. (4.11) and (4.12) are given by

$$I_{30}=\frac{4}{\pi\left[(z-z_0)^2+(r+r_0)^2\right]^{\frac{3}{2}}}\frac{E(k)}{1-k^2}, \tag{4.13}$$

$$I_{31}=\frac{4}{\pi\left[(z-z_0)^2+(r+r_0)^2\right]^{\frac{3}{2}}}\frac{1}{k^2}\left[-2F(k)+\frac{2-k^2}{1-k^2}E(k)\right] \tag{4.14}$$

where $E(k)$ is the elliptic integral of the second kind defined as

$$E(k) = \int_0^{\frac{\pi}{2}} \sqrt{1 - k^2 \cos^2 \eta}\, d\eta. \tag{4.15}$$

4.1.3 Boundary condition

On the elastic part of the wall, the fluid motion is coupled with the elastic wall via following linearized boundary conditions:

$$\frac{\partial \phi}{\partial z} = \frac{\partial w}{\partial t}, \tag{4.16}$$

$$\frac{\partial^2 \phi}{\partial z \partial t} = \frac{\partial^2 w}{\partial t^2}, \tag{4.17}$$

$$p_w(r,t) = -\rho_L \frac{\partial \phi}{\partial t} + p_\infty \tag{4.18}$$

where w is the vertical displacement of the elastic boundary, and $p_w(r,t)$ is the pressure at the wall. Eq. (4.18) is the linearized Bernoulli equation. On the rigid part of the wall, the normal velocity and acceleration are set to zero:

$$\frac{\partial \phi}{\partial z} = 0, \tag{4.19}$$

$$\frac{\partial^2 \phi}{\partial z \partial t} = 0. \tag{4.20}$$

4.2 Linear elastodynamics of a circular plate

4.2.1 Basic equation

The elastodynamics of an axisymmetric elastic body is described by Cauchy's equation of motion:

$$\frac{\partial \tau_{rr}}{\partial r} + \frac{\partial \tau_{rz}}{\partial z} + \frac{\tau_{rr} - \tau_{\theta\theta}}{r} = \rho_w \frac{\partial^2 u_r}{\partial t^2}, \tag{4.21}$$

$$\frac{\partial \tau_{zr}}{\partial r} + \frac{\partial \tau_{zz}}{\partial z} + \frac{\tau_{zr}}{r} = \rho_w \frac{\partial^2 u_z}{\partial t^2} \tag{4.22}$$

where ρ_w is the solid wall density, u_r and u_z are the displacements in the r and z directions, and τ_{ij} is the stress tensor of the isotropic linear elasticity given by

$$\tau_{ij} = \Lambda\delta_{ij}\left(\frac{\partial u_r}{\partial r} + \frac{\partial u_r}{r} + \frac{\partial u_z}{\partial z}\right) + G\left(\frac{\partial u_i}{\partial r_j} + \frac{\partial u_j}{\partial x_i}\right) \tag{4.23}$$

where i and j take r or z, Λ and G are Lamé's constants, which are related via Poisson's ratio, ν, as

$$\Lambda = \frac{2(1-\nu)}{1-2\nu}G \tag{4.24}$$

which takes infinity for the case of incompressible solid (ν = 0.5).

4.2.2 Dynamic Love's stress function

To simplify the eigenvalue analysis, the displacements and stresses are expressed by only one scalar function, $\chi(r, z, t)$, in the form of

$$u_r(r,z,t) = -\frac{1}{2G}\frac{\partial^2\chi}{\partial r\partial z}, \tag{4.25}$$

$$u_z(r,z,t) = \frac{1}{2G}\left[(1-2\nu)\left(\nabla^2\chi - \frac{1}{c_s^2}\frac{\partial^2\chi}{\partial t^2}\right) + \nabla_r^2\chi\right], \tag{4.26}$$

$$\tau_{rr}(r,z,t) = \frac{\partial}{\partial z}\left[\nu\left(\nabla^2\chi - \frac{1}{c_s^2}\frac{\partial^2\chi}{\partial t^2}\right) - \frac{\partial^2\chi}{\partial r^2}\right], \tag{4.27}$$

$$\tau_{\theta\theta}(r,z,t) = \frac{\partial}{\partial z}\left[\nu\left(\nabla^2\chi - \frac{1}{c_s^2}\frac{\partial^2\chi}{\partial t^2}\right) - \frac{1}{r}\frac{\partial\chi}{\partial r}\right], \tag{4.28}$$

$$\tau_{zz}(r,z,t) = \frac{\partial}{\partial z}\left[(1-\nu)\left(\nabla^2\chi - \frac{1}{c_s^2}\frac{\partial^2\chi}{\partial t^2}\right) + \nabla_r^2\chi(r,z,t)\right], \tag{4.29}$$

$$\tau_{rz}(r,z,t) = \frac{\partial}{\partial r}\left[(1-\nu)\left(\nabla^2\chi - \frac{1}{c_s^2}\frac{\partial^2\chi}{\partial t^2}\right) - \frac{\partial^2\chi}{\partial z^2}\right] \tag{4.30}$$

where χ is dynamical Love's stress function, $c_s = \sqrt{G/\rho_w}$ is the speed of transversal sound wave, and ∇_r^2 is a Laplace operator with respect to the radial coordinate given by

$$\nabla_r^2 = \frac{1}{r}\frac{\partial}{\partial r}\left(r\frac{\partial}{\partial r}\right) = \frac{\partial^2}{\partial r^2} + \frac{1}{r}\frac{\partial}{\partial r}. \tag{4.31}$$

The stress function identically satisfies Eq. (4.21) and yields a biharmonic problem described by Eq. (4.22) as will be presented in the following section.

4.2.3 Dimensionless form

The initial bubble radius and the oscillation period of the adiabatic natural frequency of an isolated spherical bubble are chosen to be the characteristic length and time scales. The coordinates of the system and variables are transformed to dimensionless form:

$$r^* = \frac{r}{R_0},\ \ z^* = \frac{z}{R_0}\ ,t^* = \omega_N t, \tag{4.32}$$

$$u_r^* = \frac{u_r}{R_0},\ \ u_z^* = \frac{u_z}{R_0}, \tag{4.33}$$

$$\chi^* = \frac{\chi}{2GR_0^3}. \tag{4.34}$$

Navier's equation in dimensionless form is

$$\nabla^{*2}\mathbf{u}^* + \frac{1}{1-2\nu}\nabla^*(\nabla^*\cdot\mathbf{u}^*) = \frac{1}{M_s^2}\frac{\partial^2\mathbf{u}^*}{\partial t^{*2}} \tag{4.35}$$

where $M_s^2 = G/\left(\rho_w\omega_N^2 R_0^2\right)$ is the dimensionless speed of the transversal sound wave. Note that the second term on the left hand side of Eq. (4.35) is dropped for the case of incompressible elasticity $\nu = 0.5$). The dimensionless displacements and stresses are

$$u_r^* = -\frac{\partial^2\chi^*}{\partial r^*\partial z^*}, \tag{4.36}$$

$$u_z^* = (1-2\nu)\left[\nabla^{*2}\chi^* - \frac{1}{M_s^2}\frac{\partial^2\chi}{\partial t^2}\right] + \nabla_r^2\chi^*, \tag{4.37}$$

$$\tau_{rr}^* = \frac{\partial}{\partial z^*}\left[\nu\left(\nabla^2\chi^* - \frac{1}{M_s^2}\frac{\partial^2\chi^*}{\partial t^{*2}}\right) - \frac{\partial^2\chi^*}{\partial r^{*2}}\right], \tag{4.38}$$

$$\tau_{\theta\theta}^* = \frac{\partial}{\partial z^*}\left[\nu\left(\nabla^2\chi^* - \frac{1}{M_s^2}\frac{\partial^2\chi^*}{\partial t^{*2}}\right) - \frac{1}{r^*}\frac{\partial\chi^*}{\partial r^*}\right], \tag{4.39}$$

$$\tau_{zz}^* = \frac{\partial}{\partial z^*}\left[(1-\nu)\left(\nabla^2\chi^* - \frac{1}{M_s^2}\frac{\partial^2\chi^*}{\partial t^{*2}}\right) + \nabla_r^{*2}\chi\right], \tag{4.40}$$

$$\tau_{rz}^* = \frac{\partial}{\partial r^*}\left[(1-\nu)\left(\nabla^2\chi^* - \frac{1}{M_s^2}\frac{\partial^2\chi^*}{\partial t^{*2}}\right) - \frac{\partial^2\chi^*}{\partial z^{*2}}\right]. \tag{4.41}$$

4.2.4 Boundary condition

Displacement boundary conditions are imposed at $z = 0$ and $r = a$:

$$u_r(a, z, t) = 0, \tag{4.42}$$

$$u_z(r, 0, t) = 0. \tag{4.43}$$

Stress boundary conditions are imposed at $z = 0$ and $r = a$. At the bottom end, shear free boundary condition is used, while stress free condition is used for the free surface:

$$\tau_{rz}(r, 0, t) = 0, \tag{4.44}$$

$$\tau_{rz}(r, h, t) = 0, \tag{4.45}$$

$$\tau_{zz}(r, h, t) = 0. \tag{4.46}$$

4.2.5 Eigenvalue analysis

On the basis of the stress function, eigenfunctions and eigenfrequencies are derived as follows. For brevity, subscripts for dimensionless parameters are omitted. The equation of motion in the z direction is a biharmonic equation of χ:

$$\nabla^4\chi + \left(\frac{1}{M_s^2} + \frac{1}{M_p^2}\right)\nabla^2\ddot{\chi} + \frac{1}{M_s^2 M_p^2}\ddddot{\chi} = 0 \tag{4.47}$$

where dots denote differentiation with respect to time, and M_p is the speed of the longitudinal sound wave. The stress function is separated in the form

$$\chi(r, z, t) = \mathcal{R}(r)\mathcal{Z}(z)e^{ipt} \tag{4.48}$$

where p is the eigenfrequency, and $\mathcal{R}(r)$ and $\mathcal{Z}(z)$ are the eigenfunctions in the r and z directions, respectively. Substituting into Eq. (4.22) leads to

$$\begin{aligned}\frac{\nabla_r^4\mathcal{R}}{\mathcal{R}}+\left(\frac{p^2}{M_s^2}+\frac{p^2}{M_p^2}\right)\frac{\nabla_r^2\mathcal{R}}{\mathcal{R}}+2\frac{\nabla_r^2\mathcal{R}}{\mathcal{R}}\frac{\mathcal{Z}''}{\mathcal{Z}}&\\+\left[\frac{p^4}{M_s^2M_p^2}+\left(\frac{p^2}{M_s^2}+\frac{p^2}{M_p^2}\right)\frac{\mathcal{Z}''}{\mathcal{Z}}+\frac{\mathcal{Z}''''}{\mathcal{Z}}\right]&=0.\end{aligned} \tag{4.49}$$

The fourth term on the left hand side of Eq. (4.49) should be a function of either r or z. Therefore, we consider the case of

$$\frac{\nabla_r^2\mathcal{R}}{\mathcal{R}}=-\lambda^2 \tag{4.50}$$

where λ is a positive real or a pure imaginary constant. Thus, $\mathcal{R}$ turns out to be expressed by

$$\mathcal{R}(r)=A_1J_0(\lambda r) \tag{4.51}$$

where J_0 is the Bessel function of the first kind of the zeroth order. Substituting Eq. (4.51) into Eq. (4.49) yields

$$\begin{aligned}\mathcal{Z}''''+\left(\frac{p^2}{M_s^2}+\frac{p^2}{M_p^2}-2\lambda^2\right)\mathcal{Z}''&\\-\left(\frac{p}{M_s}-\lambda\right)\left(\frac{p}{M_s}+\lambda\right)\left(\frac{p}{M_p}-\lambda\right)\left(\frac{p}{M_p}+\lambda\right)\mathcal{Z}&=0.\end{aligned} \tag{4.52}$$

The solution of Eq. (4.52) can be given in the form of

$$\mathcal{Z}(z)=B_1\cos k_sz+B_2\sin k_sz+B_3\cosh k_pz+B_4\sinh k_pz \tag{4.53}$$

where k_s and k_p, respectively, are the complex wave numbers of the transversal and the longitudinal sound waves given by

$$k_s = \sqrt{\lambda^2 - \frac{p^2}{c_s^2}}, \tag{4.54}$$

$$k_p = \sqrt{\lambda^2 - \frac{p^2}{c_p^2}}. \tag{4.55}$$

For incompressible elasticity, $k_p = \lambda$ because of the infinite speed of sound of the longitudinal wave. Eq. (4.42) leads to

$$J_1\left(a\lambda\right) = 0 \tag{4.56}$$

where a is the radius of the elastic plate. Therefore,

$$\lambda_m = \frac{\alpha_m}{a} \tag{4.57}$$

where α_m is the mth zero of the Bessel function of first kind of the zeroth order. Similarly Eq. (4.43) and (4.44) yield

$$B_1 = 0, \tag{4.58}$$

$$B_3 = 0. \tag{4.59}$$

Stress free boundary conditions at $z = h$ lead to following two linear equations with respect to B_2 and B_4:

$$B_2 k_s \left(-M_s^2 k_s^2 + p^2\right) \cos k_s h + B_4 k_p \left(M_s^2 k_p^2 + p^2\right) \cosh k_p h = 0, \tag{4.60}$$

$$B_2 M_s^2 \left(k_s^2 - \lambda_m^2\right) \sin k_s h + B_4 M_s^2 \left(k_p^2 + \lambda_m^2\right) \sinh k_p h = 0. \tag{4.61}$$

To determine non-zero B_2 and B_4, the determinant of the set of Eq. (4.60) and Eq. (4.61) must be zero, leading to

$$\begin{aligned} & k_p \left(k_s^2 - \lambda_m^2\right) \left[M_s^2 \left((k_p^2 - 3\lambda_m^2\right) + p^2\right] \cosh k_p h \sin k_s h \\ & - k_s \left(k_p^2 + \lambda_m^2\right) \left[M_s^2 \left(k_s^2 + 3\lambda_m^2\right) - p^2\right] \sinh k_p h \cos k_s h = 0. \end{aligned} \tag{4.62}$$

The eigenfrequency of (m, n) mode, p_n, is numerically obtained from the nth zero of Eq. (4.62). The corresponding eigenfunction is

$$\chi_{mn}(r, z, t) = J_0\left(\lambda_n r\right) \left[\sin k_s z + \frac{\left(k_s + \lambda_m\right)\left(k_s - \lambda_m\right) \sin k_s h}{2\lambda_m^2 \sinh k_p h} \sinh \lambda_m z\right]. \tag{4.63}$$

The boundary conditions of $\mathscr{Z}(z)$ are summarized below for use of the next section:

$$\mathscr{Z}_n(0) = 0, \tag{4.64}$$

$$\mathscr{Z}_n''(0) = 0, \tag{4.65}$$

$$\mathscr{Z}_n''(h) + \lambda_m^2 \mathscr{Z}_n(h) = 0, \tag{4.66}$$

$$\mathscr{Z}_n'''(h) + \left(\frac{p_n^2}{M_s^2} - 3M_s^2\lambda_m^2\right) \mathscr{Z}_n'(h) = 0. \tag{4.67}$$

In Fig. 4.2, the eigenfrequencies of the $(1, m)$ modes are plotted as a function of the wall thickness. The eigenfrequency decreases with increasing the wall thickness and the mode number.

4.2.6 Orthogonality of the eigenfunction

In this section, the orthogonality of the differential operator of Eq. (4.52) is examined, and an adjoint function which is orthogonal to $\mathscr{Z}_n(z)$ is developed. Multiplying a scalar function of z, $\Phi(z)$, on the left hand side of Eq. (4.52) and integrating with respect to z from 0 to h yield

$$\int_0^h \left(\mathcal{L}_n - V_{n2}^2\right) \mathscr{Z}_n \Phi dz = 0 \tag{4.68}$$

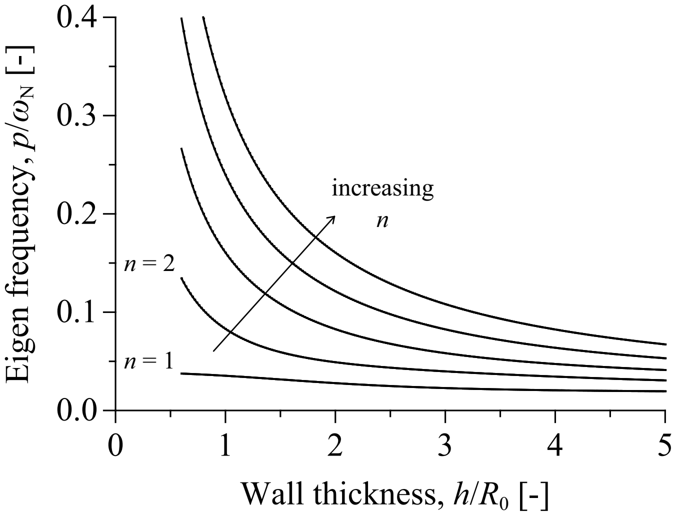

FIGURE 4.2: Eigenfrequency of the $(1, n)$ eigenmodes (n = 1, 2, 3, 4 and 5) as a function of the wall thickness for the case of (a) G = 1.5 kPa, and (b) G = 15 kPa. The eigenfrequency and the wall thickness are normalized, respectively, by the adiabatic natural frequency and the initial radius of an isolated bubble.

where $\mathcal{L} = (\partial^4/\partial z^4) + V_{n1}^2(\partial^2/\partial z^2)$ denotes the linear differential operator, and V_{n1}^2 and V_{n2}^2 are given by the eigenvalues of the (m, n) mode:

$$V_{n1}^2 = \frac{p_n^2}{M_s^2} - 2\lambda_m^2, \tag{4.69}$$

$$V_{n2}^2 = \lambda_m^2\left(\frac{p_n^2}{M_s^2} - \lambda_m\right). \tag{4.70}$$

Integrating Eq. (4.68) by part leads to

$$\begin{aligned}\int_0^h \left(\mathcal{L}_n - V_{n2}^2\right)\mathcal{Z}_n\Phi dz = &\int_0^h \mathcal{Z}_n\left(\Phi'''' + V_{n1}^2\mathcal{Z}_n''\Phi - V_{n2}^2\Phi\right)dz\\ &- \Phi(0)\mathcal{Z}_n'''(0) - \left[V_{n1}^2\mathcal{Z}_n(0) + \mathcal{Z}_n''(0)\right]\mathcal{Z}_n'(0)\\ &- \left[\left(V_{n1} - \lambda_m\right)\left(V_{n1} + \lambda_m\right)\Phi'(h) + \Phi'''(h)\right]\mathcal{Z}_n(h)\\ &+ \left[\left(-\frac{p_n^2}{M_s^2} + V_{n1}^2 + 3\lambda_m^2\right)\Phi(h) + \Phi''(h)\right]\mathcal{Z}_n'(h)\\ &= 0\end{aligned} \tag{4.71}$$

where Eq. (4.64) to (4.67) are used. Suppose that $\Phi_l(z)$ undergoes the same differential operator:

$$\Phi_l'''' + V_{l1}^2 \Phi_l'' - V_{l2}^2 \Phi_l = 0, \tag{4.72}$$

$$\tag{4.73}$$

and satisfies following boundary conditions:

$$\Phi(0) = 0, \tag{4.74}$$

$$\Phi''(0) = 0, \tag{4.75}$$

$$\left(V_{n1} - \lambda\right)\left(V_{n1} + \lambda\right)\Phi'(h) + \Phi'''(h) = 0, \tag{4.76}$$

$$\left(-\frac{p_n^2}{M_s^2} + V_{n1}^2 + 3\lambda_m^2\right)\Phi(h) + \Phi''(h) = 0. \tag{4.77}$$

It therefore turns out from Eq. (4.71) that $\mathcal{Z}_n(z)$ and $\Phi_l(z)$ have a following orthogonal relation for $n \neq l$:

$$\begin{aligned}
&\int_0^h \mathcal{Z}_n \left(\Phi_l'''' + V_{n1}^2 \mathcal{Z}_n'' \Phi_l - V_{n2}^2 \Phi_l\right) dz \\
&= \int_0^h \mathcal{Z}_n \left[\left(V_{n1}^2 - V_{l1}^2\right)\Phi_l'' - \left(V_{n2}^2 - V_{l2}^2\right)\Phi_l\right] dz \\
&= \int_0^h \mathcal{Z}_n \left(\frac{V_{n1}^2 - V_{l1}^2}{V_{n2}^2 - V_{l2}^2}\Phi_l'' - \Phi_l\right) dz \\
&= \int_0^h \mathcal{Z}_n \left(\lambda_m^{-2}\Phi_l'' - \Phi_l\right) dz \\
&= 0.
\end{aligned} \tag{4.78}$$

Consequently, the orthogonal function of $\mathcal{Z}_n(z)$ is obtained for $n \neq l$:

$$\int_0^h \mathcal{Z}_n \Psi_l dz = 0 \tag{4.79}$$

with

$$\Psi_l(z) = \frac{\lambda_m^{-2}\Phi_l''(z) - \Phi_l(z)}{\lambda_m^{-2}\Phi_l''(h) - \Phi_l(h)} \tag{4.80}$$

which is normalized such that $\Psi(h) = 1$.

4.2.7 Wave equation of the wall surface

In this section, the equation of the normal modes for the wall surface (i.e., the wave equation of the wall surface) is derived for the case of incompressible elasticity by integrating the equation of motion in the z direction. The displacement in the r direction is neglected, and the displacement in the z direction is expanded in a series of the eigenfunction:

$$u_r(r,z,t) \approx 0, \tag{4.81}$$

$$u_z(r,z,t) = w(r,t)\sum_{n=1}^{\infty} \mathcal{Z}_n(z) \tag{4.82}$$

where $w(r,t) = u_z(r,h,t)$ is the vertical displacement of the boundary at $z = h$. Substituting Eq. (4.82) into Eq. (4.37) and integrating with respect to z with ν = 1/2 leads to

$$\sum_{i=1}^{\infty}\left[\frac{\partial^2 w}{\partial t^2}\int_0^h \mathcal{Z}_i(z)\Psi_j(z)dz - 2M_s^2 w(r,t)\int_0^h \frac{\partial^2\mathcal{Z}_i(z)}{\partial z^2}\Psi_j(z)dz \right.$$
$$\left. - M_s^2\nabla_r^2 w(r,t)\int_0^h \frac{\partial\mathcal{Z}_i(z)}{\partial z}\Psi_j(z)dz\right] = 0. \tag{4.83}$$

The second term on the left hand side of Eq. (4.83) can be integrated by part:

$$\begin{aligned}\int_0^h \frac{\partial^2\mathcal{Z}_i(z)}{\partial z^2}\Psi_j(z)dz =& \left[\frac{\partial\mathcal{Z}_i(z)}{\partial z}\Psi_j(z)\right]_0^h - \int_0^h \frac{\partial\mathcal{Z}_i(z)}{\partial z}\frac{\partial\Psi_j(z)}{\partial z}dz \\ =& \mathcal{Z}_i'(h)\Psi_j(h) - \int_0^h \mathcal{Z}_i'(z)\Psi_j'(z)dz.\end{aligned} \tag{4.84}$$

Substituting Eq. (4.84) into Eq. (4.83) results in

$$\begin{aligned}\ddot{w}(r,t)\int_0^h \mathcal{Z}_j(z)\Psi_j(z)dz - 2M_s^2 w(r,t)\sum_{i=1}^{\infty}\mathcal{Z}_i'(h)\Psi_j(h)\\ + 2M_s^2 w(r,t)\sum_{i=1}^{\infty}\int_0^h \mathcal{Z}_i'(h)\Psi_j'(z)dz\\ - M_s^2\nabla_r^2 w(r,t)\int_0^h \mathcal{Z}_j(z)\Psi_j(z)dz = 0 \qquad (4.85)\end{aligned}$$

where the orthogonal relation is used at the integrals of the first and fourth terms. Here, the stress boundary condition at $z = h$ is described by

$$\begin{aligned}p_w(r,t) + p_\infty &= \left.\frac{\partial \tau_{zz}}{\partial z}\right|_{z=h}\\ &= 2M_s^2 w(r,t)\sum_{i=1}^{\infty}\mathcal{Z}_i'(h). \qquad (4.86)\end{aligned}$$

Thus, the second term on the left hand side of Eq. (4.85) is replaced by the distributed pressure due to the fluid motion at the wall boundary.

$$\begin{aligned}\rho_w\ddot{w}(r,t)\int_0^h \mathcal{Z}_j(z)\Psi_j(z)dz + 2M_s^2 w(r,t)\sum_{i=1}^{\infty}\int_0^h \mathcal{Z}_i'(h)\Psi_j'(z)dz\\ - M_s^2\nabla_r^2 w(r,t)\int_0^h \mathcal{Z}_i(z)\Psi_j(z)dz = p_w(r,t) + p_\infty \qquad (4.87)\end{aligned}$$

Therefore, the equation of motion of (m, n) mode is obtained in the form of

$$M_n^*\ddot{w}(r,t) + K_n^* w(r,t) - T_n^*\nabla_r^2 w(r,t) = p_w(r,t) + p_\infty \qquad (4.88)$$

where

$$M_n^*(h) = \rho_w\int_0^h \mathcal{Z}_n(z)\Psi_n(z)dz, \qquad (4.89)$$

$$K_n^*(h) = 2M_s^2\sum_{i=1}^{\infty}\int_0^h \mathcal{Z}_i'(h)\Psi_n'(z)dz, \qquad (4.90)$$

$$T_n^*(h) = M_s^2\int_0^h \mathcal{Z}_n(z)\Psi_n(z)dz \qquad (4.91)$$

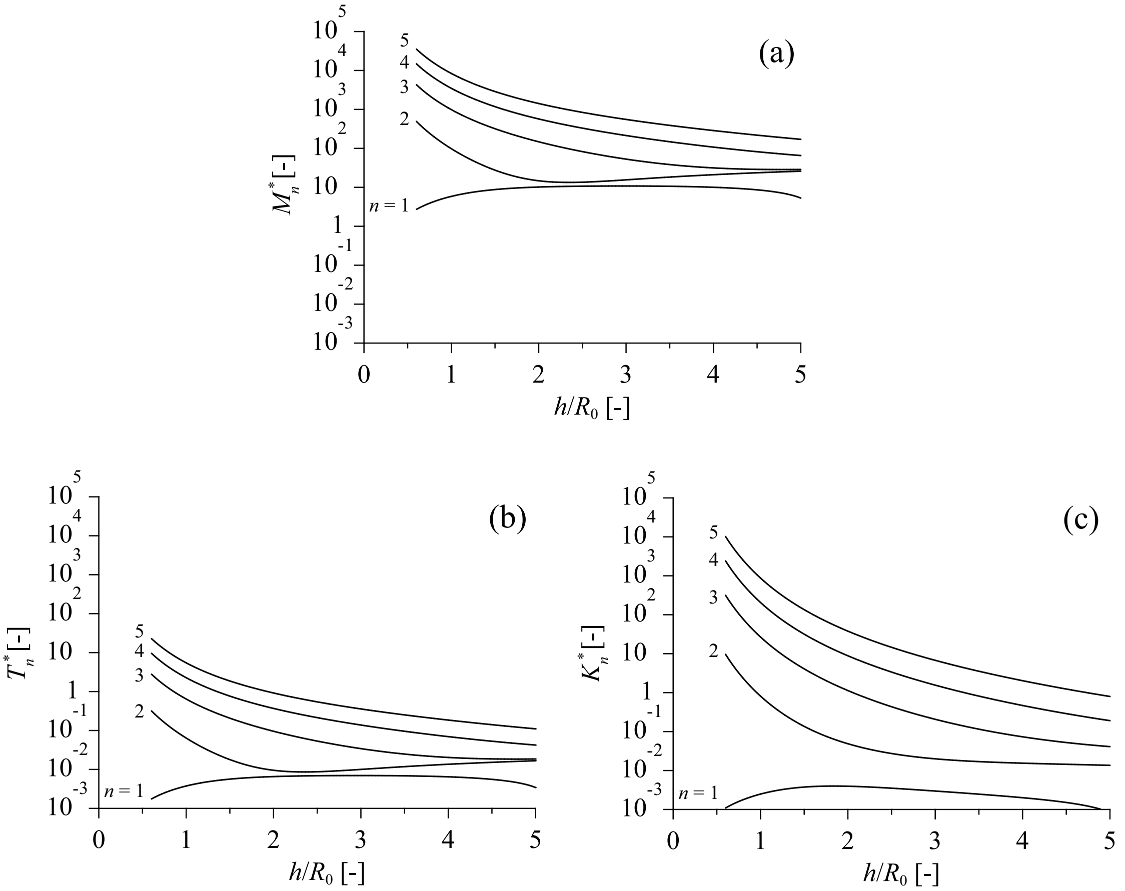

FIGURE 4.3: The parameters of the $(1, n)$th eigenmode (n = 1, 2, 3, 4 and 5) as a function of the wall thickness: (a) mass, (b) tension and (c) stiffness.

The three terms on the left side of Eq. (4.88) are due to inertia, tension and stiffness of the elasticity. Note that Eq. (4.91) are coupled with the other modes via the second term, which will be approximated by a single mode in the following numerical formulation:

$$K_n^*(h) \approx 2M_s^2 \int_0^h \mathcal{Z}_n'(h)\Psi_n'(z)dz. \tag{4.92}$$

4.3 Numerical method

In what follows, a numerical method for the coupled bubble-wall model developed in the previous sections. The flow field is described in a set of boundary integral equations and formulated in the form of boundary element framework. The linear wave equation of the elastic boundary is discretized using the Galerkin approximation and coupled with the bubble oscillation. Smoothing technique and reconstruction of nodes are employed to suppress numerical instabilities arising from time stepping of moving boundaries.

4.3.1 Spatial discretization

The rigid and elastic part of the solid boundaries and the bubble wall are discretized into N_1, N_2 and N_3 linear elements, respectively using linear isoparametric functions given by

$$f_1(\eta) = \frac{1}{2}(1-\eta), \quad f_2(\eta) = \frac{1}{2}(1+\eta) \tag{4.93}$$

where η is the local coordinate which takes -1 to 1 along each element. The global coordinates are interpolated by Eq. (4.93):

$$r = f_1(\eta) r_i + f_2(\eta) r_{i+1}, \tag{4.94}$$

$$z = f_1(\eta) z_i + f_2(\eta) z_{i+1} \tag{4.95}$$

where subscripts stand for the number of nodes. The velocity potential and its normal derivative on the elements are also interpolated in the same manner.

$$\phi(\boldsymbol{x}) = f_1(\eta)\phi_i + f_2(\eta)\phi_{i+1}, \tag{4.96}$$

$$\frac{\partial \phi(\boldsymbol{x})}{\partial n} = f_1(\eta)\left(\frac{\partial \phi}{\partial n}\right)_i + f_2(\eta)\left(\frac{\partial \phi}{\partial n}\right)_{i+1}. \tag{4.97}$$

The line element along the boundaries is transformed with respect to the local coordinate:

$$dl(\boldsymbol{x}) = \left\| \frac{\partial \boldsymbol{x}}{\partial \eta} \right\| d\eta = \sqrt{\left(\frac{\partial z}{\partial \eta}\right)^2 + \left(\frac{\partial r}{\partial \eta}\right)^2} d\eta. \tag{4.98}$$

Substituting the above discretized variables, the discretized form of the boundary integral equation is given by

$$\begin{aligned}\frac{\alpha_i}{4\pi}\phi_i = &-\sum_{k=1}^{N}\left\{\int_{C_k} G^{AX}\left[f_1(\eta)\left(\frac{\partial\phi}{\partial n}\right)_k + f_2(\eta)\left(\frac{\partial\phi}{\partial n}\right)_{k+1}\right]\left[f_1(\eta)r_k + f_2(\eta)r_{k+1}\right]\frac{l_k}{2}d\eta\right\}\\ &+\sum_{k=1}^{N}\left\{\int_{C_k}^{PV}\left[\boldsymbol{n}\cdot\nabla G^{AX}\right]\left[f_1(\eta)\phi_k + f_2(\eta)\phi_{k+1}\right]\left[f_1(\eta)r_k + f_2(\eta)r_{k+1}\right]\frac{l_k}{2}d\eta\right\}\end{aligned} \tag{4.99}$$

where C_k indicates the contour of the kth element. To close the set of equations, the boundary integral equation with the source point $\boldsymbol{x}_i$ is coupled for all the nodes:

$$\begin{aligned}&\begin{bmatrix}\ddots & & 0\\ & \alpha_i & \\ 0 & & \ddots\end{bmatrix}\begin{bmatrix}\vdots\\ \phi_i\\ \vdots\end{bmatrix} =\\ &-\begin{bmatrix}A^{(1)}_{1,1} & & \vdots & & A^{(2)}_{1,N}\\ \vdots & \cdots & A^{(2)}_{i,k-1}+A^{(1)}_{i,k} & \cdots & \vdots\\ A^{(1)}_{N+1,1} & & \vdots & & A^{(2)}_{N+1,N}\end{bmatrix}\begin{bmatrix}\vdots\\ \left(\frac{\partial\phi}{\partial n}\right)_i\\ \vdots\end{bmatrix}\\ &+\begin{bmatrix}B^{(1)}_{1,1} & & \vdots & & B^{(2)}_{1,N}\\ \vdots & \cdots & B^{(2)}_{i,k-1}+B^{(1)}_{i,k} & \cdots & \vdots\\ B^{(1)}_{N+1,1} & & \vdots & & B^{(2)}_{N+1,N}\end{bmatrix}\begin{bmatrix}\vdots\\ \phi_i\\ \vdots\end{bmatrix}\end{aligned} \tag{4.100}$$

where the elements in the coefficient matrices are given by

$$A^{(1)}_{i,k} = \int_{C_k} G^{AX} f_1(\eta)\left[f_1(\eta)r_k + f_2(\eta)r_{k+1}\right]\frac{l_k}{2}d\eta, \tag{4.101}$$

$$A^{(2)}_{i,k} = \int_{C_k} G^{AX} f_2(\eta)\left[f_1(\eta)r_k + f_2(\eta)r_{k+1}\right]\frac{l_k}{2}d\eta, \tag{4.102}$$

$$B^{(1)}_{i,k} = \int_{C_k}^{PV}\left[\boldsymbol{n}\cdot\nabla G^{AX}\right] f_1(\eta)\left[f_1(\eta)r_k + f_2(\eta)r_{k+1}\right]\frac{l_k}{2}d\eta, \tag{4.103}$$

$$B^{(2)}_{i,k} = \int_{C_k}^{PV}\left[\boldsymbol{n}\cdot\nabla G^{AX}\right] f_2(\eta)\left[f_1(\eta)r_k + f_2(\eta)r_{k+1}\right]\frac{l_k}{2}d\eta. \tag{4.104}$$

In a matrix form,

$$H_{ji}\left(\frac{\partial\phi}{\partial n}\right)_i = \left(\delta_{ij}\alpha_i - G_{ji}\right)\phi_i, \tag{4.105}$$

where δ_{ij} is the Kronecker delta and

$$H_{ji} = A^{(2)}_{j-1,i} + A^{(1)}_{j,i} \qquad (i,j = 1,\cdots,N+1), \tag{4.106}$$

$$G_{ji} = B^{(2)}_{j-1,i} + B^{(1)}_{j,i} \qquad (i,j = 1,\cdots,N+1). \tag{4.107}$$

The unit normals on nodes are defined as a wighted average of the two adjacent unit normals on the elements. The weight factors are with resect to the element length of the two adjacent element:

$$\tilde{\boldsymbol{n}}_i = \frac{l_{i+1}\boldsymbol{n}_i + l_i\boldsymbol{n}_{i+1}}{l_i + l_{i+1}} \tag{4.108}$$

where $\boldsymbol{n}_i$ and l_i are the unit normal and element the length of the ith element, respectively. The solid angles at $\boldsymbol{x}_0$ can be calculated by (Pozrikidis, 2002)

$$\alpha\left(\boldsymbol{x_0}\right) = -PV\int_C \left[\boldsymbol{n}\cdot\nabla G^{AX}\left(\boldsymbol{x},\boldsymbol{x_0}\right)\right] r\left(\boldsymbol{x}\right) dl\left(\boldsymbol{x}\right). \tag{4.109}$$

4.3.2 Smoothing scheme

To prevent numerical instability of the velocity potential on the boundaries, a smoothing method (Longuet-Higgins and Cokelet, 1976; Pozrikidis, 2002) is employed. Smoothing of variables is performed using a five point formula given by

$$q_i^{(t+\Delta t)} = \frac{-q_{i-2}^{(t)} + 4q_{i-1}^{(t)} + 10q_i^{(t)} + 4q_{i+1}^{(t)} - q_{i+2}^{(t)}}{16} \tag{4.110}$$

where q_i is the variable to be smoothed at the ith node. In the present study, the smoothing treatment by Eq. (4.110) is preformed on the coordinates of the nodes, the velocity potential and its normal derivative, mean curvature on nodes every 5 step of the time stepping.

4.3.3 Galerkin approximation

The motion of the elastic wall and pressure on the liquid-solid interface is approximated by isoparametric linear basis functions, ϕ_j:

$$w(r,t) = \sum_{k=1}^{N_2} w_k(t)\phi_k(r), \tag{4.111}$$

$$p_w(r,t) = \sum_{k=1}^{N_2} \eta_k(t)\phi_k(r), \tag{4.112}$$

and a discretized form of Eq. (4.88) is obtained:

$$M_n^* M_{jk}\ddot{w}_k + \left(K_n^* M_{jk} + T_n^* A_{jk}\right) w_k = F^* M_{jk}\eta_k \tag{4.113}$$

where

$$M_{jk} = \int_0^a r\phi_j\phi_k dr, \tag{4.114}$$

$$A_{jk} = \int_0^a r\frac{\partial \phi_j}{\partial r}\frac{\partial \phi_k}{\partial r}dr. \tag{4.115}$$

Multiplying $M^* M_{jk}^{-1}$ on the both side of Eq. (4.113) leads to

$$\ddot{w}_j + B_{jk}w_k = t_{bj} \tag{4.116}$$

with

$$B_{jk} = \frac{K^*}{M^*}\delta_{jk} + \frac{T^*}{M^*}M_{ja}^{-1}A_{bk}, \tag{4.117}$$

$$t_{bj} = \frac{F^*}{M^*}\eta_j. \tag{4.118}$$

4.3.4 Adaptive time step

To overcome numerical instabilities of BEM encountered at rapid bubble growth and collapse phases, an adaptive time step is used with the fourth order explicit Runge-Kutta time integration, which determines the time step, Δt, depending on the magnitude of $|D\phi/Dt|$ on the calculation nodes:

$$\Delta t = \min\left[\delta t_{\mathrm{reg}}, \frac{T_f}{\max\left|\dfrac{D\phi}{Dt}\right|}\right] \tag{4.119}$$

where δt_{reg} is a constant time step which is regularly used unless $|D\phi/Dt|$ exceeds a critical value. A positive constant, T_f, is set so that an increment of the variables at every time stepping be kept on the same order throughout computation. In the present study, T_f is set at 0.005.

4.3.5 Newmark method

The wave equation is integrated in time by Newmark method, which consists of predictor and corrector steps. The displacement and velocity vectors are approximated by

$$w_k(t+\Delta t) = w_k(t) + \Delta t\dot{w}_k(t) + \frac{1}{2}\Delta t^2[(1-\beta_2)\ddot{w}_k(t) + \beta_2\ddot{w}_k(t+\Delta t)], \tag{4.120}$$

$$\dot{w}_k(t+\Delta t) = \dot{w}_k(t) + \Delta t[(1-\beta_1)\ddot{w}_k(t) + \beta_1\ddot{w}_k(t+\Delta t)]. \tag{4.121}$$

Substituting Eqs. (4.120) and (4.121) into Eq. (4.116) yields

$$\begin{aligned}\left[I_{jk} + \frac{1}{2}\beta_2\Delta t^2 B_{jk}\right]\ddot{w}_k(t+\Delta t) = &- B_{jk}\left[w_k(t) + \Delta t\dot{w}_k(t) + \frac{1}{2}(1-\beta_2)\Delta t^2\ddot{w}_k(t)\right] \\ &+ t_{bj}(t+\Delta t)\end{aligned} \tag{4.122}$$

where β_1 and β_2 are positive real parameters. For conservative computation (i.e., no numerical damping), $\beta_1 = 1/2$ and $\beta_2 = 1/4$ are used in the present study. The acceleration of the next time step is calculated by Eq. (4.122), and the displacement and velocity are obtained from Eqs. (4.120) and (4.121).

4.4 Numerical results

The translational dynamics of an oscillating bubble presented in the preceding sections is numerically explored. The effects of the elastic wall thickness and oscillation modes are examined to identify the acoustic property of the elastic layer based on a solid surface. The results are compared with the case of rigid wall.

4.4.1 Sample calculation

An initially spherical bubble of $10\,\mu\mathrm{m}$ in radius is located at $z/R_0 = 5 + h$; the initial distance between the bubble center and the wall surface is $d_w = 5$.The radius of the elastic wall is fixed at $a/R_0 = 5$ for all the cases considered below. The ambient pressure is 100 kPa, and the other physical parameters are $\rho_L = 1000\,\mathrm{kg/m^3}$, $\rho_w = 1000\,\mathrm{kg/m^3}$, $\mu_{\text{eff}} = 0.0067\ \mathrm{Pa\cdot s}$, $S = 0.073\ \mathrm{N/m}$ and the effective polytropic index of the bubble content is 1.1. The wall thickness and the oscillation mode are shown in Table 4.1. Note that the range of the control parameters are restricted because of numerical instability (Duncan and Zhang, 1991). To be simple, the mode number in the r direction is approximated by the fundamental mode $(m = 1)$. The driving sound frequency is set at ω_N so that the spherical bubble oscillation is under resonance.

TABLE 4.1: Dimensionless parameters with different wall thicknesses and the oscillation mode of (m, n) mode. The radius of the elastic layer is fixed at $a = 5R_0$, and the modulus of rigidity is G = 1.5 kPa. In cases (a) to (c), the wall thickness is fixed at 1.0, and different oscillation modes are considered. The wall thickness is varied in cases (d) and (e) for the fundamental mode $(1, 1)$. These cases are compared with the case of rigid boundary.

Case	h/R_0 [-]	(m,n)	p [-]	M^* [-]	T^* [-]	K^* [-]
(a)	1.0	$(1,1)$	0.035	5.9	0.0038	0.0025
(b)	1.0	$(1,2)$	0.083	98	0.063	0.80
(c)	1.0	$(1,3)$	0.16	990	0.63	26
(d)	0.8	$(1,1)$	0.10	4.3	0.0028	0.0018
(e)	2.0	$(1,1)$	0.028	10	0.0065	0.0039

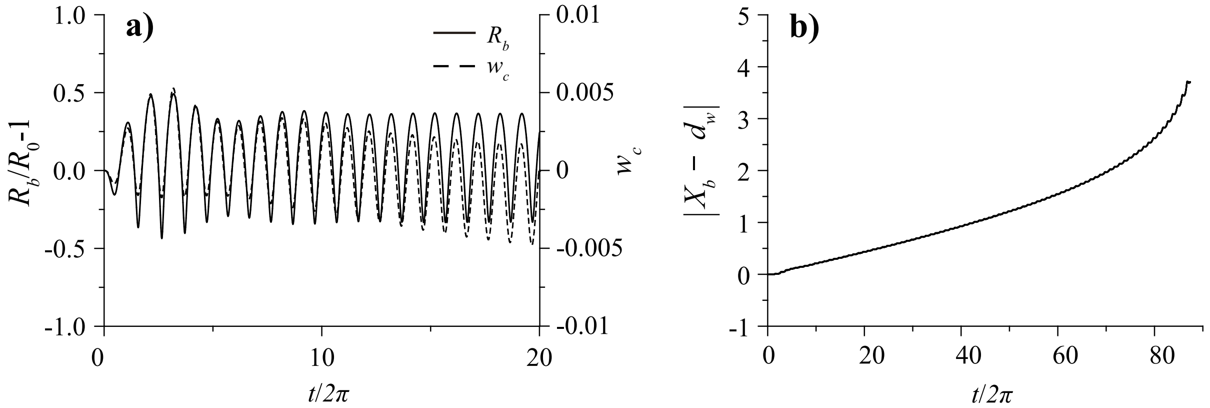

FIGURE 4.4: Temporal evolution of (a) the bubble mean radius, R_b, and (b) the bubble center, X_b, for case (a) in Table 4.1. For comparison, the displacement of the elastic wall at $r = 0$, w_c, is plotted in dashed line.

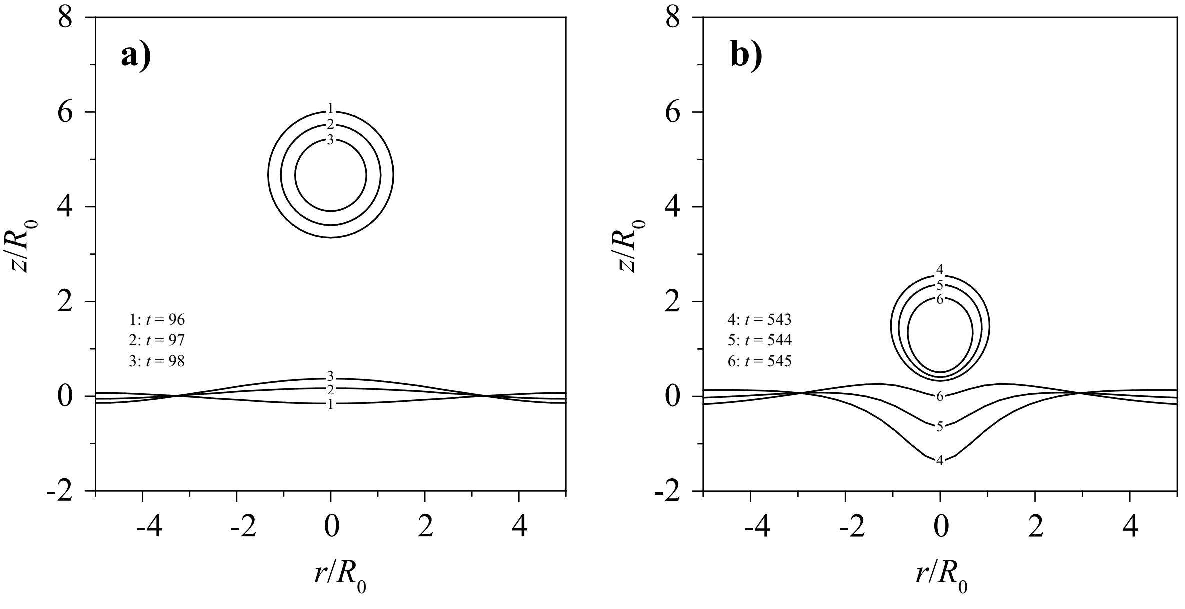

FIGURE 4.5: Temporal evolution of bubble and wall profiles. The corresponding time history of the bubble mean radius and bubble center are shown in Fig. 4.4. The displacement of the wall is illustrated with 100-fold magnification.

To give an overview of translational bubble oscillation, a sample calculation is presented for case (a) in Table 4.1. Fig. 4.4(a) shows temporal evolution of bubble mean radius defined by

$$R_b = \left(\frac{3V_b}{4\pi}\right)^{\frac{1}{3}} \tag{4.123}$$

where V_b is the volume of the bubble content. It is found that the wall oscillation is synchronized with the bubble motion; the bubble growth and contraction correspond to compression and expansion of the wall. This is because the natural frequency of the fundamental normal mode is lower than the sound frequency. The temporal evolution of bubble center is given in Fig. 4.4(b). The translational velocity of attractive motion directed toward the wall increases as the distance between the bubble and wall surface decreased.

Temporal evolution of the bubble and wall profiles are presented in Fig. 4.5 where the displacement of the elastic wall is depicted with 10^2-fold magnification. The spherical symmetry of the oscillating bubble is broken as the separation distance decreases, while the deformation of the elastic wall is smaller than the bubble oscillation by two orders of magnitude. It should be noticed that the deformed shape of the wall boundary is almost similar with the fundamental mode $(m = 1)$ except the close interaction as shown Fig. 4.5(b).

To show the effect of the higher oscillation modes, the evolution of translational motion is shown in Fig. 4.6 for different oscillation modes, and compared with the case

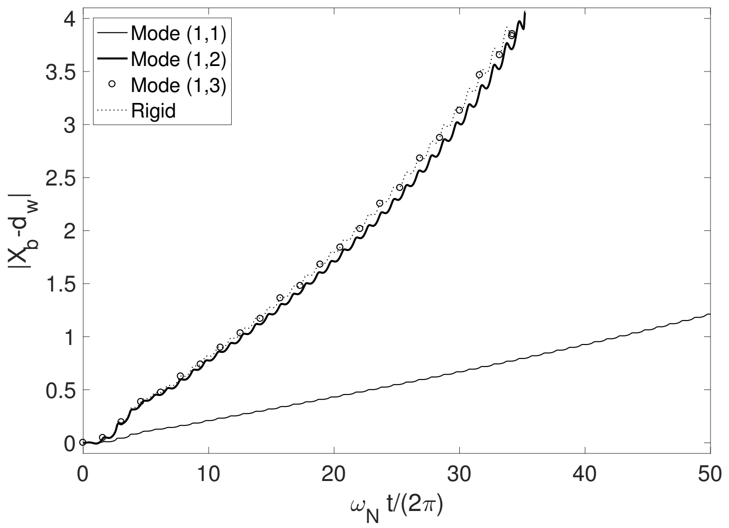

FIGURE 4.6: The temporal evolution of the bubble center, X_b, for different oscillation modes: (a) (m, n) = (1,1), (b) (m, n) = (1,2), (c) (m, n) = (1,3). The wall thickness is fixed to h = 1.0, and the other parameters are listed in Table 4.1.

of a rigid boundary. The parameters are shown in Table 4.1. It turns out that the translational velocity increases with increasing the oscillation mode number, indicating that the wall motion of the higher modes is converges to the case of a rigid wall. This implies that the small deformation of the elastic wall (i.e., transversal surface wave) has great importance to the bubble translational dynamics even in the case of incompressible assumption. It follows that the surface deformation of the lowest mode mainly determines the bubble-wall interaction.

In Fig. 4.7, the evolution of translational motion for the case of different wall thicknesses is shown. Here, the oscillation mode is fixed at $(1, 1)$ (fundamental mode). As the wall thickness decreased, the bubble translational velocity decays. Since the inertia of the wall converges to zero in the limit of $h \to 0$, the thiner wall experiences large amplitude oscillations, that is synchronized with the bubble wall motion (in-phase oscillation). Because of the in-phase motion of the bubble and wall boundary, the pressure change is less induced between the bubble and wall. As a result, the translational motion for the limit of $h \to 0$ does not converges to the case of a rigid wall. It can therefore be concluded that the presence of a thin elastic layer has great impact on the bubble and

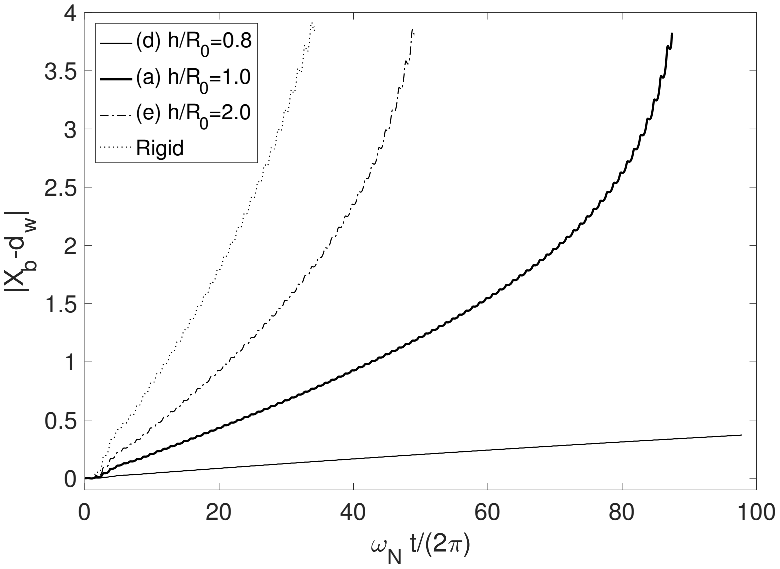

FIGURE 4.7: The temporal evolution of the bubble center, X_b, for different wall thicknesses: (a) h = 1.0, (d) h = 0.8, and (e) h = 2.0. The oscillation mode is fixed at $(1, 1)$, and the other parameters are listed in Table 4.1.

elastic wall interactions.

4.4.2 Summary

Numerical results of the coupled bubble-wall dynamics are presented. An analytical model and the basic equation for the coupled nonlinear dynamics of an oscillating bubble near an elastic wall are shown, and an eigenvalue analysis of linear isotropic elastodynamics of the compliant boundary is performed to obtain eigenfunctions and eigenfrequencies of normal modes. The coupled fluid-structure problem is numerically solved in the framework of the coupled BEM-FEM technique. The effect of the thickness and the oscillation modes of the elastic body on the translational direction and velocity of the oscillating bubble are discussed, drawing a conclusion that a small surface deformation of an elastic layer is not negligible for the translational dynamics of an oscillating bubble.

Chapter 5

Concluding remarks

5.1 Summary and conclusions

Coupled dynamics of oscillating bubbles have been explored analytically, experimentally and numerically; nonlinear modal analysis of coupled two spherical bubble oscillations developed bifurcation structures of steady-state oscillation based on perturbation method. Experimental observation of an oscillating bubble cluster was conducted and compared with classical model of the translational motion. Interaction between an oscillating bubble and an elastic wall was numerically investigated.

Asymptotic derivation of the steady-state solution and underlying nonlinear normal modes (NNMs) are provided in Chapter 2 for the primary resonance of two spherical bubbles oscillating with a fixed separation distance. In the case of equal-sized bubbles, an approximate solution of the oscillation amplitude and the phase shift showed symmetry-breaking bifurcations, leading to multi-valued stable solutions in the neighborhood of the localized NNMs. The distinctive feature of these solutions is that localized oscillation can occur depending on the driving frequency and the separation distance between the bubbles; the synchronized steady-state motion becomes unstable in a certain range of the parameter space. In addition to the symmetry-breaking bifurcation, Hopf bifurcations turn out to occur for the case of lower damping constants (i.e., for larger bubbles). Requirements necessary for the occurrence of localized oscillation are summarized: (a) The partial natural frequencies of the individual bubbles are close enough to arise the internal resonance; (b) Bubbles are in resonance at the imposed driving frequency; (c) Steady-state oscillation are achieved; (d) The separation distance is within a proper range where the coupling strength counterbalances the nonlinearity of the radial dynamics; (e) Damping effects are not so strong to smooth out the energy distribution among the bubbles. Some of our numerical calculation showed that the localized oscillation occur for a fairly typical parameter range used in practical experiments and simulations in the literature. This makes it difficult to accurately describe the bubble cloud dynamics since even a bubble cluster containing a small number of bubbles can have a large number of steady-states. However, the present bifurcation analysis offer improvements in the understanding of complex nonlinear behaviors of oscillating bubbles such as a formation of bubble structures and a sign reversal of the secondary Bjerknes force Pelekasis, Gaki, Doinikov, and Tsamopoulos, 2004.For future experimental applications of bubble oscillations, a single-sized bubble cloud in nonlinear resonance should therefore be designed with care in tuning the imposed sound frequency and the concentration of the bubbles.

An experimental technique was developed to observe translation of a bubble cluster oscillating under a stationary sound field and the translational dynamics were modeled by simply extending the theory of Bjerknes in Chapter 3. A gas bubble nucleus showed nonlinear oscillation in a low-frequency vibrating vessel and eventually leads to fission into bubble fragments. The bubble cluster showed translation toward the side wall. We explained the cluster translation as a result of the interaction with imaginary bubbles located at the opposite side of the side walls. The interaction was modeled by applying the Bjerknes theory of the second kind where the cluster is treated as a single bubble, while acoustic energy loss at the elastic wall was treated as a tuning parameter. We showed that the cluster translation observed in the experiment can be predicted properly by solving the equation of the cluster motion coupled with extended Bjerknes theory. It is concluded that the cluster translation in the present experiment is determined mainly by the secondary Bjerknes force and the cluster inertia. It is therefore suggested that, for the case of coupled bubble cluster oscillations, the translational dynamics of the bubble cloud consisted of the oscillating bubble cluster can be modeled by the classical Bjerknes theory with the spherical cluster dynamics described based on Rayleigh–Plesset-type equations. Furthermore, it can be able to predict the global dynamics of the bubble cluster structure, given the configuration of bubble cluster (size distribution and number of bubble fragments) can preliminarily be estimate for a particular case of interest. However, it remains in the future work to incorporate the fission of collapsing bubble as an additional damping of the bubble cluster volume oscillation in order to properly describe the time scale of the global cloud dynamics.

Chapter 4 presented an analytical model and the basic equation for the coupled nonlinear dynamics of an oscillating bubble near an elastic wall. Eigenvalue analysis of linear isotropic elastodynamics of a compliant boundary was performed to obtain eigenfunctions and eigenvalues of normal modes, which was coupled with the bubble oscillation. A numerical method to solve the previously presented fluid-structure coupled model was summarized in the following sections. It turns out that the small deformation of the elastic wall (i.e., transversal surface wave) has great importance to the bubble translational dynamics even in the case of incompressible assumption. The bubble translational dynamics is mainly determined by the surface deformation of the lowest eigenmode. Additionally, because of the in-phase motion of the bubble and wall boundary, the pressure change is less induced at the neighborhood of the bubble for the case of a thin wall. It follows that the limit of zero-wall thickness does not leads to the case of a rigid boundary. It can therefore be concluded that the presence of a thin elastic layer has great impact on the bubble and elastic wall interactions.

5.2 Suggestions for future work

The nonlinear modal analysis presented in Chapter 2 may be extended to bubble cluster oscillations, i.e., coupled multi-bubble or bubble cloud dynamics. A large number of steady-state solutions is expected to arise, which leads to complex spatial localization of oscillation energy in the bubble cloud. This leads to understanding in formation of complex bubble structures (i.e., a cluster of bubble chains) in a high intensity sound field.

The formation of an oscillating bubble cluster depends on the sound field and mechanical properties of the liquid (i.e., sound frequency, sound pressure, surface tension and viscosity of the host liquid). For engineering application, the number and size of bubble fragments in an oscillating cluster should be incorporated into the model equation. To complete the theory of Bjerknes for cluster oscillation, an experimental technique for observation of different cluster configurations is needed.

The elastic wall model used in this study assumes linear elasticity, indicating that the displacement of the elastic layer is sufficiently small compared to the wall thickness. However, the present numerical experiment shows large amplitude oscillations of the wall surface for the case of a thin wall thickness: the small strain assumption does not hold in the limit of $h \to 0$. It follows that the nonlinearity of the elastic wall should be incorporated into the linear spring-backed model for the case of a thin compliant layer coated on solid surface.

Appendix A

Nonlinear modal analysis

A.1 The scale analysis of the translational velocity

The translational motion can be approximately decoupled from the radial dynamics after a scale analysis described below. The term associated with the translational motion that we neglected on the right hand side of Eq. (2.2) is $u_2^2/4$ where u_2 is the translational velocity of the bubble 2 (Doinikov, 2002). This can be dropped from the equation of motion in the perturbation analysis to the order of $O(\epsilon^3)$ when the contribution of the term is of the order of $O(\epsilon^4)$:

$$\frac{\frac{1}{4}u_i^2}{\omega_N^2 R_{10}^2} \approx \epsilon^4 \tag{A.1}$$

where i takes 1 and 2. Substituting a representative oscillation amplitude of $\epsilon \approx 0.2$ and the Minnaert formula (Leighton, 2012), $\omega_N R_{10} \approx 2\pi \times 3\ \mathrm{m/s}$, for air bubbles in water at one atmosphere into Eq. (A.1), one obtain the model limitation velocity approximately given by

$$|u_i| \approx 1.5\ \mathrm{m/s}. \tag{A.2}$$

For the stationary assumption to be justified, the translational velocities should be sufficiently smaller than Eq. (A.2). This condition is likely satisfied in many practical experiments of moderately forced bubbles (Xi, Cegla, Mettin, Holsteyns, and Lippert, 2012; Jiao, He, Kentish, Ashokkumar, Manasseh, and Lee, 2015) except in the case of short-distance interaction. It can therefore be assumed that the translational motion has negligible contribution to the radial dynamics in the weakly nonlinear analysis. Furthermore, the contribution of temporal change of the separation distance, $\dot{d}^*(t)$, is also on the order of $O(\epsilon^4)$ or less. Therefore, the assumption of dropping the translational dynamics does not violate the qualitative feature of the particular examples shown in Chapter 2.

A.2 List of the dimensionless parameters

The dimensionless parameters in Eqs. (2.14) and (2.15) are

$$\omega_x = \left[3\kappa\text{Eu} + (3\kappa - 1)\frac{2}{\text{We}}\right]^{\frac{1}{2}}, \quad \omega_y = \left[3\kappa\frac{\text{Eu}}{R^{*2}} + (3\kappa - 1)\frac{2}{\text{We}R^{*3}}\right]^{\frac{1}{2}}, \tag{A.3}$$

$$c_x = \frac{4}{\text{Re}} + \frac{\omega_x^2}{C}, \quad c_y = \frac{4R^{*2}}{\text{Re}} + \frac{\omega_y^2}{CR^*}, \tag{A.4}$$

$$\mu_x = \frac{R^{*3}}{d^*}, \quad \mu_y = \frac{1}{d^* R^{*2}} \tag{A.5}$$

$$e_x = \text{Eu}A^*, \quad e_y = \frac{\text{Eu}A^*}{R^{*2}} \tag{A.6}$$

with which

$$\text{K} = \begin{bmatrix} \omega_x^2 & 0 \\ 0 & \omega_y^2 \end{bmatrix}, \tag{A.7}$$

$$\text{M} = \begin{bmatrix} 1 & \mu_x(1 + c_x\tau^*) \\ \mu_y(1 + c_y\tau^*) & 1 \end{bmatrix}, \tag{A.8}$$

$$\text{C} = \begin{bmatrix} c_x & \mu_x\tau^*\omega_x^2 \\ \mu_y\tau^*\omega_y^2 & c_y \end{bmatrix}, \tag{A.9}$$

$$\text{F} = \begin{bmatrix} e_x & 0 \\ 0 & e_y \end{bmatrix}. \tag{A.10}$$

The dimensionless parameters in Eqs. (2.22) and (2.23) are

$$\beta_{xx} = -\frac{(3\kappa+1)(3\kappa+2)-6}{\mathrm{We}} - \frac{(3\kappa+1)(3\kappa+2)-2}{2}\mathrm{Eu}, \tag{A.11}$$

$$\beta_{yy} = -\frac{(3\kappa+1)(3\kappa+2)-6}{\mathrm{We}R^{*3}} - \frac{(3\kappa+1)(3\kappa+2)-2}{2}\frac{\mathrm{Eu}}{R^{*2}}, \tag{A.12}$$

$$\beta_{xxx} = \frac{(3\kappa+1)(3\kappa+2)(3\kappa+3)-24}{3\mathrm{We}} - \frac{(3\kappa+1)(3\kappa+2)(3\kappa+3)-6}{6}\mathrm{Eu}, \tag{A.13}$$

$$\beta_{yyy} = \frac{(3\kappa+1)(3\kappa+2)(3\kappa+3)-24}{3\mathrm{We}R^{*3}} - \frac{(3\kappa+1)(3\kappa+2)(3\kappa+3)-6}{6}\frac{\mathrm{Eu}}{R^{*2}}. \tag{A.14}$$

A.3 Hopf bifurcation

Fig. A.1 presents a Hopf bifurcation structure of two equally-sized bubbles of $100\ \mu\mathrm{m}$ in radius. It turns out that underlying bifurcation structures are more complicated because of the higher Reynolds number due to the larger bubble size (i.e., lower damping constants) compared to case B ($R_{10} = R_{20} = 10\ \mu\mathrm{m}$); Hopf bifurcations arise on the localized oscillations, d3 and d4, at $\omega_f = 0.969$ and 0.990. Between the two bifurcation

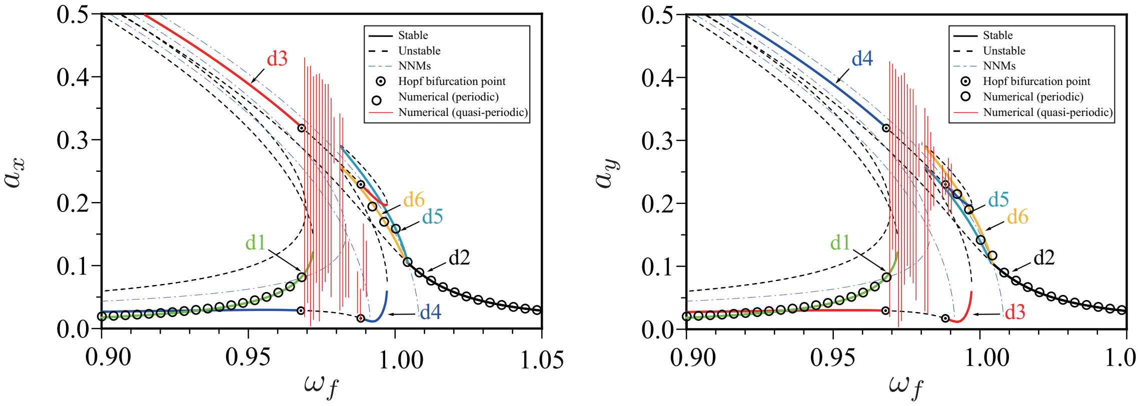

FIGURE A.1: The steady-state amplitude of the fundamental component for case F ($R_{10} = R_{20} = 100\ \mu\mathrm{m}$) in Table 2.1 as a function of the driving frequency denoted by di (i =1,2,3,4,5 and 6) in different colors. The numerical results of periodic solutions are shown by circles. The vertical lines indicate modulation amplitudes of quasi-periodic oscillations obtained during 1000 oscillation periods of the driving frequency.

points, the localized periodic solutions are unstable, leading to quasi-periodic oscillations. The vertical lines indicate modulation amplitudes of the quasi-periodic oscillation obtained during 1000 oscillation periods of the driving frequency. It is interesting to note that localized oscillations are the case with the modulation amplitudes; the quasi-periodic oscillations arise in the neighborhood the branches d3 and d4 at $\omega_f \approx 0.99$. Similar bifurcation structures consisting of symmetry-breaking and Hopf bifurcations are expected in other coupled nonlinear oscillators more than three dimensional state space (Kozłowski, Parlitz, and Lauterborn, 1995).

Appendix B

Dynamical analysis of the translational motion of an oscillating bubble

B.1 Eigenvalue analysis

The translational dynamics described by Eq. (3.16) has only one equilibrium point $(X^*_{\mathrm{st}}, U^*_{\mathrm{st}}) = (0, 0)$, which is a stationary solution of the system. Perturbation of (X^*, U^*) from the fixed point is denoted by $(\delta x, \delta u)$, and the linear truncation of Eq. (3.16) is obtained in the form of

$$\frac{d}{dt^*}\begin{pmatrix} \delta x \\ \delta u \end{pmatrix} = \begin{bmatrix} 0 & 1 \\ -4B & -C_D \end{bmatrix}\begin{pmatrix} \delta x \\ \delta u \end{pmatrix} \tag{B.1}$$

after the transformation with $X^* = X^*_{\mathrm{st}} + \delta x$ and $U^* = U^*_{\mathrm{st}} + \delta u$. The eigenvalues of the system are

$$\lambda = \frac{-C_D \pm \sqrt{C_D^2 + 16B}}{2}. \tag{B.2}$$

The bifurcation structure can be understood in B–C_D plain and is divided into three regions. The stability of $(X^*_{\mathrm{st}}, U^*_{\mathrm{st}})$ is determined only by the sign of B as explained below. When $B > 0$, the equilibrium point is unstable (saddle point) because of a positive real eigenvalue. This indicates that the oscillating bubble cannot stay away from the both side walls, leading to the attractive motion toward the walls. When B is negative, the equilibrium point is stable node or spiral depending on the magnitude of C_D, which is assumed positive real in this study. If $B < 0$ and C_D is small enough to satisfy $C_D^2 + 16B < 0$, the system presents damped oscillatory motion around the stable equilibrium point due to the complex eigenvalues. Increasing C_D causes qualitative change of the bubble behavior from damped oscillation to asymptotic motion to the equilibrium point. The sign of B depends on the acoustic impedance of the wall boundary, the separation distance and the imposed sound frequency (Ingard, 1951).

Bibliography

Apfel, R. E. 1984 Acoustic cavitation inception. *Ultrasonics* **22**, pp. 167–173.

Atchley, A. A. and Prosperetti, A. 1989 The crevice model of bubble nucleation. *The Journal of the Acoustical Society of America* **86**, pp. 1065–1084.

Baird, M. H. I. 1968 Behavior of gas bubbles in a vertically vibrating liquid column. *The Canadian Journal of Chemical Engineering* **46**, pp. 482–482.

Barbat, T., Ashgriz, N., and Liu, C.-S. 1999 Dynamics of two interacting bubbles in an acoustic field. *Journal of Fluid Mechanics* **389**, pp. 137–168.

Bjerknes, V. F. K. 1906 Fields of force. Cambridge Univ Press.

Blake, J. R., Taib, B. B., and Doherty, G. 1986 Transient cavities near boundaries. Part 1. Rigid boundary. *Journal of Fluid Mechanics* **170**, pp. 479–497.

Blake, J. R., Taib, B. B., and Doherty, G. 1987 Transient cavities near boundaries Part 2. Free surface. *Journal of Fluid Mechanics* **181**, pp. 197–212.

Blake, J. R., Robinson, P. B., Shima, A., and Tomita, Y. 1993 Interaction of two cavitation bubbles with a rigid boundary. *Journal of Fluid Mechanics* **255**, pp. 707–721.

Bremond, N., Arora, M., Dammer, S. M., and Lohse, D. 2006 Interaction of cavitation bubbles on a wall. *Physics of Fluids* **18**, p. 121505.

Bremond, N., Arora, M., Ohl, C.-D., and Lohse, D. 2006 Controlled multibubble surface cavitation. *Physical review letters* **96**, p. 224501.

Brennen, C. E. 2002 Fission of collapsing cavitation bubbles. *Journal of Fluid Mechanics* **472**, pp. 153–166.

Brennen, C. E. 2013 Cavitation and bubble dynamics. Cambridge University Press.

Carroll, J. M., Calvisi, M. L., and Lauderbaugh, L. K. 2013 Dynamical analysis of the nonlinear response of ultrasound contrast agent microbubbles. *The Journal of the Acoustical Society of America* **133**, pp. 2641–2649.

Chapman, R. B. and Plesset, M. S. 1971 Thermal effects in the free oscillation of gas bubbles. *Journal of Basic Engineering* **93**, pp. 373–376.

Chong, K. J. Y., Quek, C. Y., Dzaharudin, F., Ooi, A., and Manasseh, R. 2010 The effects of coupling and bubble size on the dynamical-systems behaviour of a small cluster of microbubbles. *Journal of Sound and Vibration* **329**, pp. 687–699.

Coussios, C. C. and Roy, R. A. 2008 Applications of acoustics and cavitation to noninvasive therapy and drug delivery. *Annual Review of Fluid Mechanics* **40**, pp. 395–420.

Crum, L. A. 1975 Bjerknes forces on bubbles in a stationary sound field. *The Journal of the Acoustical Society of America* **57**, pp. 1363–1370.

Delale, C. F. and Tunç, M. 2004 A bubble fission model for collapsing cavitation bubbles. *Physics of Fluids* **16**, pp. 4200–4203.

Devin Jr, C. 1959 Survey of thermal, radiation, and viscous damping of pulsating air bubbles in water. *The Journal of the Acoustical Society of America* **31**, pp. 1654–1667.

Doinikov, A. A. and Zavtrak, S. T. 1995 On the mutual interaction of two gas bubbles in a sound field. *Physics of Fluids* **7**, pp. 1923–1930.

Doinikov, A. A. 2002 Translational motion of a spherical bubble in an acoustic standing wave of high intensity. *Physics of Fluids* **14**, pp. 1420–1425.

Doinikov, A. A., Manasseh, R., and Ooi, A. 2005 Time delays in coupled multibubble systems (L). *The Journal of the Acoustical Society of America* **117**, pp. 47–50.

Dommermuth, D. G. and Yue, D. K. 1987 Numerical simulations of nonlinear axisymmetric flows with a free surface. *Journal of Fluid Mechanics* **178**, pp. 195–219.

Duncan, J. H., Milligan, C. D., and Zhang, S. 1996 On the interaction between a bubble and a submerged compliant structure. *Journal of Sound and Vibration* **197**, pp. 17–44.

Duncan, J. H. and Zhang, S. 1991 On the interaction of a collapsing cavity and a compliant wall. *Journal of Fluid Mechanics* **226**, pp. 401–423.

Dzaharudin, F., Suslov, S. A., Manasseh, R., and Ooi, A. 2013 Effects of coupling, bubble size, and spatial arrangement on chaotic dynamics of microbubble cluster in ultrasonic fields. *The Journal of the Acoustical Society of America* **134**, pp. 3425–3434.

Eller, A. and Flynn, H. 1965 Rectified diffusion during nonlinear pulsations of cavitation bubbles. *The Journal of the Acoustical Society of America* **37**, pp. 493–503.

Emmer, M., Van Wamel, A., Goertz, D. E., and De Jong, N. 2007 The onset of microbubble vibration. *Ultrasound in Medicine & Biology* **33**, pp. 941–949.

Farhangmehr, V., Aghdam, A. H., Shervani-Tabar, M. T., Parvizi, R., Ohl, S. W., and Khoo, B. C. 2014 Numerical investigation on the pulsating bubble dynamics in a narrow cylinder with a compliant coating. *Fluid Dynamics Research* **46**, p. 015513.

Francescutto, A. and Nabergoj, R. 1983 Steady-state oscillations of gas bubbles in liquids: Explicit formulas for frequency response curves. *The Journal of the Acoustical Society of America* **73**, pp. 457–460.

Geist, K. and Lauterborn, W. 1988 The nonlinear dynamics of the damped and driven Toda chain: I. Energy bifurcation diagrams. *Physica D: Nonlinear Phenomena* **31**, pp. 103–116.

Geist, K. and Lauterborn, W. 1991 The Nonlinear Dynamics of the Damped and Driven Toda Chain: III. Classification of the nonlinear resonances and local bifurcations. *Physica D: Nonlinear Phenomena* **52**, pp. 551–559.

Gibson, D. C. and Blake, J. R. 1982 The growth and collapse of bubbles near deformable surfaces. *Applied Scientific Research* **38**, pp. 215–224.

Gisbon, D. C. and Blake, J. R. 1980 Growth and collapse of cavitation bubbles near flexible boundaries. *7th Australasian Conference on Hydraulics and Fluid Mechanics 1980: Preprints of Papers*. Institution of Engineers, Australia, p. 283.

Harkin, A., Kaper, T. J., and Nadim, A. 2001 Coupled pulsation and translation of two gas bubbles in a liquid. *Journal of Fluid Mechanics* **445**, pp. 377–411.

Helfield, B. L. and Goertz, D. E. 2013 Nonlinear resonance behavior and linear shell estimates for Definity$^{\text{TM}}$ and MicroMarker$^{\text{TM}}$ assessed with acoustic microbubble spectroscopy. *The Journal of the Acoustical Society of America* **133**, pp. 1158–1168.

Hilgenfeldt, S., Lohse, D., and Brenner, M. P. 1996 Phase diagrams for sonoluminescing bubbles. *Physics of Fluids* **8**, pp. 2808–2826.

Hill, C. R. and Ter Haar, G. R. 1995 High intensity focused ultrasound—potential for cancer treatment. *The British Journal of Radiology* **68**, pp. 1296–1303.

Hsiao, C.-T. et al. 2013 Modelling single-and tandem-bubble dynamics between two parallel plates for biomedical applications. *Journal of Fluid Mechanics* **716**, pp. 137–170.

Ikeda, T., Harata, Y., and Nishimura, K. 2013 Intrinsic Localized Modes of Harmonic Oscillations in Nonlinear Oscillator Arrays. *Journal of Computational and Nonlinear Dynamics* **8**, p. 041009.

Ingard, U. 1951 On the reflection of a spherical sound wave from an infinite plane. *The Journal of the Acoustical Society of America* **23**, pp. 329–335.

Jameson, G. J. and Davidson, J. F. 1966 The motion of a bubble in a vertically oscillating liquid: theory for an inviscid liquid, and experimental results. *Chemical Engineering Science* **21**, pp. 29–34.

Jiao, J., He, Y., Kentish, S. E., Ashokkumar, M., Manasseh, R., and Lee, J. 2015 Experimental and theoretical analysis of secondary Bjerknes forces between two bubbles in a standing wave. *Ultrasonics* **58**, pp. 35–42.

Kalumuck, K. M., Duraiswami, R., and Chahine, G. L. 1995 Bubble dynamics fluid-structure interaction simulation by coupling fluid BEM and structural FEM codes. *Journal of Fluids and Structures* **9**, pp. 861–883.

Kang, I. S. and Leal, L. G. 1988 The drag coefficient for a spherical bubble in a uniform streaming flow. *Physics of Fluids* **31**, pp. 233–237.

Keller, J. B. and Miksis, M. 1980 Bubble oscillations of large amplitude. *The Journal of the Acoustical Society of America* **68**, pp. 628–633.

Kerschen, G., Peeters, M., Golinval, J.-C., and Vakakis, A. F. 2009 Nonlinear normal modes, Part I: A useful framework for the structural dynamicist. *Mechanical Systems and Signal Processing* **23**, pp. 170–194.

Kim, T.-H. and Kim, H.-Y. 2014 Disruptive bubble behaviour leading to microstructure damage in an ultrasonic field. *Journal of Fluid Mechanics* **750**, pp. 355–371.

Kim, W., Kim, T.-H., Choi, J., and Kim, H.-Y. 2009 Mechanism of particle removal by megasonic waves. *Applied Physics Letters* **94**, p. 081908.

King, M. E., Aubrecht, J., and Vakakis, A. F. 1995 Experimental study of steady-state localization in coupled beams with active nonlinearities. *Journal of Nonlinear Science* **5**, pp. 485–502.

Klaseboer, E. and Khoo, B. C. 2004 An oscillating bubble near an elastic material. *Journal of Applied Physics* **96**, pp. 5808–5818.

Klaseboer, E., Turangan, C. K., and Khoo, B. C. 2006 Dynamic behaviour of a bubble near an elastic infinite interface. *International Journal of Multiphase Flow* **32**, pp. 1110–1122.

Koch, P., Kurz, T., Parlitz, U., and Lauterborn, W. 2011 Bubble dynamics in a standing sound field: The bubble habitat. *The Journal of the Acoustical Society of America* **130**, pp. 3370–3378.

Kozłowski, J., Parlitz, U., and Lauterborn, W. 1995 Bifurcation analysis of two coupled periodically driven Duffing oscillators. *Physical Review E* **51**, p. 1861.

Krefting, D., Mettin, R., and Lauterborn, W. 2004 High-speed observation of acoustic cavitation erosion in multibubble systems. *Ultrasonics Sonochemistry* **11**, pp. 119–123.

Krefting, D., Toilliez, J. O., Szeri, A. J., Mettin, R., and Lauterborn, W. 2006 Translation of bubbles subject to weak acoustic forcing and error in decoupling from volume oscillations. *The Journal of the Acoustical Society of America* **120**, pp. 670–675.

Kreider, W., Crum, L. A., Bailey, M. R., and Sapozhnikov, O. A. 2011 Observations of the collapses and rebounds of millimeter-sized lithotripsy bubbles. *The Journal of the Acoustical Society of America* **130**, pp. 3531–3540.

Lauterborn, W. and Bolle, H. 1975 Experimental investigations of cavitation-bubble collapse in the neighbourhood of a solid boundary. *Journal of Fluid Mechanics* **72**, pp. 391–399.

Leighton, T. 2012 The acoustic bubble. Academic press.

Li, X., Ji, J. C., and Hansen, C. H. 2006 Non-linear normal modes and their bifurcation of a two DOF system with quadratic and cubic non-linearity. *International Journal of Non-Linear Mechanics* **41**, pp. 1028–1038.

Li, Z.-R., Sun, L., Zong, Z., and Dong, J. 2012 A boundary element method for the simulation of non-spherical bubbles and their interactions near a free surface. *Acta Mechanica Sinica* **28**, pp. 51–65.

Longuet-Higgins, M. S. and Cokelet, E. 1976 The deformation of steep surface waves on water. I. A numerical method of computation. *Proceedings of the Royal Society of London A: Mathematical, Physical and Engineering Sciences*. **350**. The Royal Society, pp. 1–26.

Lundgren, T. and Mansour, N. 1988 Oscillations of drops in zero gravity with weak viscous effects. *Journal of Fluid Mechanics* **194**, pp. 479–510.

Macdonald, C. A. and Gomatam, J. 2006 Chaotic dynamics of microbubbles in ultrasonic fields. *Proceedings of the Institution of Mechanical Engineers, Part C: Journal of Mechanical Engineering Science* **220**, pp. 333–343.

Magnaudet, J. and Legendre, D. 1998 The viscous drag force on a spherical bubble with a time-dependent radius. *Physics of Fluids* **10**, pp. 550–554.

Mettin, R., Akhatov, I., Parlitz, U., Ohl, C. D., and Lauterborn, W. 1997 Bjerknes forces between small cavitation bubbles in a strong acoustic field. *Physical Review E* **56**, p. 2924.

Miao, H. and Gracewski, S. M. 2008 Coupled FEM and BEM code for simulating acoustically excited bubbles near deformable structures. *Computational Mechanics* **42**, pp. 95–106.

Nasibullaeva, E. S. and Akhatov, I. S. 2013 Bubble cluster dynamics in an acoustic field. *The Journal of the Acoustical Society of America* **133**, pp. 3727–3738.

Nayfeh, A. H. 2008 Perturbation methods. John Wiley & Sons, pp. 228–244.

Nayfeh, A. H. and Mook, D. T. 2008 Nonlinear oscillations. John Wiley & Sons, pp. 195–196.

Neppiras, E. A. 1984 Acoustic cavitation series: part one: Acoustic cavitation: an introduction. *Ultrasonics* **22**, pp. 25–28.

Nigmatulin, R. I., Akhatov, I. S., Vakhitova, N. K., and Nasibullayeva, E. S. 2000 Dynamics of bubble clusters. *Nonliner Acoustic at the Turn of the Millenium: ISNA 15, 15th International Symposium.* **524**. AIP Publishing, pp. 455–458.

Nyborg, W. L. and Rodgers, A. 1967 The motion of liquid inside a closed vibrating vessel. *Biotechnology and Bioengineering* **9**, pp. 235–256.

Ohl, S. W., Klaseboer, E., and Khoo, B. C. 2009 The dynamics of a non-equilibrium bubble near bio-materials. *Physics in Medicine and Biology* **54**, p. 6313.

Ooi, A. and Manasseh, R. 2005 Coupled nonlinear oscillations of microbubbles. *ANZIAM Journal* **46**, pp. 102–116.

Parlitz, U., Englisch, V., Scheffczyk, C., and Lauterborn, W. 1990 Bifurcation structure of bubble oscillators. *The Journal of the Acoustical Society of America* **88**, pp. 1061–1077.

Pelekasis, N. A., Tsamopoulos, J. A., and Manolis, G. D. 1992 A hybrid finite-boundary element method for inviscid flows with free surface. *Journal of Computational Physics* **101**, pp. 231–251.

Pelekasis, N. A., Gaki, A., Doinikov, A., and Tsamopoulos, J. A. 2004 Secondary Bjerknes forces between two bubbles and the phenomenon of acoustic streamers. *Journal of Fluid Mechanics* **500**, pp. 313–347.

Pelekasis, N. A. and Tsamopoulos, J. A. 1993a Bjerknes forces between two bubbles. Part 1. Response to a step change in pressure. *Journal of Fluid Mechanics* **254**, pp. 467–499.

Pelekasis, N. A. and Tsamopoulos, J. A. 1993b Bjerknes forces between two bubbles. Part 2. Response to an oscillatory pressure field. *Journal of Fluid Mechanics* **254**, pp. 501–527.

Plesset, M. S. and Chapman, R. B. 1971 Collapse of an initially spherical vapour cavity in the neighbourhood of a solid boundary. *Journal of Fluid Mechanics* **47**, pp. 283–290.

Pozrikidis, C. 2002 A practical guide to boundary element methods with the software library BEMLIB. CRC Press, pp. 9–109.

Prosperetti, A. and Lezzi, A. 1986 Bubble dynamics in a compressible liquid. Part 1. First-order theory. *Journal of Fluid Mechanics* **168**, pp. 457–478.

Prosperetti, A., Crum, L. A., and Commander, K. W. 1988 Nonlinear bubble dynamics. *The Journal of the Acoustical Society of America* **83**, pp. 502–514.

Reddy, A. J. and Szeri, A. J. 2002 Coupled dynamics of translation and collapse of acoustically driven microbubbles. *The Journal of the Acoustical Society of America* **112**, pp. 1346–1352.

Robinson, P. B., Blake, J. R., Kodama, T., Shima, A., and Tomita, Y. 2001 Interaction of cavitation bubbles with a free surface. *Journal of Applied Physics* **89**, pp. 8225–8237.

Rosenberg, R. M. 1966 On Nonlinear Vibrations of Systems with Many Degrees of Freedom. *Advances in Applied Mechanics* **9**, p. 155.

Rosenberg, R. M. 1960 Normal modes of nonlinear dual-mode systems. *Journal of Applied Mechanics* **27**, pp. 263–268.

Rosenberg, R. M. 1962 The normal modes of nonlinear n-degree-of-freedom systems. *Journal of Applied Mechanics* **29**, pp. 7–14.

Sato, M., Hubbard, B. E., English, L. Q., Sievers, A. J., Ilic, B., Czaplewski, D. A., and Craighead, H. G. 2003 Study of intrinsic localized vibrational modes in micromechanical oscillator arrays. *Chaos: An Interdisciplinary Journal of Nonlinear Science* **13**, pp. 702–715.

Shima, A., Tomita, Y., Gibson, D. C., and Blake, J. R. 1989 The growth and collapse of cavitation bubbles near composite surfaces. *Journal of Fluid Mechanics* **203**, pp. 199–214.

Sochard, S., Wilhelm, A.-M., and Delmas, H. 1998 Gas-vapour bubble dynamics and homogeneous sonochemistry. *Chemical Engineering Science* **53**, pp. 239–254.

Soh, W. K. 1992 An energy approach to cavitation bubbles near compliant surfaces. *Applied Mathematical Modelling* **16**, pp. 263–268.

Sorokin, V. S., Blekhman, I. I., and Vasilkov, V. B. 2012 Motion of a gas bubble in fluid under vibration. *Nonlinear Dynamics* **67**, pp. 147–158.

Sudo, S. and Hashimoto, H. 1988 Unsteady Pressure Response of a liqud in a Cylindrical Container Subject to Vertical Vibration. *JSME International Journal. Ser. 2, Fluids Engineering, Heat Transfer, Power, Combustion, Thermophysical Properties* **31**, pp. 227–233.

Takagi, S. and Matsumoto, Y. 2011 Surfactant effects on bubble motion and bubbly flows. *Annual Review of Fluid Mechanics* **43**, pp. 615–636.

Takahira, H., Yamane, S., and Akamatsu, T. 1995 Nonlinear oscillations of a cluster of bubbles in a sound field (bifurcation structure). *JSME International Journal. Series B, Fluids and Thermal Engineering* **38**, pp. 432–439.

Takahira, H., Akamatsu, T., and Fujikawa, S. 1994 Dynamics of a Cluster of Bubbles in a Liquid. Theoretical Analysis. *JSME International Journal Series B Fluids and Thermal Engineering* **37**, pp. 297–305.

Vakakis, A. F., Manevitch, L. I., Mikhlin, Y. V., Pilipchuk, V. N., and Zevin, A. A. 2008 Normal Modes and Localization in Nonlinear Systems. John Wiley & Sons, 8–21.

Wang, Q. X., Yeo, K. S., Khoo, B. C., and Lam, K. Y. 1996 Nonlinear interaction between gas bubble and free surface. *Computers & Fluids* **25**, pp. 607–628.

Wang, Q. 2014 Multi-oscillations of a bubble in a compressible liquid near a rigid boundary. *Journal of Fluid Mechanics* **745**, pp. 509–536.

Wang, S., Zhang, A., Liu, Y., and Zeng, D. 2013 Numerical simulation of bubble dynamics in an elastic vessel. *The European Physical Journal E* **36**, pp. 1–7.

Wiedemair, W., Tukovic, Z., Jasak, H., Poulikakos, D., and Kurtcuoglu, V. 2014 Modeling the interaction of microbubbles: Effects of proximity, confinement, and excitation amplitude. *Physics of Fluids* **26**, p. 062106.

Xi, X., Cegla, F., Mettin, R., Holsteyns, F., and Lippert, A. 2012 Collective bubble dynamics near a surface in a weak acoustic standing wave field. *The Journal of the Acoustical Society of America* **132**, pp. 37–47.

Yang, X. and Church, C. C. 2005 A model for the dynamics of gas bubbles in soft tissue. *The Journal of the Acoustical Society of America* **118**, pp. 3595–3606.

Yu, H., Lin, Z., Xu, L., Liu, D., and Shen, Y. 2015 Theoretical study of microbubble dynamics in sonoporation. *Ultrasonics* **61**, pp. 136–144.

Zabolotskaya, E. A. 1984 Interaction of gas-bubbles in a sound field. *Soviet Physics Acoustics-Ussr* **30**, pp. 365–368.

Zhang, S., Duncan, J. H., and Chahine, G. L. 1993 The final stage of the collapse of a cavitation bubble near a rigid wall. *Journal of Fluid Mechanics* **257**, pp. 147–181.

List of publications

Sugita, N., & Sugiura, T. 2017 Nonlinear normal modes and localization in two bubble oscillators. Ultrasonics **74**, pp. 174-185.

Sugita, N., Ando, K. & Sugiura, T. 2017 Experiment and modeling of translational dynamics of an oscillating bubble cluster in a stationary sound field. Ultrasonics [Accepted for publication]